

Theoretische Physik

Precision computations for gaugino and scalar dark matter

Inaugural-Dissertation
zur Erlangung des Doktorgrades
der Naturwissenschaften im Fachbereich Physik
der Mathematisch-Naturwissenschaftlichen Fakultät
der Westfälischen Wilhelms-Universität Münster

vorgelegt von
David Regalado Lamprea
aus Sevilla
- 2018 -

Dekan:	Prof. Dr. Michael Klasen
Erster Gutachter:	Prof. Dr. Michael Klasen
Zweite Gutachterin:	Jun. Prof. Dr. Anna Kulesza
Tag der mündlichen Prüfung:	
Tag der Promotion:	

Zusammenfassung

Das Standardmodell der Teilchenphysik ist eines der erfolgreichsten Theorien in der Geschichte der Naturwissenschaften. Es hat die Quantenchromodynamik und die Theorie der elektroschwachen Wechselwirkungen in ein gemeinsames elegantes Modell vereint, welches natürliche Phänomene mit beispielloser Genauigkeit erklären vermag. Jedoch gibt es theoretische und experimentelle Hinweise, die darauf schließen, dass das Standardmodell erweitert werden muss um alle natürlichen Phänomene präzise erklären zu können. Auch abgesehen von den sehr wichtigen Problemen der Gravitation und der dunklen Energie, wird das Standardmodell im elektroschwachen Sektor in der Form von dunkler Materie, der nicht verschwindenden Neutrinomassen, welches das Standardmodell alleine nicht erklären kann, herausgefordert. Darüber hinaus gibt es Andeutungen im Higgs Sektor wie zum Beispiel das Hierarchieproblem, welches auch auf die Notwendigkeit einer neuen Physik hinweist.

Bei der Suche nach neuer Physik sind präzise Vorhersagen von zentraler Bedeutung. Zusammen mit der steigenden Präzision von experimentellen Ergebnissen können diese zu wichtigen Beschränkungen oder gar zu einer kompletten Ausschließung von Modellen führen. In dieser Arbeit werden wir Präzisionsrechnungen dieser Art im supersymmetrischen und nicht-supersymmetrischen Kontext durchführen.

Der Fokus des ersten Teils der Arbeit liegt auf Resummationsvorhersagen am LHC für den elektroschwachen Sektor einer minimalen supersymmetrischen Erweiterung des Standardmodells. Wir werden zeigen, wie diese Vorhersagen zu vernünftigen Resultaten in kinematischen Regionen führt, in denen die perturbative Störungsreihe nicht mehr konvergiert. Des Weiteren wird dadurch die Präzision des Wirkungsquerschnitts erhöht und die Skalenunsicherheit reduziert.

In dem zweiten Teil wird unser Fokus auf den beiden Hauptprobleme des elektroschwachen Sektors liegen: die Existenz der dunklen Materie und die Existenz der nicht verschwindenden Neutrinomassen. Wir werden eine geringfügige Erweiterung des Standardmodells analysieren, welches Neutrino Massen im 1-Loop erzeugt und Kandidaten für die dunkle Materie beinhaltet. Wir werden den Parameterraum des Modells untersuchen und zeigen, dass es realisierbare Regionen für alle vorhandenen experimentellen Einschränkungen gibt, jedoch auch, wie zukünftige Experimente in naher Zukunft diese Regionen untersuchen können.

Abstract

The standard model of particle physics is one of the most successful theoretical frameworks in the history of science. It has provided the unification of quantum chromodynamics and the electroweak theory into a common elegant model that can explain natural phenomena with unprecedented accuracy. However there are theoretical and experimental reasons to conclude that the standard model must be extended to properly explain all natural phenomena. Even apart from the very important issues of gravity and dark energy, the standard model faces challenges in the electroweak sector, in the form of dark matter, the nonzero neutrino masses which the standard model alone cannot accommodate, and some hints in the the Higgs sector like the hierarchy problem also point towards the need for new physics.

In this quest for new physics, precision is of vital importance, since precise theoretical predictions coupled with the every-increasingly precise experimental results are necessary to constrain and eventually rule out the different theoretical possibilities. We will investigate in this work approaches to this type of precise predictions in both supersymmetric and nonsupersymmetric contexts.

In the first part of this work we will focus on supersymmetric models and we will investigate the use of resummation procedures for predictions in the electroweak sector of the minimal supersymmetric standard model at the LHC, and we will show how they lead to sound predictions in kinematical regions where fixed-order approaches fail and overall how they improve the precision of the cross section computations and considerably reduce the scale uncertainties.

In the second part we will focus on arguably the two main issues of the electroweak sector: the existence of dark matter and the existence of nonzero neutrino masses. We will analyze a minimal extension of the standard model that generates neutrino masses radiatively at one-loop, and contains dark matter candidates. We will explore the parameter space of this model and show that it contains viable regions for all current constraints, but will also show how expected future sensitivities will probe these regions in the near future.

Contents

1	The Standard Model and Beyond	11
I	Collider phenomenology	15
2	Theoretical background	17
2.1	Perturbative QCD	17
2.1.1	Running coupling	18
2.1.2	QCD factorization	19
2.1.3	Parton distribution functions	20
2.2	Resummation	25
2.2.1	Introduction	25
2.2.2	Threshold resummation	27
2.2.3	Transverse momentum resummation	33
2.3	Supersymmetry	36
2.3.1	Introduction	36
2.3.2	Construction of the supersymmetric lagrangian	37
2.3.3	The Minimal Supersymmetric Standard Model	43
3	Resummino	47
3.1	Software implementations of resummation	47
3.2	Code architecture and structure	48
3.2.1	Build system	48
3.2.2	Included external dependencies	49
3.2.3	Code structure	49
3.3	Software requirements and installation	52
3.3.1	Explanation of dependencies	52
3.3.2	Installation of dependencies	53
3.3.3	Compilation	54
3.4	Software usage	55
3.4.1	Input file	55
3.4.2	Running Resummino	57
3.4.3	Resummino output	58

3.5	Examples	59
4	Gaugino production	61
4.1	Current experimental searches and constraints	61
4.2	Benchmark points	66
4.3	Total cross sections	67
4.4	Invariant mass and transverse momentum	70
4.4.1	Invariant mass distributions	71
4.4.2	Transverse momentum distributions	73
II	Minimal models	79
5	Dark matter	81
5.1	Evidence for dark matter	81
5.1.1	Anomalous velocity of luminous objects	82
5.1.2	Gravitational lensing	82
5.1.3	Cosmological measurements	83
5.2	Models of dark matter	84
5.2.1	Supersymmetric candidates	85
5.2.2	Non-supersymmetric candidates	85
5.3	Relic density calculation	86
5.4	Dark matter detection	87
5.4.1	Direct detection	88
5.4.2	Indirect detection	89
5.4.3	Collider searches	93
6	Neutrino masses	95
6.1	Evidence for neutrino masses	95
6.1.1	Solar neutrino experiments	99
6.2	Majorana neutrinos and the Weinberg operator	100
6.3	Majorana masses	100
6.4	Seesaw and inverse seesaw models	102
6.5	Radiative seesaw models	104
6.6	Lepton flavor violation processes	105
7	Minimal models	107
7.1	Introduction and review of current minimal models	107
7.2	Definition of the model	108
7.3	Phenomenology	110
7.3.1	Collider constraints	110
7.3.2	Neutrino masses	111
7.3.3	Lepton flavor violation	113
7.3.4	Dark matter	114

7.3.5	Dark matter self-energy	115
8	Results	117
8.1	Numerical implementation	117
8.1.1	Overview	117
8.1.2	SARAH	118
8.1.3	SPheno	118
8.1.4	Micromegas	118
8.1.5	DarkSUSY	119
8.2	Numerical results	120
8.2.1	Parameter space	120
8.2.2	Lepton flavor violation processes	123
8.2.3	Direct detection	127
8.2.4	Indirect detection	127
8.2.5	Collider phenomenology	128
9	Conclusions	131
A	Gaugino total cross sections	135
	Bibliography	137

Chapter 1

The Standard Model and Beyond

The standard model of particle physics is arguably one of the most successful scientific theories ever made. From a theoretical point of view it combined in a single mathematical framework what appears to be distinct physical effects as explained by quantum chromodynamics or the electroweak theory, and from an experimental point of view it has led to some of the most precise predictions of any physical theory. However, despite this success, there are both theoretical hints and experimental evidence that the standard model needs to be modified or extended to explain the universe as observed. We will briefly introduce some of the issues as motivation for beyond the standard model theories as will be further studied in this work, and name the most promising candidates to solve some of these issues.

Arguably the most prominent of the issues of the Standard Model is that it contains no renormalizable theory of **gravity**, and therefore an important part of the physical phenomenology cannot be explained by the Standard Model alone. A quantum theory of gravity continues to be one of the main open problems in science. A second issue is that a large portion of the energy budget of the universe as we measure through cosmological measurements is in the form of **dark energy**, which is known to have a different behavior than that of matter and radiation, and the Standard Model alone cannot account for such a type of energy. These two issues may well be related to each other, since a full account of gravitational phenomena may be necessary to explain the nature of dark matter. But even within the realm of the electroweak and quantum chromodynamics sectors there are open issues. The Standard Model has no particle with the required properties to explain an important part of the matter content of the universe, the so-called **dark matter**. We will study this issue in more detail in Ch. 5. And last, it is not possible to introduce a renormalizable **neutrino mass** term in the Standard Model lagrangian, whereas we have enough experimental evidence to claim that (at

least two of) the neutrinos must have a nonzero mass. We will analyze this issue also in detail in Ch. 6.

Apart from these issues, there are other indications, that while not problem of the theory by themselves, serve on different grounds as hint for the possible existence of possible extensions that would contain natural explanations for such observations. For example, the Standard Model requires relatively **many free parameters** and many particles which seem to appear independently of each other. In particular, there seems to exist three copies (families) of each particle type, without any convincing explanation for this multiplicity. Another issue is the so-called **strong CP problem**: The Standard Model does not seem to violate CP invariance in the strong sector, whereas there seems to be no reason for that terms to vanish. An important case of this in the case of supersymmetry is the so-called **hierarchy problem**, i.e. the fact that a very precise fine-tuning or cancellation is required to obtain the correct mass of the Higgs boson (of tens of order of magnitude the actual Higgs boson mass).

Different theories provide a solution to a different set of these problem or issues. We will analyze the different theoretical possibilities to develop such models. For that we first notice that since the SM is a quantum field theory (QFT) it is therefore uniquely determined by its gauge symmetries and a set of particles that transform under a given representation of the gauge the symmetries. The symmetries in turn are usually classified into gauge (or internal) and spacetime (or external). Thus, if we want to extend the SM but remain in the QFT framework, we can do one or more of the following:

Firstly, we can extend the gauge symmetries. This kind of theories can at the same be divided into two groups: top-down and bottom-up approaches. In top-down approaches, the symmetries at low energy scales are the result of the breaking of more symmetric gauge groups through spontaneous symmetry breaking. To this group belong the Grand Unified Theories. In bottom-up approaches, new gauge symmetries are added to the SM gauge group in a constructive way. There are several theoretical motivations for these kind of theories, like left-right symmetries. These both approaches are of course not exclusive, and certain theories can be studied from either point of view.

Respecting the spacetime symmetries there are also two possibilities: a first obvious possibility is just to increase the number of spacetime dimensions (Extra-Dimensional theories, ED). But even if one wants to remain in four dimensions, it is possible to extend the symmetries by introducing Supersymmetry. Supersymmetric theories are one of the most interesting BSM theories from a theoretical and phenomenological point of view.

Lastly, it is possible to keep the same symmetries, but add new particles to the model. This is for example the case of seesaw mechanism.

These different options are not exclusive between each other and can be combined with each other in some models. Interestingly enough, if one

wants to leave the QFT framework (e.g., string theory) one finds all of these options are usually required on mathematical consistency grounds.

Part I

Collider phenomenology

Chapter 2

Theoretical background

As we have seen, supersymmetry is one of the most promising beyond the standard model (BSM) theories. Current experimental studies require very precise theoretical predictions to investigate the supersymmetric parameter space, and therefore procedures like resummation become crucial in supersymmetry studies at hadron colliders. In this chapter we will review the necessary theory for such studies, and in particular we will focus on resummation predictions for gaugino production at hadron colliders. In 2.1 we will review the required background for perturbative quantum chromodynamics which will be the basis of further computations. In 2.2 we will introduce the resummation framework for precise computations at hadron colliders in kinematical regions where fixed-order computations become unstable due to the existence of potentially large logarithms, and finally in 2.3 we will review the theory of supersymmetry and in particular its gaugino sector.

2.1 Perturbative QCD

Since the first observation of the scaling obeyed by deep inelastic structure functions it has been known that the strong interaction becomes weaker at smaller distances, and in fact the construction of quantum chromodynamics as the quantum field theory of strong interactions has been based on the property of *asymptotic freedom*, i.e. that the strong coupling vanishes as the relevant distance of the phenomenon goes to zero. The smallness of the coupling in this limit implies that the use of perturbation theory is justified, which has a great relevance in the phenomenology of strong interactions, since it allows for a systematic analytical computational method. However, as we will see long-distance physics also enters crucially in the computation, so that factorization will be necessary to split those contributions which cannot be computed perturbatively. We will follow the computations in [1].

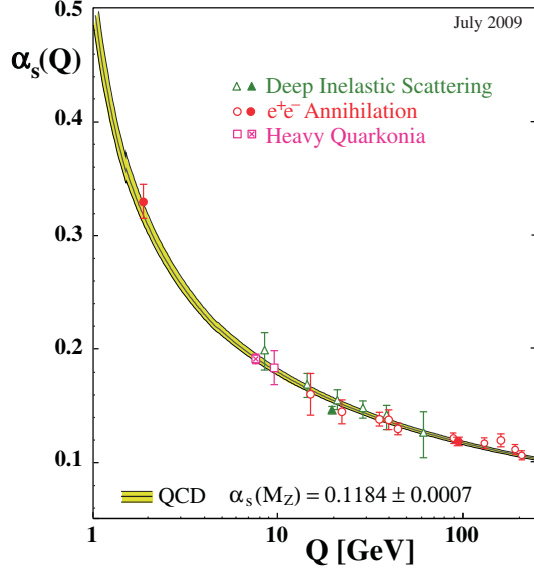


Figure 2.1: Measurements of α_s as a function of the energy scale Q . The solid curves are QCD predictions by extrapolating the world average measurement of $\alpha_s(M_Z)$ using 4-loop computations. From [3].

2.1.1 Running coupling

Quantum Chromodynamics is defined by the lagrangian density [2]

$$\mathcal{L}_{\text{QCD}} = -\frac{1}{4}F_{\mu\nu}F^{\mu\nu} + \bar{\psi}(i\not{D} - M)\psi + \frac{1}{2\zeta}(\partial \cdot A)^2 + \partial_\mu \bar{c}_a(\partial^\mu c_a + gf_{abc}c_b A_c^\mu) \quad (2.1)$$

where A, ψ, c are the gluon, quark and Faddeev-Popov ghost fields, $D_\mu = \partial_\mu + igA_{a\mu}t_a$ is the covariant derivative, $F_{\mu\nu}$ is the field strength tensor, f_{abc} are the SU(3) structure constants and t_a are the SU(3) generators of the fundamental representation. The ζ term is a gauge-fixing term.

As usual, to avoid ultraviolet divergences we require renormalization of the defined lagrangian. Since we know that quantum chromodynamics is renormalizable, the nonphysical degrees of freedom, i.e. the longitudinal gluons and ghosts, must decouple from the physics, and using the Ward identities it can be shown that the theory is gauge invariant.

We can regulate the divergences in a gauge-invariant way using dimensional regularization, and then introduce renormalization factors Z_i for the coupling, masses fields, and gauge fixing parameter ζ . It can be shown that no extra counterterms other than those are required to make the Green function finite after removing regularization.

The Z coefficients of the renormalization procedure have some arbitrariness, since finite parts can be added to the counterterms. This freedom can be used to remove large logarithms that would spoil the perturbativity.

When one changes the renormalization scale μ , since the unrenormalized parameters g_0, M_0 are fixed, the values of the renormalized parameters g, M must vary to preserve renormalization group invariance. Thus the coupling becomes a function of the scale μ given by the renormalization group equation

$$\mu \frac{dg(\mu)}{d\mu} = \beta(g(\mu)) \quad (2.2)$$

where β can be determined through perturbative calculations

$$\beta(g) = -g \left(\frac{\alpha_S}{4\pi} \beta_1 + \left(\frac{\alpha_S}{4\pi} \right)^2 \beta_2 + \mathcal{O}(\alpha_S^3) \right) \quad (2.3)$$

and is obtained as

$$\beta_1 = 11 - 2n_f/3 = (11N_c - 2n_f)/3 \quad (2.4)$$

with N_c the number of colors and n_f the number of flavors. The first positive term comes mostly from nonabelian diagrams and the second negative term comes from the fermion loop diagram, and for β_2 we obtain

$$\beta_2 = 102 - 38n_f/3. \quad (2.5)$$

With this, to the lowest order of approximation we can write

$$\alpha_S(\mu^2) = \frac{\alpha_S(\mu_0)}{1 + (\beta_1/4\pi)\alpha_S(\mu_0^2)\log(\mu^2/\mu_0^2)} \quad (2.6)$$

where we have evolved the value of α_S to an arbitrary value of μ from the knowledge of $\alpha_S(\mu_0)$ at a certain level μ_0 e.g. frequently the mass of the Z boson m_Z . When written in this form it may seem that the running depends on $\alpha_S(\mu_0)$ and μ_0 independently, which is not possible because it must be independent of the reference taken. A more appropriate representation thus combined both dependencies into a single variable

$$\alpha_S(\mu^2) = \frac{4\pi}{\beta_1 \log(\mu^2/\Lambda^2)} \quad (2.7)$$

We can also write a more accurate approximation by taking into account also β_2 in eq. (2.3), and we get

$$\frac{\alpha_S}{4\pi} = \frac{1}{\beta_1 \log(\mu^2/\Lambda^2)} - \frac{\beta_2 \log(\log(\mu^2/\Lambda^2))}{\beta_1^3 \log^2(\mu^2/\Lambda^2)} + \mathcal{O}\left(\frac{1}{\log^3(\mu^2/\Lambda^2)}\right). \quad (2.8)$$

2.1.2 QCD factorization

The fact that the strong coupling as we have seen becomes larger at low energies at the point of the Landau pole divergence at the QCD scale Λ_{QCD}

leads to the property of parton confinement of QCD, i.e. the fact that partons hadronize forming baryons or mesons on timescales $\sim 1/\Lambda$ [4]. This makes it impossible to describe the structure, in this case of the proton, from a perturbative point of view. However, the minus sign in Eq. (2.3) leads to another of the crucial properties of QCD, the Asymptotic Freedom [5, 6], or the fact that the strong coupling becomes weaker at larger energies therefore allowing the description of QCD processes at high energies as that of the partons (quarks and gluons) inside the proton as interacting “freely”. This allows to understand the hadronic process as two separated processes, first the description of the partons inside the proton in the form of a structure function, known as the parton distribution function, convoluted with the partonic scattering process where the rest of the proton structure is ignored. This is known as the QCD factorization property and is a key factor in allowing theoretical predictions in hadronic processes such as those at hadron colliders.

At leading order, the parton distribution functions (which will be studied in more detail in the next section) can be simply understood as the probability that a given parton type carries a given fraction of the proton total momentum. At further orders this simple picture is lost, but the computational power they offer for hadronic processes remains. A physical explanation or interpretation for this factorization property lies in the separation of physical time (or energy) scales. If we set of the center of mass frame, it is easy to see that the two hadrons are Lorentz contracted with respect to each other. This means the interactions of a parton inside a hadron with the other hadron will occur in time scales much shorter than those happening inside its own hadron. Also those interactions inside one hadron will be time dilated and therefore further separating the time scales. All this leads to the collision interactions happening at significantly shorter scales than those inside a hadron given the collision happens at enough energy.

In the following section we will focus on these parton distribution function starting as is usual in these cases in a deep inelastic scattering framework.

2.1.3 Parton distribution functions

One of the crucial tools to investigate the structure of hadrons is deep inelastic scattering experiments, where a lepton (an electron, muon, or neutrino) interacts with a hadron, mainly through the exchange of photons. This process provides one of the main tests of perturbative quantum chromodynamics, and also serves to determine the structure function of the hadron which is later used on collider experiments.

We consider the scattering of a lepton with momentum k with a hadron, in particular a proton with momentum p , through a virtual photon with

momentum q . The variables for this process are usually noted [1]

$$\begin{aligned}
Q^2 &:= -q^2 \\
M^2 &:= p^2 \\
\nu &:= p \cdot q = M(E' - E) \\
x &:= \frac{Q^2}{2\nu} = \frac{Q^2}{2M(E' - E)} \\
y &= \frac{q \cdot p}{k \cdot p} = 1 - E'/E,
\end{aligned} \tag{2.9}$$

where the energies are referred to the target rest frame and M is the proton mass.

We parametrize the structure of the proton in terms of the so-called *structure functions* $F_i(x, Q^2)$ such that we can write the cross section as

$$\begin{aligned}
\frac{d^2\sigma}{dx dy} &= \frac{8\pi\alpha^2 ME}{Q^4} \times \\
&\left(\left(\frac{1 + (1-y)^2}{2} \right) 2xF_1 + (1-y)(F_2 - 2xF_1) - (M/2E)xyF_2 \right), \tag{2.10}
\end{aligned}$$

in the limit $Q^2 \ll M_Z^2$ for the charged lepton case, and similarly for the neutrino

$$\frac{d^2\sigma}{dx dy} = \frac{G_F^2 ME}{\pi} \left((1-y - \frac{M}{2E}xyF'_2 + y^2xF'_1 - y(1 - \frac{1}{2}y)xF'_3) \right). \tag{2.11}$$

We now define the limit $Q^2, \nu \rightarrow \infty$ with x fixed, the so-called Bjorken limit, and it is observed that in this limit that the structure function depends only on x , i.e. to a good approximation it does not depend on Q^2 ,

$$F_i(x, Q^2) \rightarrow F_i(x). \tag{2.12}$$

This implies that the virtual photons interact with pointlike particles inside the proton, since otherwise there would be a dependence on Q . If we consider the limit for a highly energetic proton, and consider that the photon scatters off a pointlike quark inside the proton moving parallel to it (i.e. with no transverse momentum) and carrying a fraction ξ of its momentum we can rewrite eq. (2.10) as

$$\frac{d^2\sigma}{dx dy} = \frac{4\pi\alpha^2 ME}{Q^4} \times \left((1 + (1-y)^2)F_1 + \frac{1}{x}(1-y)(F_2 - 2xF_1) - (M/2E)xyF_2 \right). \tag{2.13}$$

On the other hand one can compute the process $e^-q \rightarrow e^-q$, and using the usual Mandelstam variables one obtains

$$\sum |\bar{M}|^2 = 2e_q^2 e^4 \frac{s^2 + u^2}{t^2}, \tag{2.14}$$

and therefore with

$$\frac{d\sigma}{dt} = \frac{1}{16\pi s^2} \sum |\bar{M}|^2 \quad (2.15)$$

and substituting the deep inelastic scattering variables $t = -Q^2$, $u = s(y-1)$ and $s = \xi Q^2/(xy)$ the cross section can be expressed as

$$\frac{d\sigma}{dQ^2} = \frac{2\pi\alpha^2 e_q^2}{Q^4} (1 + (1-y)^2). \quad (2.16)$$

Now the mass-shell constraint for the outgoing quark gives

$$p_q'^2 = (p_q + q)^2 = q^2 + 2p_q \cdot q = -2p \cdot q(x - xi) = 0, \quad (2.17)$$

which implies $x = \xi$. By using then $\int_0^1 dx \delta(x - \xi) = 1$ we finally obtain

$$\frac{d^2\sigma}{dx dQ^2} = \frac{4\pi\alpha^2}{Q^4} (1 + (1-y)^2) \frac{1}{2} e_q^2 \delta(x - \xi). \quad (2.18)$$

By comparing now eqs. (2.10) and (2.18) we can get the structure functions as

$$F_2 = x e_q^2 \delta(x - \xi) \quad (2.19)$$

for F_2 and similarly for F_1

$$F_1 = e_q^2 \delta(x - \xi), \quad (2.20)$$

i.e., $F_2 = 2xF_1$.

We can interpret $F_2(x)$ as proving a quark inside the proton with momentum fraction $x = \xi$, which gives raise to the so-called *naive parton model*, where $q(\xi)d\xi$ represents the probability that a quark carries momentum fraction in $[\xi, \xi + d\xi]$ for $0 \leq \xi \leq 1$, and the photon interacts incoherently with the quark inside the proton with the corresponding momentum fraction.

Thus we can obtain the proton structure functions by integrating the quark distribution functions with the quark probability,

$$F_2(x) = 2xF_1(x) = \sum_{q,\bar{q}} \int_0^1 d\xi q(\xi) x e_q^2 \delta(x - \xi) = \sum_{q,\bar{q}} e_q^2 x q(x). \quad (2.21)$$

In QCD the naive parton model is broken. In particular, the assumption that quarks have negligible transverse momentum does not hold, since a quark can emit a gluon and acquire transverse momentum k_T which can be large with probability $\sim \alpha_S dk_T^2/k_T^2$ for large k_T , up to the kinematical limit $k_T^2 \sim Q^2$ giving rise to logarithmic contributions of the form $\alpha_S \log Q^2$ breaking the Bjorken scaling where the structure function does not depend on Q in the limit $Q^2 \rightarrow \infty$ with x fixed. We will now compute these corrections to the structure function obtained in eq. (2.19) and obtain the

QCD parton model, since it will be useful to understand certain aspects of the parton distribution functions as used in collider phenomenology.

If we consider a free quark with momentum p (i.e. setting $\xi = 1$)

$$\gamma^*(q) + q(p) \rightarrow q(l) \quad (2.22)$$

where we have shown the four-momenta in brackets for the corresponding particles. The matrix element is trivially given by

$$\mathcal{M}_\alpha = -ie_q \bar{u}(l) \gamma^\alpha u(p), \quad (2.23)$$

so when summed and averaged over spins and colors we obtain

$$n^\alpha n^\beta \sum |\bar{M}_{\alpha\beta}|^2 = 4e_q^2, \quad (2.24)$$

where we have projected out the F_2 contribution, and which together with the phase space

$$d\Phi_1 = 2\pi \delta((p+q)^2), \quad (2.25)$$

and finally inserting the flux factor $1/(4\pi)$ gives us the structure function

$$F_2(x) = e_q^2 \delta(1-x) \quad (2.26)$$

which corresponds to the naive parton model with $\xi = 1$, as expected.

First we consider the real gluon emissions. In particular we start with the leftmost diagram. The invariant phase space is given in this case by

$$d\Phi_2 = \int \frac{d^4 r}{(2\pi)^2} \frac{d^4 l}{(2\pi)^3} \delta^+(r^2) \delta^+(l^2) (2\pi)^4 \delta^4(p+q-r-l), \quad (2.27)$$

and introducing k^μ for the parton line we obtain

$$d\Phi_2 = \frac{1}{4\pi^2} \int d^4 k \delta^+((p-k)^2) \delta^+((k+q)^2). \quad (2.28)$$

We can express k^μ as

$$k^\mu = \xi p^\mu + \frac{k_\Gamma^2 - |k^2|}{2\xi} n^\mu + k_\Gamma^\mu, \quad (2.29)$$

$$d^4 k = \frac{d\xi}{d2\xi} dk^2 d^2 k_\Gamma \quad (2.30)$$

from which we can obtain

$$(p-k)^2 = (1-\xi) \frac{|k^2|}{\xi} - \frac{k_\Gamma^2}{\xi}, \quad (2.31)$$

$$(k+q)^2 = 2\xi\nu - Q^2 - |k^2| - 2q_\Gamma \cdot k_\Gamma, \quad (2.32)$$

which let us rewrite the phase space in eq. (2.28) in the form

$$d\Phi_2 = \frac{1}{16\nu\pi^2} \int d\xi dk^2 dk_T^2 d\theta (k_T^2 - (1-\xi)|k^2|) \times \delta\left(\xi - x - \frac{|k|^2 + 2q_T \cdot k_T}{2\nu}\right) \quad (2.33)$$

with $0 < \theta < \pi$.

We now obtain the matrix element, which is given by

$$\mathcal{M}^\alpha = -ig_e e_q \bar{u}(l) \gamma^\alpha \frac{1}{\not{k}} \not{\epsilon} t^A u(p), \quad (2.34)$$

which after summing and averaging spins and colors, gives

$$\sum |\mathcal{M}|_{\alpha\beta}^2 = \frac{1}{2} e_q^2 g^2 \sum C_F \text{Tr}(\gamma^\beta (\not{k} + \not{q}) \gamma^\alpha \not{k} \not{\epsilon} \not{\epsilon}^* \not{k}) \frac{1}{k^4}. \quad (2.35)$$

Projecting out again the F_2 contribution we obtain

$$\frac{1}{4\pi} n^\alpha n^\beta \sum |\mathcal{M}|_{\alpha\beta}^2 = \frac{8e_q^2 \alpha_S}{|k^2|} \xi P(\xi), \quad (2.36)$$

where we have used the splitting function $P(\xi)$

$$P(\xi) = C_F \frac{1\xi^2}{1-\xi^2}, \quad (2.37)$$

of the QCD $q\bar{q}g$ vertex. Now combining together eqs. (2.28) and (2.37) and performing the integrations over k_T^2 and θ we obtain

$$F_2 = e_q^2 \frac{\alpha_S}{2\pi^2} \int_0^{2\nu} \frac{d|k^2|}{|k^2|} \int_{\xi_-}^{\xi_+} d\xi \frac{\xi P(\xi)}{\sqrt{(\xi_+ - \xi)(\xi - \xi_-)}} \quad (2.38)$$

where we have defined the ξ_\pm functions

$$\xi_\pm(z, x) = x + z - 2zx \pm \sqrt{4x(1-x)z(1-z)} \quad (2.39)$$

together with the $z = |k^2|/(2\nu)$ variable to simplify the notation. It is important at this time that $|k^2|$ is not limited to small values and this leads to a logarithmic divergency at small $|k^2|$. We can most simply use a cutoff κ^2 to regularize this divergence for now, and using the fact that $\lim_{z \rightarrow 0} \xi_\pm = x$ and that

$$\int_{\xi_-}^{\xi_+} d\xi \frac{1}{\sqrt{(\xi_+ - \xi)(\xi - \xi_-)}} = \pi \quad (2.40)$$

we finally obtain

$$F_2|_{\text{div}} = e_q^2 \frac{\alpha_S}{2\pi} x P(x) \int_{\kappa^2}^{2\nu} \frac{d|k^2|}{|k^2|} = e_q^2 \frac{\alpha_S}{2\pi} x P(x) \log\left(\frac{2\nu}{\kappa^2}\right). \quad (2.41)$$

It can be seen that this is the only diagram with a logarithmic divergence contribution, the other diagrams giving a finite contribution to the structure function.

In total, and by using $\log(2\nu) = \log(Q^2) - \log(x)$ the structure function including real corrections is given then by

$$F_2(x, Q^2) = e_q^2 x \left(\delta(1-x) + \frac{\alpha_S}{2\pi} \left(P(x) \log\left(\frac{Q^2}{\kappa^2}\right) + C(x) \right) \right), \quad (2.42)$$

where C is a function which can be computed. This shows that Bjorken scaling is broken at next-to-leading order in the structure function by logarithms $\log Q^2$, which can be seen in the corresponding quark distribution function

$$q(x, Q^2) = \delta(1-x) + \frac{\alpha_S}{2\pi} \left(P(x) \log(Q^2) \frac{\mu^2}{\kappa^2} + C(x) \right). \quad (2.43)$$

At this point we note that this is not the full next-to-leading-order contribution, since virtual corrections are still left. Those contribution can be computed using standard methods, and actually the ultraviolet divergences will cancel in the sum. We will not reproduce here the full computations, but the final result is given by¹

$$q(x, \mu) = q_0(x) \frac{\alpha_S}{2\pi} \int_x^1 \frac{d\xi}{\xi} q_0(\xi) \left(P\left(\frac{x}{\xi}\right) \log \frac{\mu^2}{\kappa^2} + C\left(\frac{x}{\xi}\right) \right) + \dots \quad (2.44)$$

2.2 Resummation

In this section we will introduce the concept of resummation, will investigate why it is necessary and its advantages over fixed-order calculations, and will briefly present the main aspects of the mathematical formalism of threshold and transverse-momentum resummation. Comprehensive reviews on the topic can be found in [7, 8, 9]. This section will also be based on the reviews in [10, 11, 12, 13, 14].

2.2.1 Introduction

Perturbative computations in the QCD framework are typically done at the fixed levels in the α_S parameter which correspond to the different topological families of tree diagrams. The Kinoshita-Lee-Neuenberg theorem [15, 16] guaranteed (given the appropriate assumptions) that the singular infrared contributions of real and virtual nature cancel each other and make the QCD next-to-leading cross section an infrared-safe quantity. However, in given kinematical regions, e.g. $z \rightarrow 1$ and $p_T \rightarrow 0$ (which will later give rise to

¹The full derivation is in [1].

threshold and transverse-momentum resummation, respectively) these cancellations are constrained and potentially large logarithms are left in the partonic cross sections, eventually spoiling the convergence of the magnitudes. This can be seen for example in the case $z \rightarrow 1$ as in the case of massive particles, close to the threshold the available phase space for the real emission is limited and only allows for soft emission. If we compute the fixed-order cross section at $\mathcal{O}(\alpha_S)$ we can easily find that it will be proportional to

$$\mathcal{M} \propto \frac{1}{(p-k)^2} = -\frac{1}{2p \cdot k} = -\frac{1}{2p_0 k_0 (1 - \cos \theta)}, \quad (2.45)$$

where we can see that this can lead to divergencies in the limits $k \rightarrow 0$ (soft emission) and $\theta \rightarrow 0$ (collinear emission). It is important to note that collider detectors cannot detect either of those limits: in the former case because of the low energy of the emission and in the latter one because of collinearity with the beam, meaning we need to include those two contributions to our formally $2 \rightarrow 2$ process calculation.

When integrating this matrix element together with the corresponding phase space we obtain something of the form:

$$\alpha_S \int \frac{d^4 k}{(2\pi^4)} \frac{p \cdot p'}{p \cdot k p' \cdot k} \propto \alpha_S \int \frac{dp_0}{p_0} \int \frac{d\theta}{\theta} \propto \alpha_S \log^2(\dots). \quad (2.46)$$

If we now apply dimensional regularization to (2.46) as is usual we obtain

$$\alpha_S \int \frac{d^{4-2\epsilon} k}{(2\pi^4)} \frac{p \cdot p'}{p \cdot k p' \cdot k} \propto \alpha_S \int \frac{dp_0 p_0^{-\epsilon}}{p_0} \int \frac{d\theta \sin^{-\epsilon} \theta}{\theta} \propto \alpha_S \left(\frac{1}{\epsilon} + \log^2(\dots) \right), \quad (2.47)$$

where the double logarithm is due to the both soft and collinear contributions.

Although what we have seen holds at the $\mathcal{O}(\alpha_S)$ level, it can be shown that the same pattern follows to all orders. In a simplified way, we can write the cross section as

$$\sigma \propto 1 + \alpha_S(L^2 + L + 1) + \alpha_S^2(L^4 + L^3 + L^2 + L + 1) + \dots, \quad (2.48)$$

where the 1 terms mean some constant non-dependent on α_S and the L terms are the logarithmic ones, whose particular form depend of the particular kinematical region.

The aim of resummation is to sum some of the logarithmic contributions to all orders in α_S . As we will see this restores the convergence properties of the series as well as improved the overall precision of the cross section computation, reducing the dependencies on the arbitrary physical factorization and renormalization scales μ_F and μ_R . This is done by exponentiating the

elements in (2.48) to different resummation orders. Again schematically we obtain something of the form

$$\begin{aligned}\sigma &\propto 1 + \alpha_S(L^2 + L + 1) + \alpha_S^2(L^4 + L^3 + L^2 + L + 1) + \dots \\ &= \exp(Lg_1(\alpha_S L) + g_2(\alpha_S L) + \alpha_S g_3(\alpha_S L) + \dots) C(\alpha_S),\end{aligned}\quad (2.49)$$

where g_1 sums at the leading-log (LL) order, g_2 corresponds to the next-to-leading-log order (NLL), etc., and some suppressed terms are neglected.

We will now review the particular application of this idea to the threshold and transverse momentum cases.

2.2.2 Threshold resummation

When computing cross section in the perturbative QCD paradigm we normally consider one physical scale that is used for the arbitrary renormalization and factorization scales. We normally set those scales μ_R and μ_F , e.g. in the case of the Drell-Yan process to the invariant mass of the process M . However in some kinematical regions we may have a two-scale process and after the cancelation of the soft and collinear divergences potentially large logarithms remain [7].

Process illustration

Before doing the real threshold calculation we will show the process and ideas in a simplified manner. After that will present the different steps into more details. For illustration, let us consider an infrared-sensitive quantity depending on two scales M and m , $R(M^2, m^2)$. In this case, M will be the hard scale of the process while m measures the distance to a critical kinematical region. The first step as we will later see in detail will be the factorization of the quantity into a hard part H and soft part S ,

$$R(M^2, m^2) = H(M^2/\mu^2)S(m^2/\mu^2),\quad (2.50)$$

where we have introduced a factorization scale μ . The hard function H will contain the information about the hard process while the soft part S contains the long-distance behavior. It is important to notice that such a factorization can be very non-trivial in real processes [7] and that will usually hold in a transformed space of the original variables, e.g. the Mellin space. If we set the scale $\mu = M$ we will obtain very large logarithmic contributions in S , spoiling the convergence of the series even in the case of small α_S . We will investigate in this section the specific forms of these logarithms. It is the part S that we will try to resum in the soft limit.

To accomplish this we will first note that from the dependencies of H and S we can write the evolution equations

$$\frac{dH}{d \log \mu^2} = -\frac{dS}{d \log \mu^2} =: \gamma_S(\mu^2),\quad (2.51)$$

where we have defined the anomalous dimensions γ_S . We can now solve this equation by using separation of variables to obtain

$$S(m^2/\mu^2) = S(1) \exp\left(-\int_{m^2}^{\mu^2} \frac{dq^2}{q^2} \gamma_S(q^2)\right). \quad (2.52)$$

By now choosing the scale $\mu = M$ we obtain the resummed result

$$R(M^2, m^2) = H(1)S(1) \exp\left(-\int_{m^2}^{M^2} \frac{dq^2}{q^2} \gamma_S(q^2)\right), \quad (2.53)$$

where we can see that we no longer have the potentially large logarithms in the H and S terms so they can be computed safely in the perturbation theory framework. The exponential factor in (2.53) is the Sudakov factor which can be computed up to the different resummation orders.

Factorization

We will apply now these ideas to the case of threshold resummation. As discussed, when $z \rightarrow 1$ we obtain potentially large logarithms in the fixed-order cross section of the form

$$\alpha_S^n \left(\frac{\log^m(1-z)}{1-z}\right)_+, \quad (2.54)$$

where $m \leq 2n - 1$.

Let us consider then the doubly differential hadronic cross section

$$M^2 \frac{d^2\sigma_{AB}}{dM^2 dp_T^2}(\tau) = \sum_{ab} \int_0^1 dx_a \int_0^1 dx_b x_a f_{a/A}(x_a, \mu^2) x_b f_{b/B}(x_b, \mu^2) \\ \times z \hat{\sigma}_{ab}(z, M^2, M^2/p_T^2, M^2/\mu^2) \delta(\tau - x_a x_b z), \quad (2.55)$$

where $\tau := M^2 \hat{s}$. We can rewrite this by using the Mellin transformation

$$\tilde{F}(N) := \int_0^1 dx^{N-1} F(X) \quad (2.56)$$

into

$$M^2 \frac{d\sigma_{AB}}{dM^2 dp_T^2}(N-1) = \sum_{ab} f_{a/A}(N, \mu^2) f_{b/B}(N, \mu^2) \\ \times \hat{\sigma}_{ab}(N, M^2, M^2/p_T^2, M^2/\mu^2), \quad (2.57)$$

where we have used the slight abuse of notation $\tilde{F}(N) \equiv F(N)$ to simplify the notation.

The partonic cross section can also be written in the Mellin space as

$$M^2 \frac{d\sigma_{ab}}{dM^2 dp_T^2}(N-1) = \sum_{cd} \phi_{c/a}(N, \mu^2) \phi_{d/b}(N, \mu^2) \times \hat{\sigma}_{cd}(N, M^2, M^2/p_T^2, M^2/\mu^2), \quad (2.58)$$

with $\phi_{c/a}(x_c, \mu^2)$ the parton-in-parton distribution of parton c in parton d .

The evolution of the ϕ functions are given as a function of μ by the Altarelli-Parisi equation [17]

$$\frac{\partial \phi_{c/a}(N, \mu^2)}{\partial \log \mu^2} = \sum_b P_{cb}(N, a_S(\mu^2)) \phi_{b/a}(N, \mu^2), \quad (2.59)$$

where P_{cb} are the splitting functions, which can be calculated in perturbation theory. The LO values are given by:

$$P_{qq}^{(\text{LO})}(N) = C_F \left(\frac{3}{2} + \frac{1}{N(N+1)} - 2 \sum_{k=1}^N \frac{1}{k} \right), \quad (2.60)$$

$$P_{qg}^{(\text{LO})}(N) = \frac{1}{2} \left(\frac{2+N+N^2}{N(N+1)(N+2)} \right), \quad (2.61)$$

$$P_{gq}^{(\text{LO})}(N) = C_F \left(\frac{2+N+N^2}{N(N^2-1)} \right), \quad (2.62)$$

$$P_{gg}^{(\text{LO})}(N) = \beta_0 + 2C_A \left(\frac{1}{N(N-1)} + \frac{1}{(N+1)(N+2)} - \sum_{k=1}^N \frac{1}{k} \right). \quad (2.63)$$

As a mathematical tool we now introduce the QCD evolution operator $E_{ab}(N, \mu^2, \mu_0^2)$, defined as:

$$\frac{\partial E_{ab}(N, \mu^2, \mu_0^2)}{\partial \log \mu^2} = \sum_c P_{ac}(N, a_S(\mu^2)) E_{cb}(N, \mu^2, \mu_0^2). \quad (2.64)$$

With this we can rewrite the Altarelli-Parisi equation in the form:

$$\phi_{c/a}(N, \mu^2) = \sum_b E_{cb}(N, \mu^2, \mu_0^2) \phi_{b/a}(N, \mu_0^2). \quad (2.65)$$

The Mellin transformation of the logarithmic terms we want to resum is given by

$$\left(\frac{\log^m(1-z)}{(1-z)} \right)_+ \rightarrow \log^{m+1} N + \dots. \quad (2.66)$$

If we keep the leading terms in N and ignore $\mathcal{O}(1/n)$ contributions in the splitting functions, we can find the behavior of Eqs. (2.60)-(2.63) in the

$\log N \rightarrow \infty$ limit as:

$$P_{qq}^{(\text{LO})}(N) = C_F \left(\frac{3}{2} - 2 \log \bar{N} \right) + \mathcal{O} \left(\frac{1}{\bar{N}} \right), \quad (2.67)$$

$$P_{gg}^{(\text{LO})}(N) \sim \frac{1}{2\bar{N}}, \quad (2.68)$$

$$P_{gq}^{(\text{LO})}(N) \sim \frac{C_F}{\bar{N}}, \quad (2.69)$$

$$P_{gq}^{(\text{LO})}(N) = \beta_0 - 2C_A \log \bar{N} + \mathcal{O} \left(\frac{1}{\bar{N}} \right), \quad (2.70)$$

where $\bar{N} = Ne^{\gamma_E}$ and γ_E the Euler constant.

From Eqs. (2.67)-(2.70) we see that the mixing contributions can be ignored at leading order in N , which together with Eq. (2.58) integrated over p_T leads to

$$M^2 \frac{d\sigma_{ab}}{dM^2}(N-1) = \phi_{a/a}(N, \mu^2) \phi_{b/b}(N, \mu^2) \hat{\sigma}_{ab}(N, M^2, M^2/\mu^2) + \mathcal{O} \left(\frac{1}{\bar{N}} \right). \quad (2.71)$$

It can be shown that (2.71) can be factorized [8] into

$$M^2 \frac{d\sigma_{ab}}{dM^2}(N-1) = \psi_{a/a}(N, M^2) \psi_{b/b}(N, M^2) \times H_{ab}(M^2, M^2/\mu^2) S_{ab}(N, M^2/\mu^2) + \mathcal{O} \left(\frac{1}{\bar{N}} \right), \quad (2.72)$$

where the H_{ab} function is infrared-safe and independent of N , so it can be computed perturbatively as

$$H_{ab}(M^2, M^2/\mu^2) = \sum_{n=0}^{\infty} a_S^n H_{ab}^{(n)}(M^2, M^2/\mu^2), \quad (2.73)$$

the parton-in-parton distributions ψ are dependent on the invariant mass M instead of the scale μ and satisfy in this case the evolution equations

$$\frac{\partial \psi_{a/a}(N, M^2)}{\partial \log M^2} = \gamma_a(a_S(M^2)) \psi_{a/a}(N, M^2), \quad (2.74)$$

with γ_a the anomalous dimension, given perturbatively by

$$\gamma_a(a_S) = \frac{1}{Z_a} \frac{\partial Z_a}{\partial \log \mu^2} = \sum_n a_S^n \gamma_a^{(n)}, \quad (2.75)$$

and corresponds to the N -independent virtual terms in $P_{aa}(N, a_S)$. The function S_{ab} corresponds in turn to the large-angle emission of soft gluons and can be computed in the eikonal approximation.

From (2.50) and (2.72) we can obtain

$$\begin{aligned} \hat{\sigma}_{ab}(N, M^2, M^2/\mu^2) &= \frac{\psi_{a/a}(N, M^2)\psi_{b/b}(N, M^2)}{\phi_{a/a}(N, \mu^2)\phi_{b/b}(N, \mu^2)} \\ &\times S_{ab}(N, M^2/\mu^2)H_{ab}(M^2, M^2/\mu^2) + \mathcal{O}\left(\frac{1}{N}\right). \end{aligned} \quad (2.76)$$

By solving then the evolution equations for ϕ, ψ in the threshold limit and using gauge invariance and renormalization group equations, and the exponentiation of the eikonal function, the cross section can be then written as

$$\hat{\sigma}_{ab}(N, M^2, M^2/\mu^2) = H_{ab}(M^2, M^2/\mu^2) \exp(G_{ab}(N, M^2, M^2/\mu^2)) + \mathcal{O}\left(\frac{1}{N}\right), \quad (2.77)$$

with

$$\begin{aligned} G_{ab}(N, M^2, M^2/\mu^2) &= \log \Delta_a(N, M^2, M^2/\mu^2) \\ &+ \log \Delta_b(N, M^2, M^2/\mu^2) \\ &+ \log \Delta_{ab}(N, M^2, M^2/\mu^2), \end{aligned} \quad (2.78)$$

where

$$\log \Delta_a(N, M^2, M^2/\mu^2) = \int_0^1 dz \frac{z^{N-1} - 1}{1-z} \int_{\mu^2}^{(1-z)^2 M^2} \frac{dq^2}{q^2} A_a(a_S(q^2)), \quad (2.79)$$

$$\log \Delta_{ab}(N, M^2, M^2/\mu^2) = \int_0^1 dz \frac{z^{N-1} - 1}{1-z} D_{ab}(a_S((1-z)^2 M^2)). \quad (2.80)$$

The soft collinear gluon radiation from parton a is here included in A_a which is calculable perturbatively and the large-angle soft gluon emission contributions are included in D_{ab} also perturbatively calculable.

Introducing the integrated (2.79) and (2.80) into (2.53) we obtain

$$\begin{aligned} \hat{\sigma}_{ab}(N, M^2, M^2/\mu^2) &= \mathcal{H}_{ab}(M^2, M^2/\mu^2) \\ &\times \exp(\mathcal{G}_{ab}(N, M^2, M^2/\mu^2)) + \mathcal{O}\left(\frac{1}{N}\right). \end{aligned} \quad (2.81)$$

This \mathcal{H}_{ab} , as opposed to the hard function H_{ab} , includes the non-logarithmic terms resulting from the integrations:

$$\mathcal{H}_{ab}^{(0)}(M^2, M^2/\mu^2) = H_{ab}^{(0)}(M^2, M^2/\mu^2) \quad (2.82)$$

$$\mathcal{H}_{ab}^{(1)}(M^2, M^2/\mu^2) = H_{ab}^{(1)}(M^2, M^2/\mu^2) + \frac{\pi^2}{6}(A_a^{(1)} + A_b^{(1)})H_{ab}^{(0)}(M^2), \quad (2.83)$$

and \mathcal{G}_{ab} can be shown to have the expansion

$$\mathcal{G}_{ab}(N, M^2, M^2/\mu^2) = \log \bar{N} g_{ab}^{(1)}(\lambda) + g_{ab}^{(1)}(\lambda, M^2/\mu^2) + a_S g_{ab}^{(3)}(\lambda, M^2/\mu^2) + \dots \quad (2.84)$$

with $\lambda = \alpha_S \beta_0 \log \tilde{N}$. The functions $g_{ab}^{(i)}$ determine the order of the resummation result: $g_{ab}^{(1)}$ is the leading logarithm contribution (LL), whereas $g_{ab}^{(2)}$ resums up to the next-to-leading logarithmic order (NLL). Similarly the rest of $g_{ab}^{(i)}$ resum at larger orders.

For reference we will present the values for the $g_{ab}^{(i)}$ necessary for up to NLL resummation [18]

$$\begin{aligned} 2\lambda\beta_0 g_{ab}^{(1)}(\lambda) &= (A_a^{(1)} + A_b^{(1)})(2\lambda + (1 - 2\lambda)\log(1 - 2\lambda)) \quad (2.85) \\ 2\beta_0 g_{ab}^{(2)}(\lambda, M^2/\mu^2) &= (A_a^{(1)} + A_b^{(1)}) \log(1 - 2\lambda) \log \frac{M^2}{\mu^2} \\ &\quad + (A_a^{(1)} + A_b^{(1)}) \frac{\beta_1}{\beta_0^2} (2\lambda + \log(1 - 2\lambda) + \frac{1}{2} \log^2(2 - 2\lambda)) \\ &\quad - (A_a^{(1)} + A_b^{(1)}) \frac{1}{\beta_0} (2\lambda + \log(1 - 2\lambda)) + D_{ab}^{(1)} \log(1 - 2\lambda), \quad (2.86) \end{aligned}$$

with the coefficients

$$A_a^{(1)} = 2C_a, \quad (2.87)$$

$$A_a^{(2)} = 2C_a \left[\left(\frac{67}{18} - \frac{\pi^2}{6} \right) C_A - \frac{5}{9} n_f \right], \quad (2.88)$$

$$D_{ab}^{(1)} = 0, \quad (2.89)$$

where $C_q = C_F$ and $C_g = C_A$.

The function \mathcal{H}_{ab} is then, by comparing (2.81) with the perturbative expansion of $\hat{\sigma}_{ab}$ and identifying terms:

$$\mathcal{H}_{ab}^{(0)}(M^2, M^2/\mu^2) = \hat{\sigma}_{ab}^{(0)}(M^2, M^2/\mu^2), \quad (2.90)$$

$$\mathcal{H}_{ab}^{(1)}(M^2, M^2/\mu^2) = \hat{\sigma}_{ab}^{(0)}(M^2, M^2/\mu^2) \quad (2.91)$$

$$\times (\mathcal{A}_0 + (\delta P_{aa}^{(1)} + \delta P_{bb}^{(1)}) \log \frac{M^2}{\mu^2} + \frac{\pi^2}{6} (A_a^{(1)} + A_b^{(1)})), \quad (2.92)$$

where $\delta P_{aa}^{(1)}$ is the coefficient of the $\delta(1 - x)$ term in the splitting function $P_{aa}^{(1)}$, and \mathcal{A}_0 is the infrared-finite part of the renormalized virtual correction

$$\begin{aligned} M^{\dagger(1)} M^{(0)} + \text{h.c.} &= a_S \left(\frac{4\pi\mu^2}{M^2} \right)^\epsilon \\ &\times \frac{\Gamma(1 - \epsilon)}{\Gamma(1 - 2\epsilon)} \left(\frac{\mathcal{A}_{-2}}{\epsilon^2} + \frac{\mathcal{A}_{-1}}{\epsilon} + \mathcal{A}_0 \right) |M^{(0)}|^2 + \mathcal{O}(\epsilon), \quad (2.93) \end{aligned}$$

where we have used the $\overline{\text{MS}}$ renormalization scheme.

The resummed cross sections are valid near the threshold, but fixed-order predictions are still valid far from this thresholds and must be retained, therefore it is necessary to combine these two values through a matching procedure,

$$\hat{\sigma} = \hat{\sigma}_{\text{res}} + \hat{\sigma}_{\text{f.o.}} - \hat{\sigma}_{\text{exp}}, \quad (2.94)$$

with $\hat{\sigma}_{\text{res}}$, $\hat{\sigma}_{\text{f.o.}}$, $\hat{\sigma}_{\text{exp}}$ the resummed, fixed-order, and expansion results, which corresponds to the resummed cross section expanded to the same order in α_S as the fixed-order result:

$$\begin{aligned} \hat{\sigma}_{ab}^{\text{exp}} &= H_{ab}^{(0)}(M^2, M^2/\mu^2) + a_S H_{ab}^{(1)}(M^2, M^2/\mu^2) \\ &- a_S \left(2L - \log \frac{M^2}{\mu^2} \right) \sum_c (H_{ab}^{(0)}(M^2, M^2/\mu^2) P_{cb}^{(1)}(N) + P_{ca}^{(1)} H_{cb}^{(0)}(M^2, M^2/\mu^2)) \\ &- a_S H_{ab}^{(0)}(M^2, M^2/\mu^2) (L^2(A_a^{(1)} + A_b^{(1)}) + L(B_a^{(1)} + B_b^{(1)})). \end{aligned} \quad (2.95)$$

2.2.3 Transverse momentum resummation

We will now briefly review the resummation procedure to resum potentially large logarithmic terms that appear when computing transverse momentum distributions. These terms have the form

$$a_S^n \left(\frac{\log^m(M^2/p_{\text{T}}^2)}{p_{\text{T}}^2} \right)_+, \quad (2.96)$$

with $m \leq 2n - 1$. This resummation procedure follows the Collins-Soper-Sterman formalism [19].

In this case it is more convenient to work with the usual Fourier transform W_{ab} on the cross section,

$$M^2 \frac{d^2 \sigma_{ab}}{dM^2 dp_{\text{T}}^2}(N) = \int \frac{d^2}{4\pi} e^{i\mathbf{b} \cdot \mathbf{p}_{\text{T}}} W_{ab}(N+1, M^2, M^2 \bar{b}^2, M^2/\mu^2), \quad (2.97)$$

where b is the impact parameter and $\bar{b} := b\gamma_{\text{E}}/w$. After performing the angular part of the integral we obtain

$$M^2 \frac{d^2 \sigma_{ab}}{dM^2 dp_{\text{T}}^2}(N) = \int_0^\infty db \frac{b}{2} W_{ab}(N+1, M^2, M^2 \bar{b}^2, M^2/\mu^2). \quad (2.98)$$

The $p_{\text{T}} \rightarrow 0$ singularities appear as large logarithms for $M\bar{b} \rightarrow \infty$ which take the particular form

$$\left(\frac{1}{p_{\text{T}}^2} \log^n \left(\frac{M^2}{p_{\text{T}}^2} \right) \right)_+ \rightarrow \log^{m+1} M^2 \bar{b}^2 + \dots \quad (2.99)$$

It can be shown [19] that the Fourier-transformed cross section can be factorized as

$$W_{ab}(n, M^2, M^2\bar{b}^2, M^2/\mu^2) = \sum_{c,d} H_{cd}(M^2, M^2/\mu^2) S_{cd}(N, M^2\bar{b}^2) \\ \times P_{c/a}(N, b^2, M^2\bar{b}^2) P_{d/b}(N, b^2, M^2\bar{b}^2) + \mathcal{O}\left(\frac{1}{M^2\bar{b}^2}\right), \quad (2.100)$$

where S_{cd} is an eikonal function describing the soft-gluon emission, $P_{c/a}$ is the parton-in-parton distribution at fixed transverse momentum, and H_{cd} is an infrared-safe hard function, which perturbatively is given by,

$$H_{cd}(M^2, M^2/\mu^2) = \sum_{n=0}^{\infty} a_S^n H_{cd}^{(n)}(M^2, M^2/\mu^2). \quad (2.101)$$

It is also worth noting that although our choice of notation is similar on purpose to the threshold case, the particular definitions of H and S are different in both formalism.

By solving the evolution equations for $P_{c/a}$ we can rewrite W_{ab} as

$$W_{ab}(N, M^2, M^2\bar{b}^2, M^2/\mu^2) = \sum_{c,d} H_{cd}(M^2, M^2/\mu^2) \\ \times P_{c/a}(N, b^2, 1) P_{d/b}(N, b^2, 1) \exp(G_{cd}(M^2, M^2\bar{b}^2, M^2/\mu^2)), \quad (2.102)$$

where the exponent G_{cd} can be written as

$$G_{cd}(M^2, M^2\bar{b}^2, M^2/\mu^2) \\ = -\frac{1}{2} \int_{1/\bar{b}^2}^{M^2} \frac{dq^2}{q^2} \left(A_c(a_S(q^2)) \log\left(\frac{M^2}{q^2}\right) + B_c(a_S(q^2)) \right) + (c \leftrightarrow d), \quad (2.103)$$

and the $P_{c/a}$ functions can be expressed as

$$P_{c/a}(N^2, b, 1) = \sum_c C_{bc}(N, a_S(1/\bar{b}^2)) \phi_{c/a}(N, 1/\bar{b}^2). \quad (2.104)$$

To obtain our final results we now need to perform the inverse Fourier transform for the W_{ab} quantity, and evolve the $\phi_{c/a}$ functions from the scale μ to $1/\bar{b}^2$, which yields

$$\sigma_{ab}(N, M^2, M^2/p_T^2, M^2/\mu^2) \\ = \int_0^\infty db \frac{b}{2} J_0(bp_T) \sum_{c,d,e,f} H_{cd}(M^2, M^2/\mu^2) \exp(G_{cd}(M^2, M^2\bar{b}^2, M^2/\mu^2)) \\ \times C_{ce}(N, a_S(1/\bar{b}^2)) C_{df}(N, a_S(1/\bar{b}^2)) E_{ea}(N, 1/\bar{b}^2, \mu^2) E_{fb}(N, 1/\bar{b}^2, \mu^2). \quad (2.105)$$

The different resummation orders are now given by the perturbative orders of the functions H_{ab}, A_a, B_a, C_{ab} in α_S ,

$$A_a = \sum_{n=1}^{\infty} a_S^n A_a^{(n)}, \quad B_a = \sum_{n=1}^{\infty} a_S^n B_a^{(n)}, \quad C_{ab}(N) = \delta_{ab} + \sum_{n=1}^{\infty} a_S^n C_{ab}^{(n)}(N), \quad (2.106)$$

where the LL accuracy is given by the $H_{ab}^{(0)}, A_a^{(1)}$ terms, the NLL precision requires also $H_{ab}^{(1)}, A_a^{(2)}, B_a^{(1)}, C_{ab}^{(1)}$ and the NNLL order would also require the $H_{ab}^{(2)}, A_a^{(3)}, B_a^{(2)}, C_{ab}^{(2)}$ terms.

After performing the integral in (2.103) we obtain

$$G_{ab}(m^2, M^2 \bar{b}^2, M^2/\mu^2) = \log(M^2 \bar{b}^2 g_{ab}^{(1)}(\lambda)) + g_{ab}^{(2)}(\lambda, M^2/\mu^2) + \dots, \quad (2.107)$$

with $\lambda := \alpha_S \beta_0 \log(M^2 \bar{b}^2)$. The function $g_{ab}^{(1)}$ resums up to LL and the $g_{ab}^{(2)}$ corresponds to the NLL contributions. These are given by

$$\begin{aligned} 2\lambda g_{ab}^{(1)}(\lambda) &= (A_a^{(1)} + A_b^{(1)})(\lambda + \log(1 - \lambda)), \quad (2.108) \\ 2\beta_0 g_{ab}^{(2)}(\lambda, M^2/\mu^2) &= (A_a^{(1)} + A_b^{(1)}) \left(\frac{\lambda}{1 - \lambda} + \log(1 - \lambda) \right) \log\left(\frac{M^2}{\mu^2}\right) \\ &\quad + (A_a^{(1)} + A_b^{(1)}) \frac{\beta_1}{\beta_0} \left(\frac{\lambda + \log(1 - \lambda)}{1 - \lambda} + \frac{1}{2} \log^2(1 - \lambda) \right) \\ &\quad - (A_a^{(2)} + A_b^{(2)}) \frac{1}{\beta_0} \left(\frac{\lambda}{1 - \lambda} + \log(1 - \lambda) \right) \\ &\quad + (B_a^{(1)} + B_b^{(1)}) \log(1 - \lambda), \quad (2.109) \end{aligned}$$

where the values for $A_a^{(i)}, B_a^{(i)}$ are the same as for threshold resummation. Differently from the threshold case, the functions $H_{ab}^{(1)}, C_{ab}^{(1)}, B_a^{(2)}$ are not unique [20] and a consistent set must be chosen. We will use the factors as originally chosen [19, 21, 22], which are given by

$$H_{ab}(M^2, M^2/\mu^2) = \sigma_{ab}^{(0)}(M^2, M^2/\mu^2), \quad (2.110)$$

$$B_a^{(2)} = -2\delta P_{aa}^{(2)} + \beta_0 \left(\frac{2\pi^2}{3} C_a + \mathcal{A}_0 \right), \quad (2.111)$$

$$C_{ab}^{(1)}(N) = \delta_{ab} \left(C_a \frac{\pi^2}{6} + \frac{1}{2} \mathcal{A}_0 \right) - [P_{ab}^{(1)}(N)]_\epsilon, \quad (2.112)$$

where $[P_{ab}^{(1)}(N)]_\epsilon$ is the $\mathcal{O}(\epsilon)$ terms in the expansion of $P_{ab}^{(1)}$ and the other factors coincide with the threshold case.

Finally it is also necessary to perform the fixed order matching as before,

$$\hat{\sigma} = \hat{\sigma}_{\text{res}} + \hat{\sigma}_{\text{f.o.}} - \hat{\sigma}_{\text{exp}}, \quad (2.113)$$

which in this case is given by

$$\begin{aligned}
\hat{\sigma}_{ab}^{\text{exp}}(n, M^2, M^2/p_{\text{T}}^2, M^2/\mu^2) &= H_{ab}^{(0)}(M^2, M^2/\mu^2) + a_{\text{S}} H_{ab}^{(1)}(M^2, M^2/\mu^2) \\
&- a_{\text{S}} \left(\mathcal{J} - \log \frac{M^2}{\mu^2} \right) \sum_c (H_{ac}^{(0)}(M^2, M^2/\mu^2) P_{cb}^{(1)}(N) + P_{ca}^{(1)}(N) H_{cb}(M^2, M^2/\mu^2)) \\
&+ a_{\text{S}} \sum_c (H_{ac}^{(0)}(M^2, M^2/\mu^2) C_{cb}^{(1)}(N) + C_{ca}^{(1)}(N) H_{cb}^{(0)}(M^2, M^2/\mu^2)) \\
&- a_{\text{S}} H_{ab}^{(0)}(M^2, M^2/\mu^2) \left(\frac{\mathcal{J}^2}{4} (A_a^{(1)} + A_b^{(1)}) + \frac{\mathcal{J}}{2} (B_a^{(1)} + B_b^{(1)}) \right), \quad (2.114)
\end{aligned}$$

where

$$\mathcal{J} := \frac{1}{2} \int_0^\infty db J_0(bp_{\text{T}}) \log(M^2 b^2). \quad (2.115)$$

2.3 Supersymmetry

In this section we will present the basic ideas and formulations of supersymmetry. We will first introduce the necessary components to build the supersymmetry lagrangian and later will use this to build and analyze the supersymmetric gaugino sector. For further details the reader is referred to [23].

2.3.1 Introduction

As we have seen, the possibilities to extend the spacetime symmetries of the Standard Model are severely constrained if we are to remain in a consistent Quantum Field Theory. In particular, if we are to remain in a four-dimensional spacetime outside conformal theories the Haag-Lopuszanski-Sonius theorem [24], which is based on the Coleman-Mandula theorem [25] restrict that for realistic theories including chiral fermions the generators Q and Q^\dagger must satisfy the anticommutation relations

$$\begin{aligned}
\{Q, Q^\dagger\} &= P^\mu, \\
\{Q, Q\} &= \{Q^\dagger, Q^\dagger\} = 0, \\
[P^\mu, Q] &= [P^\mu, Q^\dagger] = 0, \quad (2.116)
\end{aligned}$$

where P^μ is the generator of spacetime translations. We can note here that as we know that P^μ transforms as a spin-1 object, the supersymmetry generators Q, Q^\dagger act as spin-1/2 objects. These generators also commute with the gauge transformation generators.

2.3.2 Construction of the supersymmetric lagrangian

We will introduce the formalism of supersymmetry using the superspace framework. We will introduce the basic of the superspace algebra, and introduce the construction of the different supersymmetry lagrangian by parts. We will follow the construction of [23] and references therein.

Superspace

The superspace is a manifold which extends the spacetime usual bosonic coordinates t, x, y, z by adding four fermionic coordinates such that points are determined by

$$x^\mu, \theta^\alpha, \theta^\dagger_{\dot{\alpha}}, \quad (2.117)$$

where the coordinates $\theta^\alpha, \theta^\dagger_{\dot{\alpha}}$ are complex anticommuting two-component spinors.

A general superspace will therefore be a function of these superfields. We can expand such a function in a power series in the θ, θ^\dagger . However, since $\theta^{(\dagger)}$ is anticommuting this expansion can be simplified. In particular, if we consider a general anticommuting variable η we know that $\eta^2 = 0$, which means that the series expansion always terminates:

$$f(\eta) = f_0 + \eta f_1, \quad (2.118)$$

from which is easy to see that $\frac{d\eta}{d\eta} = f_1$ and similarly $\int d\eta f(\eta) = f_1$, and in particular that integration and differentiation are the same for functions of an anticommuting variable.

Going back to the superpotential, we can use this fact to write:

$$S(x, \theta, \theta^\dagger) = \alpha + \theta\xi + \theta^\dagger\chi^\dagger + \theta\theta b + \theta^\dagger\theta^\dagger c + \theta^\dagger\bar{\sigma}^\mu\theta v_\mu + \theta^\dagger\theta^\dagger\theta\eta + \theta\theta\theta^\dagger\zeta^\dagger + \theta\theta\theta^\dagger\theta^\dagger d, \quad (2.119)$$

where we have also used the fact that

$$\begin{aligned} \theta_\alpha &= \frac{1}{2}\epsilon_{\alpha\beta}\theta\theta, \\ \theta^\dagger_{\dot{\alpha}}\theta^\dagger_{\dot{\beta}} &= \frac{1}{2}\epsilon_{\dot{\beta}\dot{\alpha}}\theta^\dagger\theta^\dagger, \\ \theta_\alpha\theta^\dagger_{\dot{\beta}} &= \frac{1}{2}\sigma^\mu_{\alpha\dot{\beta}}(\theta^\dagger\bar{\sigma}_\mu\theta). \end{aligned} \quad (2.120)$$

The superfield S as we have writte could be either commuting or anticommuting, and in general could carry additional Lorentz or spinor indices, from in this whole section we will assume the simpler case without Grassman-odd or extra indices information. In that case we can observe that we have eight bosonic fields a, b, c, d as well as four fermionic fields $\xi, \chi^\dagger, \eta, \zeta^\dagger$. In particular we observe that both bosonic and fermionic degrees of freedom are the same (16 real degrees of freedom). However in general this will be as we

will see a reducible representation of the supersymmetry. Chiral and vector superfields will then be obtained by imposing additional constraints.

Derivatives with respect to the anticommuting coordinates which will be further needed for the construction are defined as:

$$\frac{\partial\theta^\beta}{\partial\theta^\alpha} = \delta_\alpha^\beta, \quad \frac{\partial\theta^\dagger_{\dot{\beta}}}{\partial\theta^\alpha} = 0, \quad \frac{\partial\theta^\dagger_{\dot{\alpha}}}{\partial\theta^\dagger_{\dot{\beta}}} = \delta_{\dot{\beta}}^{\dot{\alpha}}, \quad \frac{\partial\theta^\beta}{\partial\theta^\dagger_{\dot{\alpha}}} = 0. \quad (2.121)$$

Using these, we can define the supersymmetry generators as:

$$\begin{aligned} \hat{Q}_\alpha &= i\frac{\partial}{\partial\theta^\alpha} - (\sigma^\mu\theta^\dagger)_\alpha\partial_\mu, \\ \hat{Q}^\alpha &= -i\frac{\partial}{\partial\theta_\alpha} + (\theta^\dagger\bar{\sigma}^\mu)^\alpha\partial_\mu, \\ \hat{Q}^\dagger_{\dot{\alpha}} &= i\frac{\partial}{\partial\theta^\dagger_{\dot{\alpha}}} - (\bar{\sigma}^\mu\theta)_{\dot{\alpha}}\partial_\mu \\ \hat{Q}_{\dot{\alpha}}^\dagger &= -i\frac{\partial}{\partial\theta^\dagger_{\dot{\alpha}}} + (\theta\sigma^\mu)_{\dot{\alpha}}\partial_\mu. \end{aligned} \quad (2.122)$$

With these, we can obtain the infinitesimal supersymmetry transformation for a superfield S through a series expansion in $\epsilon, \epsilon^\dagger$ as

$$\begin{aligned} \sqrt{2}\delta_\epsilon S &= -i(\epsilon\hat{Q} + \epsilon^\dagger\hat{Q}^\dagger)S = \left(\epsilon^\alpha\frac{\partial}{\partial\theta^\alpha} + \epsilon^\dagger_{\dot{\alpha}}\frac{\partial}{\partial\theta^\dagger_{\dot{\alpha}}} + i(\epsilon\sigma^\mu\theta^\dagger + \epsilon^\dagger\bar{\sigma}^\mu\theta)\partial_\mu \right) S \\ &= S(x^\mu + i\epsilon\sigma^\mu\theta^\dagger + i\epsilon^\dagger\bar{\sigma}^\mu\theta, \theta + \epsilon, \theta^\dagger + \epsilon^\dagger) - S(x^\mu, \theta, \theta^\dagger). \end{aligned} \quad (2.123)$$

Equation (2.123) can be interpreted as a superspace translation

$$\begin{aligned} \theta^\alpha &\rightarrow \theta^\alpha + \epsilon^\alpha, \\ \theta^\dagger_{\dot{\alpha}} &\rightarrow \theta^\dagger_{\dot{\alpha}} + \epsilon^\dagger_{\dot{\alpha}}, \\ x^\mu &\rightarrow x^\mu + i\epsilon\sigma^\mu\theta^\dagger + i\epsilon^\dagger\bar{\sigma}^\mu\theta. \end{aligned} \quad (2.124)$$

Using this we can obtain the transformation of all the fields in the general

superfield S

$$\begin{aligned}
\sqrt{2}\delta_\epsilon a &= \epsilon\xi + \epsilon^\dagger\chi^\dagger \\
\sqrt{2}\delta_\epsilon\xi_\alpha &= 2\epsilon_\alpha b - (\sigma^\mu\epsilon^\dagger)_\alpha(v_\mu + i\partial_\mu a), \\
\sqrt{2}\delta_\epsilon\chi^{\dagger\dot{\alpha}} &= 2\epsilon^{\dagger\dot{\alpha}}c + (\bar{\sigma}^\mu\epsilon)^{\dot{\alpha}}(v_\mu + i\partial_\mu a), \\
\sqrt{2}\delta_\epsilon b &= \epsilon^\dagger\zeta^\dagger - \frac{i}{2}\epsilon^\dagger\bar{\sigma}^\mu\partial_\mu\chi, \\
\sqrt{2}\delta_\epsilon c &= \epsilon\eta - \frac{i}{2}\epsilon\sigma^\mu\partial_\mu\chi^\dagger, \\
\sqrt{2}\delta_\epsilon v^\mu &= \epsilon\sigma^\mu\zeta^\dagger - \epsilon^\dagger\bar{\sigma}^\mu\eta - \frac{i}{2}\epsilon\sigma^\nu\bar{\sigma}^\mu\partial_\nu\xi + \frac{i}{2}\epsilon^\dagger\bar{\sigma}^\mu\partial_\nu\chi^\dagger, \\
\sqrt{2}\delta_\epsilon\eta_\alpha &= 2\epsilon_\alpha d - i(\sigma^\mu\epsilon^\dagger)_\alpha\partial_\mu c - \frac{i}{2}(\sigma^\nu\bar{\sigma}^\mu\epsilon)_\alpha\partial_\mu v_\nu, \\
\sqrt{2}\delta_\epsilon\zeta^{\dagger\dot{\alpha}} &= 2\epsilon^{\dagger\dot{\alpha}}d - i(\bar{\sigma}^\mu\epsilon)^{\dot{\alpha}}\partial_\mu b + \frac{i}{2}(\bar{\sigma}^\nu\sigma^\mu\epsilon^\dagger)^{\dot{\alpha}}\partial_\mu v_\nu, \\
\sqrt{2}\delta_\epsilon d &= -\frac{i}{2}\epsilon^\dagger\bar{\sigma}^\mu\partial_\mu\eta - \frac{i}{2}\epsilon\sigma^\mu\partial_\mu\zeta^\dagger.
\end{aligned} \tag{2.125}$$

It is important to note here that each term of these operators is proportional to either ϵ or ϵ^\dagger , meaning that bosons will be transformed into fermions and fermions into bosons when acting with them.

Finally we arrive at the point where we can obtain the anticommutators of the supersymmetry generators \hat{Q}, \hat{Q}^\dagger which will make more explicit the connection to the concepts introduced in 2.3.1.

$$\begin{aligned}
\{\hat{Q}_\alpha, \hat{Q}_{\dot{\beta}}^\dagger\} &= 2i\sigma_{\alpha\dot{\beta}}^\mu\partial_\mu = -2\sigma_{\alpha\dot{\beta}}^\mu\hat{P}_\mu, \\
\{\hat{Q}_\alpha, \hat{Q}_\beta\} &= 0, \\
\{\hat{Q}_{\dot{\alpha}}^\dagger, \hat{Q}_{\dot{\beta}}^\dagger\} &= 0.
\end{aligned} \tag{2.126}$$

Chiral covariant derivatives

As is usual in lagrangian constructions we need to find an invariant derivative of the superfield with respect to the new anticommuting coordinates. Obviously the naive choice $\partial/\partial\theta^\alpha$ (or similarly $\partial/\partial\theta_{\dot{\alpha}}^\dagger$) is not valid as is not supersymmetric covariant:

$$\delta_\epsilon\left(\frac{\partial S}{\partial\theta^\alpha}\right) \neq \frac{\partial}{\partial\theta^\alpha}(\delta_\epsilon S). \tag{2.127}$$

Thus in this case we define the chiral covariant derivatives with respect to the anticommuting fields as

$$\begin{aligned}
D_\alpha &:= \frac{\partial}{\partial\theta^\alpha} - i(\sigma^\mu\theta^\dagger)_\alpha\partial_\mu, \\
D^{\dot{\alpha}} &:= -\frac{\partial}{\partial\theta_{\dot{\alpha}}^\dagger} + i(\theta^\dagger\bar{\sigma}^\mu)^{\dot{\alpha}}\partial_\mu.
\end{aligned} \tag{2.128}$$

We also define for Grassman-even fields the antichiral covariant derivative as

$$\bar{D}_{\dot{\alpha}} S^* := (D_{\alpha} S)^*, \quad (2.129)$$

which combined with (2.128) gives

$$\begin{aligned} \bar{D}^{\dot{\alpha}} &:= \frac{\partial}{\partial \theta_{\dot{\alpha}}^{\dagger}} - i(\bar{\sigma}^{\mu} \theta^{\dagger})^{\dot{\alpha}} \partial_{\mu}, \\ \bar{D}_{\dot{\alpha}} &:= -\frac{\partial}{\partial \theta^{\dagger \dot{\alpha}}} + i(\theta \sigma^{\mu})_{\dot{\alpha}} \partial_{\mu}. \end{aligned} \quad (2.130)$$

With this we can now verify that these definitions are indeed supersymmetry covariant by noticing that

$$\{\hat{Q}_{\alpha}, D_{\beta}\} = \{\hat{Q}_{\dot{\alpha}}^{\dagger}, D_{\beta}\} = \{\hat{Q}_{\alpha}, \bar{D}_{\dot{\beta}}\} = \{\hat{Q}_{\dot{\alpha}}^{\dagger}, \bar{D}_{\dot{\beta}}\} = 0, \quad (2.131)$$

so that

$$\delta_{\epsilon}(D_{\alpha} S) = D_{\alpha}(\delta_{\epsilon} S), \quad \delta_{\epsilon}(\bar{D}_{\dot{\alpha}} S) = \bar{D}_{\dot{\alpha}}(\delta_{\epsilon} S). \quad (2.132)$$

Chiral superfields

As previously discussed we need to impose constraints on the superfield S . In the case of a chiral superfield, we impose on a general superfield $\Phi(x, \theta, \theta^{\dagger})$ the constraint

$$\bar{D}_{\dot{\alpha}} \Phi = 0. \quad (2.133)$$

In the case of antichiral superfields we impose similarly the constraint

$$D_{\alpha} \Phi^* = 0. \quad (2.134)$$

To solve this constraints we define an auxiliary field y

$$y^{\mu} := x^{\mu} + i\theta^{\dagger} \bar{\sigma}^{\mu} \theta, \quad (2.135)$$

and rewrite the superfield as a function of the new variable $\Phi(y^{\mu}, \theta^{\alpha}, \theta_{\dot{\alpha}}^{\dagger})$.

The chiral covariant derivatives can be then rewritten as

$$\begin{aligned} D_{\alpha} &:= \frac{\partial}{\partial \theta^{\alpha}} - i(\sigma^{\mu} \theta^{\dagger})_{\alpha} \frac{\partial}{\partial y^{\mu}}, \\ D^{\alpha} &:= -\frac{\partial}{\partial \theta_{\alpha}} + i(\theta^{\dagger} \bar{\sigma}^{\mu})^{\alpha} \frac{\partial}{\partial y^{\mu}}, \\ \bar{D}^{\dot{\alpha}} &= \frac{\partial}{\partial \theta_{\dot{\alpha}}^{\dagger}}, \\ \bar{D}_{\dot{\alpha}} &= -\frac{\partial}{\partial \theta^{\dagger \dot{\alpha}}}. \end{aligned} \quad (2.136)$$

We can see that the constraint is solved by functions of y^{μ}, θ that do not depend on θ^{\dagger} , so we find

$$\Phi = \phi(y) + \sqrt{2}\theta\phi(y) + \theta\theta F(y), \quad (2.137)$$

and for the antichiral case

$$\Phi^* = \phi^*(y^*) + \sqrt{2}\theta^\dagger\phi^\dagger(y^*) + \theta^\dagger\theta^\dagger F^*(y^*), \quad (2.138)$$

where $y^{\mu*} = x^\mu - i\theta^\dagger\bar{\sigma}^\mu\theta$ and where we have used a complex scalar ϕ , a two-component fermion ϕ and an auxiliary field F .

By undoing the variable transformation we can obtain the superfields in the original coordinates

$$\begin{aligned} \Phi &= \phi(x) + i\theta^\dagger\bar{\sigma}^\mu\theta\partial_\mu\phi(x) + \frac{1}{4}\theta\theta\theta^\dagger\theta^\dagger\partial_\mu\partial^\mu\phi(x) \\ &\quad + \sqrt{2}\theta\phi(x) - \frac{i}{\sqrt{2}}\theta\theta\theta^\dagger\bar{\sigma}^\mu\partial_\mu\psi(x) + \theta\theta F(x), \\ \Phi^* &= \phi(x) - i\theta^\dagger\bar{\sigma}^\mu\theta\partial_\mu\phi^*(x) + \frac{1}{4}\theta\theta\theta^\dagger\theta^\dagger\partial_\mu\partial^\mu\phi^*(x) \\ &\quad + \sqrt{2}\theta^\dagger\phi^\dagger(x) - \frac{i}{\sqrt{2}}\theta^\dagger\theta^\dagger\theta\sigma^\mu\partial_\mu\psi(x) + \theta^\dagger\theta^\dagger F^*(x). \end{aligned} \quad (2.139)$$

By comparison this with the general superfield (2.119) we can easily obtain the supersymmetry transformations

$$\begin{aligned} \delta_\epsilon\phi &= \epsilon\psi, \\ \delta_\epsilon\psi_\alpha &= -i(\sigma^\mu\epsilon^\dagger)_\alpha\partial_\mu\phi + \epsilon_\alpha F, \\ \delta_\epsilon F &= -i\epsilon^\dagger\bar{\sigma}^\mu\partial_\mu\psi. \end{aligned} \quad (2.140)$$

It is possible to construct a chiral (or antichiral) superfield from a general superfield S by using

$$\begin{aligned} \Phi &\equiv \overline{DD}S \equiv \bar{D}_{\dot{\alpha}}\bar{D}^{\dot{\alpha}}S, \\ \Phi^* &\equiv DDS^* \equiv D^\alpha D_\alpha S^*. \end{aligned} \quad (2.141)$$

In fact, given a chiral superfield Φ it is always possible to find a superfield S for such construction. Also it can also be used that $W(\Phi_i)$ is a superchiral field for an arbitrary holomorphic function W and superchiral fields Phi_i .

Vector superfields

A vector superfield can be obtained by imposing the constraint reality $V = V^*$, which is equivalent to imposing

$$a = a^*, \quad \chi^\dagger = \xi^\dagger, \quad c = b^*, \quad \nu_\mu = \nu_\mu^*, \quad \zeta^\dagger = \eta^\dagger, \quad d = d^*. \quad (2.142)$$

It is customary to define in this case

$$\eta_\alpha = \lambda_\alpha - \frac{i}{2}(\sigma^\mu\partial_\mu\chi^\dagger)_\alpha, \quad \nu_\mu = A_\mu, \quad d = \frac{1}{2}D + \frac{1}{4}\partial_m u\partial^\mu a, \quad (2.143)$$

so we can write the superfield expanded as

$$V(x, \theta \theta^\dagger) = a + \theta \xi + \theta \theta b + \theta^\dagger \theta^\dagger b^* + \theta^\dagger \bar{\sigma}^\mu \theta A_\mu + \theta^\dagger \theta^\dagger \theta (\lambda - \frac{i}{2} \sigma^\mu \partial_m u \xi^\dagger) + \theta \theta \theta^\dagger (\lambda^\dagger - \frac{i}{2} \bar{\sigma}_\mu \xi) + \theta \theta \theta^\dagger \theta^\dagger (\frac{1}{2} D + \frac{1}{4} \partial_\mu \partial^\mu a). \quad (2.144)$$

The transformations can be obtained similarly as for the chiral case from $\sqrt{2} \delta_\epsilon V = -i(\epsilon \hat{Q} + \epsilon^\dagger \hat{Q}^\dagger) V$ and can be found e.g. in [23].

At this point we note that if Φ is a chiral field, then $\Phi + \Phi^*$, $i(\Phi - \Phi^*)$ and $\Phi \Phi^*$ are all vector fields. If the vector superfield represents a supermultiplet it will contain gauge bosons, gauginos, and gauge auxiliary fields A^μ, λ, D . The other components a, ξ, b mass dimensions 0, 1/2, 1 are auxiliary fields that are gauged away.

Supersymmetric lagrangians

Using the components we have presented we now turn to the issue of how to build a lagrangian using superfields. The first component is to realize that the integral of any superfield over the whole superspace is invariant $\delta_\epsilon A = 0$ with

$$A = \int d^4 x \int d^2 \theta d^2 \theta^\dagger S(x, \theta, \theta^\dagger), \quad (2.145)$$

since $\hat{Q}^{(\dagger)}$ are defined as sums of total derivatives with respect to the superspace coordinates. This gives the form of the dynamic contributions to the action where the vector S must be superfield a vector superfield V to preserve the reality of the action. To obtain the lagrangian density \mathcal{L} we integrate over the fermionic coordinates

$$V_D = \int d^2 \theta d^2 \theta^\dagger V(x, \theta, \theta^\dagger) = V(x, \theta, \theta^\dagger) \Big|_{\theta \theta^\dagger \theta^\dagger} = \frac{1}{2} D + \frac{1}{4} \partial_\mu \partial^\mu a, \quad (2.146)$$

where we note that the $\partial_\mu \partial^\mu a$ term will disappear after integration over $\int d^4$. This is the so-called D -term contribution to the lagrangian density.

The other type of contribution can be obtained from the fact that the F -term of a chiral superfield is also a total derivative under a supersymmetry transformation, so one can introduce contributions of the form

$$\Phi_F = \Phi|_{\theta\theta} = \int d^2 \theta \Phi \Big|_{\theta^\dagger=0} = \int d\theta d^2 \theta^\dagger \delta^{(2)}(\theta^\dagger) \Phi = F. \quad (2.147)$$

Since the F -term in general can be complex, it is necessary to add as usual $\Phi_F + \text{c.c.}$ terms to the lagrangian.

In general we can form a complete lagrangian then as

$$\mathcal{L} = [\Phi^{*i} \Phi_i]_D + ([W(\Phi_i)]_F + \text{c.c.}) \quad (2.148)$$

where W can be any holomorphic function of the chiral superfields.

Name	Families	Symbol	Spin 0	Spin 1/2	SU(3) \times SU(2) \times U(1)
Quarks	3	Q	$(\tilde{u}_L, \tilde{d}_L)$	(u_L, d_L)	$(\mathbf{3}, \mathbf{2}, 1/6)$
& squarks	3	$\bar{u},$	\tilde{u}_R^*	U_R^\dagger	$(\bar{\mathbf{3}}, \mathbf{1}, -2/3)$
	3	\bar{d}	\tilde{d}_R^*	d_R^\dagger	$(\bar{\mathbf{3}}, \mathbf{1}, 1/3)$
Leptons	3	L	$(\tilde{\nu}, \tilde{e}_L)$	(ν, e_L)	$(\mathbf{1}, \mathbf{2}, -1/2)$
& sleptons	3	\bar{e}	\tilde{e}_R^*	e_R^\dagger	$(\mathbf{1}, \mathbf{1}, 1)$
Higgs	1	H_u	(H_u^+, H_u^0)	$(\tilde{H}_u^+, \tilde{H}_u^0)$	$(\mathbf{1}, \mathbf{2}, 1/2)$
& higgsinos	1	H_d	(H_d^0, H_d^-)	$(\tilde{H}_d^0, \tilde{H}_d^-)$	$(\mathbf{1}, \mathbf{2}, -1/2)$

Table 2.1: Particle content of the Minimal Supersymmetric Standard Model.

2.3.3 The Minimal Supersymmetric Standard Model

In this section we will introduce a minimal extension of the Standard Model that includes Supersymmetry, the Minimal Supersymmetric Standard Model (MSSM). We will begin introducing its particle content and construct its lagrangian using the results of the previous section. We will then introduce the soft symmetry breaking in the MSSM. In particular we will focus on the neutralinos and charginos sector of the MSSM as it is the relevant one in this thesis.

Particle content and lagrangian

The particle content of the MSSM is the one in Tab. 2.1. Using the developments of the previous section, the superpotential of the MSSM can be found to be

$$W_{\text{MSSM}} = \bar{u} \mathbf{y}_u Q H_u - \bar{d} \mathbf{y}_d Q H_d - \bar{e} \mathbf{y}_e L H_d + \mu H_u H_d, \quad (2.149)$$

where $H_{u,d}, Q, L, \bar{u}, \bar{d}, \bar{e}$ are the chiral superfields of the supermultiplets in Tab. 2.1 and the $\mathbf{y}_{u,d,e}$ are the Yukawa matrices of each family. The last μ term is the supersymmetric equivalent of the Higgs boson mass terms in the SM lagrangian. We can note here that terms of the form $H^* H$ are not holomorphic in the chiral superfields and therefore do not appear in the lagrangian. Also interesting to note here is that we can see from this that both H_u and H_d are necessary to give mass through the Yukawa terms to quarks and leptons: Terms like $\bar{u} Q H_d^*$ are not holomorphic and therefore we need the $\bar{Q} H_u$ term (and following a similar argument for H_d), apart from anomaly cancellation arguments.

R-parity

The superpotential (2.149) does not contain all renormalizable gauge-invariant terms holomorphic in the chiral superfields. In particular by omitting certain terms we have implicitly adopted certain extra symmetries, namely the

baryon number B and lepton number L conservation. Those extra terms can be written as the following, where we have excluded family indices:

$$W_{\Delta L=1} = \frac{1}{2}\lambda LL\bar{e}_k + \lambda' LQ\bar{d}_k + \mu' LH \quad (2.150)$$

$$W_{\Delta B=1} = \frac{1}{2}\lambda''\bar{u}d\bar{d}. \quad (2.151)$$

Chiral supermultiplets have $B = 1/3$ in the case of Q and $B = -1/3$ for \bar{u}, \bar{d} , whereas L has $L = 1$ and \bar{e} has leptonic charge $L = -1$. All others assignments are either $B = 0$ or $L = 0$. With this it is easy to see then that (2.150) violates lepton number by one unit whereas (2.151) violates baryonic number also by one unit. This leads to an obvious issue since B - and L -violating processes are heavily constrained experimentally. In particular, one of the first and most obvious constraints is the one coming from the non-decay of the proton. For example, if we were to allow such processes, a simple diagram from $p^+ \rightarrow e^+\pi^0$ or similar processes would give approximately

$$\Gamma_{p \rightarrow e^+\pi^0} \sim m_p^5 \sum_{2,3} \|\lambda'_{1i}\lambda''_{1i}\|^2 / m_{\bar{d}_i}^4, \quad (2.152)$$

which for couplings ~ 1 and sparticle masses of ~ 1 TeV would mean a decay time of less than a second, whereas experimental bounds are well above 10^{32} years.

The gaugino sector

The quantum gauge eigenstates for higgsinos and gauginos mix with each other giving rise to mass eigenstates. The neutral higgsinos and gauginos combine to four neutralinos χ^0 , and the charged higgsinos and winos combine into two charginos χ^\pm .

We will start analyzing the neutral sector. The MSSM lagrangian has a term of the form

$$\mathcal{L} \supset -\frac{1}{2}\Phi^T \mathbf{M}_0 \Phi + \text{c.c.} \quad (2.153)$$

where Φ is the gauge-eigenstate basis $\Phi = (\tilde{B}, \tilde{W}^0, \tilde{H}_d^0, \tilde{H}_u^0)$ and the mixing matrix $\mathbf{M}_{\tilde{\chi}}$ can be written from the MSSM lagrangian as

$$\mathbf{M}_0 = \begin{pmatrix} M_1 & 0 & -c_\beta s_W m_Z & s_\beta s_W m_Z \\ 0 & M_2 & c_\beta c_W m_Z & -s_\beta c_W m_Z \\ -c_\beta s_W m_Z & c_\beta c_W m_Z & 0 & -\mu \\ s_\beta s_W m_Z & -s_\beta c_W m_Z & -\mu & 0 \end{pmatrix}, \quad (2.154)$$

where we have used the VEVs for the Higgs scalars, and use the usual notation $s_\beta = \sin \beta$, $c_\beta = \cos \beta$, $s_W = \sin \theta_W$ and $c_W = \cos \theta_W$. This mixing matrix can be diagonalized by a unitary matrix \mathbf{N} such that

$$N^* \mathbf{M}_0 N^{-1} = \text{diag}(m_{\chi_1}^0, m_{\chi_2}^0, m_{\chi_3}^0, m_{\chi_4}^0). \quad (2.155)$$

The parameters M_1, M_2, μ are in general complex but a phase redefinition of \tilde{B}, \tilde{W} allows us to choose M_1, M_2 real and positive. The parameter μ still remains complex as there are no further degrees of freedom to rotate. However a nonreal μ can have CP-violating consequences unless nontrivial cancellations apply, and therefore it is usually chosen real, although with arbitrary sign.

We now review the charged sector, which is very similar to the neutral case. The lagrangian term in this case is given by

$$\mathcal{L} \supset -\frac{1}{2}(\Psi)^T \mathbf{M}_\pm \Psi + \text{c.c.} \quad (2.156)$$

with $\Psi = (\tilde{W}^+, \tilde{H}_u^+, \tilde{W}^-, \tilde{H}_d^-)$ and the mixing matrix is given in this case by

$$\mathbf{M}_\pm = \begin{pmatrix} \mathbf{0} & \mathbf{X}^T \\ \mathbf{X} & \mathbf{0} \end{pmatrix} \quad (2.157)$$

with

$$\mathbf{X} := \begin{pmatrix} M_2 & \sqrt{2}s_\beta m_W \\ \sqrt{2}c_\beta m_W & \mu \end{pmatrix} \quad (2.158)$$

with the same conventions as in the neutralino case.

The mass eigenstates are then given by 2×2 unitary matrices \mathbf{U} and \mathbf{V} for the negatively and positively charged particles, respectively. They are chosen so that

$$\mathbf{U}^* \mathbf{X} \mathbf{V}^{-1} = \text{diag}(m_{\tilde{\chi}_1^\pm}, m_{\tilde{\chi}_2^\pm}) \quad (2.159)$$

All the corresponding Feynman rules can be found in [26].

Chapter 3

Resummino

Resummino a software package to compute resummation predictions for particle production in beyond the standard model theories at hadron colliders. The different parts of the software have been developed over time for prediction in different theoretical frameworks. In this chapter we will present the software package in its current form. We will first briefly review the context of resummation software in , then present in somewhat more detail the software package structure of Resummino in , briefly considering its evolution, later in we will present detailed instructions for building and installing Resummino (including its software dependencies), and finally in we will present usage instructions and show examples of running the software.

3.1 Software implementations of resummation

As we have developed in Ch. 3, resummation predictions require a relatively complex and specific mathematical framework, in general distinct from the other usual fixed-order or parton showering approaches like Pythia at LO or MadGraph at NLO [27]. This requires specific software programs with the required mathematical components to perform the resummation corrections. Resummation computations has been long been successfully for Standard Model processes [8]. An example of resummation software relevant for standard model cross sections are the different variants of ResBos that include Z and W production [28, 29, 30], Higgs production [31, 32] and low-mass Drell-Yann [28, 29].

As currently the ATLAS and CMS experiments at LHC search for new physics, BSM resummation predictions have become necessary to constrain larger regions of the vast parameter spaces. In particular, for SUSY resummation, strong production channels have precise resummed cross sections as implemented by the software package NNLL-fast [33], which provides NNLL corrections matched to approximated NNLO for SUSY colored particles, both for squarks and gluinos [34] and stop and sbottom production

[35]. In the case of this program, the NLO results are obtained separately by the software package Prospino [36, 37, 38].

Resummino [39] has been developed to provide precise resummation predictions for several Beyond the Standard Model particle production processes, including supersymmetric [40, 41, 42, 43, 44, 45, 46, 39, 47, 48, 12, 10, 49] and non-supersymmetric Z', W' production [50, 51]. The implementation of resummation in software requires certain different components that will be analyzed in this chapter.

3.2 Code architecture and structure

In this section we will present the current code structure, with the different components and how they relate to each other, including the dependency of internal as well as external codes of the different modules. We will briefly compare the current form with previous versions of the code.

3.2.1 Build system

Software written in compiled languages like C++ require a compiler to transform the code into running binaries and a linker to link those binaries to external dependencies in the system, e.g. shared libraries.

Although a manual compilation of the code is possible, automated build systems are required for packages of this complexity, so as to avoid having to manually find and reference external dependencies and define the compilation process. Also this provides more resilience to changes in the system paths and makes it easier to build on heterogeneous systems, e.g. in the case of Resummino on Linux or OS X systems.

Traditionally the compilation process was defined using hand-written Makefiles. Initial versions of the software used this approach, where it was necessary to manually modify a Makefile to compile the software in a given system. This included referencing the different software components as well as the relevant compilers, including system paths. This approach is not sustainable as it inevitably has assumptions about which particular system or compiler (and compiler version) is going to be used, and has in the past caused issues where compilation of the system was difficult and error-prone. Modern Resummino uses the CMake build system for compilation. Through a series of files in the code this defines the necessary dependencies and the build process in a system-agnostic way, and the CMake software automatically adapts the generation of appropriate Makefiles adapted to the target system. When compiling Resummino, the CMake software will (1) find if the required compiler, libraries and dependencies are present in the system, and what varieties and versions of them to use; (2) if that is the case, where in the system they can be found, and (3) uses that information together with

the build description of the package to generate the crafted Makefiles that can be used to build Resummino and link it to the external dependencies.

The main CMake file is called `CMakeLists.txt` and is located at the root of the code tree. This file defines the project, loads the rest of the modules, and initiates the build process.

Some of the modules are located in the `cmake` folder. These are small pieces of CMake code that locate some of the dependencies. In particular included are modules to locate the right version of `GSL`, `LHAPDF` and `LoopTools` as well as some required `Boost` libraries. These models will handle the appropriate linking. In 3.3.3 we will see how to indicate to the modules where the external libraries are located, if they are not in standard paths.

Finally the compilation of the main Resummino code is done in the file `src/CMakeLists.txt`, where the source code files are listed and the instructions for the creation of the Resummino library are located.

3.2.2 Included external dependencies

Resummino depends on several packages that can be found or at least easily installed on modern systems (see 3.3), and in those cases it has been preferred to use the external link. This allows to leverage the upstream updates for those packages including bug fixes. But it also depends on other packages that are more difficult to find in binary form or that present more issues for compilation. In this case, the decision has been to include these packages into the Resummino code itself and compile it together with the main code. This happens mostly transparently for the user.

In particular Resummino has a version with the package `LoopTools` [52] included with the source code (although the user can choose to use a version without it and provide its own linked version). Also, the `SLHAea` library (in the form of a stand-alone header) is included for convenience.

These packages can be found in the `lib` folder of the source tree (or in `include` in the case of header-only libraries).

3.2.3 Code structure

The Resummino code itself is structured over different files inside the `src` folder of the source tree. As is typical in C++ packages, the code is distributed into modules with separate header (`.h` files) and source code (`.cc` files). In previous versions of the software, the files were spread into several directories (including e.g. some kinematical code in an `inc` folder together with vendored code and some PDF inside a `tmp` folder). These extraneous directories have been removed and their contents reorganized. Also the contents of the different files have been reorganized into different files, which have been renamed for clarity. Overall we intent to have a set of properly-named files that make the structure of the code more obvious. We will

briefly review this structure of files, their content and organization, as well as their mutual relationships.

We can differentiate two different blocks inside the code. The first one is focused on the mathematical computations, and the second one responsible for the user interaction. Resummino is comprised of the following modules and the corresponding files:

- Matrix elements: `matrix_*.cc` files
- Partonic cross sections: `pxs_*.cc` and `pxs.h` files
- Kinematics module: `kinematics.{cc,h}` files
- Dipoles module: `dipoles.{cc,h}`
- Integration module: `integration_method.{cc,h}` files
- Hadronic cross section module: `hxs.cc`, `hxs_dlnm2.cc`, `hxs_dpt2.cc` files for total cross sections, invariant mass distribution, and transverse momentum distribution respectively, as well as `hxs.h` as common module header.
- Resummation module: `resummation.{cc,h}` files
- PDF module: `pdf.{cc,h}` files
- Mathematics utilities: The files `maths.{cc,h}` for the general purpose mathematical functions, as well as `npf.h` for n -point functions
- General utilities: `utils.h` files
- User interface: `main.cc` file
- User parameters handling: `params.{cc,h}` files

The *matrix elements* block contains the functions that evaluate the matrix elements of the different diagrams contributing to the different orders of the fixed-order computation. The different files contain the matrix elements grouped by type, and the naming should be obvious. This includes `born` for the tree-level order, the ones ending in `real` which contain the real contributions and the `box`, `bubble` and `triangle` which contain the corresponding type of the loop diagrams, plus the `counterterm` file for the counterterms. The different conventions with respect to the naming of the different variables and the name of the naming of the functions themselves are documented in the header of every file, for example `pa` (`pb`) represents the momentum of the first (second) incoming particle, similarly for `p1`, `p2` for the outgoing particles, and `MBss()` is the function which computes the matrix element squared M for the tree-level contribution (B) of the s -channel

when squared with itself `ss`. The reader is referred to the code for other cases.

The *partonic cross sections* module uses the *matrix elements* block to obtain the partonic cross section. In particular it sets the appropriate propagators, couplings, and sums over the all the relevant matrix elements. For debugging purposes channels can be temporarily enabled and disabled in this module. The relevant file in the case of gauginos is `pxs_gauginos.cc` and similarly for the other processes implemented.

The *kinematics* module contains several useful kinematical transformations that are used by the *partonic cross sections* block to set the appropriate values when evaluating the matrix elements (for example expressing the dot products of the form $p_i \cdot p_j$ in terms of the Maldestam variable s, t, u).

The *dipoles* module contains all the relevant code for the Catani-Seymour dipoles [53, 54] and the Altarelli-Parisi splitting functions.

The *integration* module performs the final integration of the partonic cross sections together with the kinematical factors to obtain the hadronic cross sections. This module makes heavy use of the GNU Scientific Library [55] to perform the Vegas integration [56]. The integration algorithm and most important parameters are programmed in this module and are very relevant for the correct functioning of the software.

The *hadronic cross section* module uses the *integration* module to perform the integration. The integration is thus split into two different blocks with different responsibilities: In this module only the physical parameters and processes are defined, whereas the *integration* block defines all technical parameters and algorithm choices related to the technical process of integration. In particular this module uses the previously obtained partonic cross section integrand together with the kinematical variables to build the integrand with the phase space, define the relevant integration variables and its limits as well as any further factors (e.g. conversion factors to obtain the expected physical units). This integration can be done for the total cross section (`hxs.cc`), or for transverse momentum (`hxs_dpt2.cc`) or invariant mass (`hxs_d1m2.cc`).

The *resummation* module implements as expected the functions related to the resummation procedure as in 2.2 to obtain the unintegrated hadronic cross that can be integrated by the previous modules.

The PDF module is a crucial piece of the resummation computation. It not only wraps the usual PDF-related functions that allow Resummino to use the different PDF sets, it also handles the transformation of the PDF into Mellin space through a fit of the chosen PDF which is then transformed mathematically.

The *mathematical* and *general* utilities modules contain convenient definitions that are used in the rest of the package, for example defining special functions like the Γ function or defining the PDG particle codes to handle user input.

The *parameters* module holds all relevant physical parameter for a given process. These include the process parameters (e.g. energy or type of collider) as well as the physical model including particle masses, the SUSY benchmark point through the use of the SLHA convention as well as relevant couplings. This module also handles the reading of the parameters in the different input files read by the software.

Finally the *user interface* implements the command-line interface that is used by the user to interact with the software. This includes reading interpreting the user input, running the corresponding calculations by using the other modules, and creating the output in the different formats for the user, as well handling any errors in the user input or in any of the rest of the modules.

3.3 Software requirements and installation

The software Resummino requires several external software packages to be compiled (compile-time dependencies) and ran (run-time dependencies). Here we will briefly review the different external codes used and their function inside the Resummino codebase. After that we will review how to make sure these dependencies are properly installed in the system and how to build the software using the CMake software as seen in 3.2.1. These dependencies have significantly changed from previous versions of the code, since loop integrals as well as PDF handling used different libraries which did not allow for the flexibility of these new options.

3.3.1 Explanation of dependencies

The Resummino code makes use of the following packages that we will briefly describe:

- LoopTools
- CMake
- Boost headers
- GNU Scientific Library
- LHAPDF
- SLHAea

The LoopTools package is a run-time dependency (although it can be optionally included with the codebase as seen in 3.2.2) to numerically perform loop integrals.

The CMake binaries are a compile-time dependency necessary to compile the software as explained in 3.2.1. As a compile-time dependency once the Resummino binary has been built it is not needed anymore (and in particular it does not have to be installed in the system running the code in production).

The Boost headers are a compile-time dependency that includes a vast array of practical C++ functions. They are widely used in the C++ community, and in the case of Resummino they are used for their string parsing support used in the input section of the user interface.

The GNU Scientific Library is a run-time dependency used for numerical computations inside Resummino [57]. In particular several parts of this library are used for different mathematical operations, including multi-dimensional Monte Carlo Vegas integration in the phase space, numerical fits of the PDFs used for the necessary transformations in the resummation procedure, special functions (in particular dilog and ζ functions), and different optimized vector and matrix operations.

The LHAPDF library [58] is a run-time dependency that implements a interpolator used for evaluating PDF grids, as well as a collection of those grids in an standardized format. LHAPDF is the way Resummino reads external PDFs, and therefore any PDF set implemented in such framework can be used in Resummino (previous versions did not use LHAPDF and were limited to some PDF families).

The SLHAea is a header-only library used to parse SLHA input files that is included together with the Resummino code for convenience.

3.3.2 Installation of dependencies

Before proceeding to the installation it is necessary to make sure that all dependencies are installed in the system.

In the case of LHAPDF this is very simple, and following the public instructions this can be done by downloading the appropriate tarball and decompressing it and entering into the created directory

```
$ tar xf LHAPDF-<version>.tar.gz
$ cd LHAPDF-<version>
```

where <version> is the version of LHAPDF to use, and once in the directory compiling with the usual UNIX verbs

```
$ ./configure
$ make
$ make install
```

If the user does not have enough rights, `sudo` may be needed in the last step (or the user can choose an alternative installation path, see the LoopTools

documentation for details). Please note that LHAPDF, as well as Resummino itself, require the Boost packages (which can be installed by using the standard system package tools).

LoopTools is installed in a very similar way in case the user wants to use their own LoopTools package.

3.3.3 Compilation

Resummino is distributed in tarballs named `resummino-<version>.tar.bz2` or similarly, therefore the first step in the compilation process is to extract the contents of the files:

```
$ tar -xvf resummino-<version>.tar.bz2
```

Once extracted, we enter the newly created folder where we can find the Resummino code:

```
$ cd resummino-<version>
```

It is recommended to build the code out-of-source, which avoid polluting the source tree with binary files and allows for independent build, for which we will create a new empty folder where to put the binaries and enter it:

```
$ mkdir build
$ cd build
```

Now we can run the CMake binary that will look for all the dependencies and prepare all the Makefiles ready for compilation in the target system:

```
$ cmake ../ -DLHAPDF=/usr/local/lhapdf \
-DCMAKE_INSTALL_PREFIX=/usr/local/resummino
```

Many compilation options can be given in this step. We will briefly review the most relevant ones here for convenience.

Finally we can compile the main Resummino binaries with:

```
$ make
```

If needed we can also install the software (to the target path given above), for which we can issue:

```
$ make install
```

It is important to note that if the target path is a system-wide folder (which is the default) we will require root privileges for this step, and therefore we will need to do something similar to:

```
$ sudo make install
```

provided we have `sudo` rights on the machine.

3.4 Software usage

The different input parameters that define the process and the type of computation to perform are passed to Resummino using an input file. Earlier versions of the code did not have the concept of input file and instead relied on execution scripts that defined the input parameters as variables. This is cumbersome and error-prone and therefore the decision was made to move the software to a simple input file format. An example input file is found in the code as `input/resummino.in`. This file contains the main definitions of the process to perform (type of collider, energy, etc.). The SUSY model has to be specified in a separate input file following the standard SLHA format [59, 60]. An example SLHA file can be found in the release source code as `input/slha.in`. The particular SLHA file to use is specified in the Resummino input file using the `slha` parameter. Please note that the path to the SLHA file must be specified relative to the Resummino input file, so in this case the variable will be `slha = slha.in`.

3.4.1 Input file

The different blocks that need to be configured in the Resummino input file are:

- Collider type and energy
- Physical process
- Type of computation to perform
- SUSY model
- Parton Distribution Function (PDF)
- QCD scales
- Integration parameters

The first block that should be configured in the input file is the type and energy of the collider, which is done with the following variables:

```
collider_type = proton-proton
center_of_mass_energy = 13000
```

The `center_of_mass_energy` parameter is in GeV. Also possible for the collider type is `proton-antiproton`.

After that it is necessary to define the physical process for which to compute the cross sections. This is done by specifying the two outgoing particles:

Particle type	Particle	PDG code
Slepton	\tilde{e}_L^-	1000011
Slepton	\tilde{e}_R^-	2000011
Slepton	$\tilde{\nu}_{eL}$	1000012
Slepton	$\tilde{\mu}_L^-$	1000013
Slepton	$\tilde{\mu}_R^-$	2000013
Slepton	$\tilde{\nu}_{\mu L}$	1000014
Slepton	$\tilde{\tau}_1^-$	1000015
Slepton	$\tilde{\tau}_2^-$	2000015
Slepton	$\tilde{\nu}_\tau$	1000016
Gaugino	$\tilde{\chi}_1^0$	1000022
Gaugino	$\tilde{\chi}_2^0$	1000023
Gaugino	$\tilde{\chi}_3^0$	1000025
Gaugino	$\tilde{\chi}_4^0$	1000035
Gaugino	$\tilde{\chi}_1^+$	1000024
Gaugino	$\tilde{\chi}_2^+$	1000037

Table 3.1: PDG number codes for the different supersymmetric particles understood by Resummino.

```
particle1 = 1000011
particle2 = -1000011
```

This parameters follow the PDG numbering scheme , and in particular a minus sign implies the corresponding antiparticle.

For reference we list here the particle codes understood by Resummino in Fig. 3.1.

It is also necessary to specify the type of computation to perform. This can be a total cross section, transverse momentum cross section, transverse momentum cross section using the joint resummation formalism, or the invariant mass cross section:

```
result = total
M = auto
pt = auto
```

For the result variables the possible values are `total`, `pt`, `ptj`, or `m`, corresponding to the possibilities above. The variable `M` contains the invariant mass scale of the process. For total cross sections or transverse momentum ones, this should be left as `auto` and it will be assigned to $\sqrt{(p_1 + p_2)^2}$. For invariant mass distribution computations, this should be set at the invariant mass point to compute. Similarly with the `pt` variable for transverse momentum distributions (whether or not in the joint formalism).

The SUSY model used for the computations must be defined in an external file in the standard SLHA format [59, 60]. That file must be referenced

in the Resummino input file using the variable:

```
slha = slha.in
```

where the file `slha.in` is the SLHA file to use. In case of using a relative path it must be relative to the Resummino input file.

For the Parton Distribution Function Resummino uses the standard LHAPDF library which contains a large number of different PDF families in common standard formats. In Resummino the PDF options are controlled by the variables:

```
pdf_format = lhgrid # lhgrid or lhpdf
pdf_lo = CT14llo
pdfset_lo = 0
pdf_nlo = CT14nlo
pdfset_nlo = 0
```

In this case, the `pdf_format` variable can take the values `lhgrid` or `lhpdf` depending on the format of the LHAPDF files used. After that we define the Leading Order (LO) and the Next-to-Leading Order (NLO) PDFs by specifying the family name and the set inside the family. (Normally sets are used for uncertainty computations. Typically it will be necessary to run all the sets inside a given family.)

Finally Resummino offers the user some low-level integration parameters:

```
precision = 0.01
max_iters = 5
```

where `precision` is the desired numerical uncertainty precision in the integration and `max_iters` is the maximum number of integration iterations. These parameters are passed to the GSL integration functions. The default values work for a large array of situations.

3.4.2 Running Resummino

Once compiled the Resummino binaries can be ran by issuing on the terminal:

```
$ resummino <input_file>
```

where `<input_file>` is the path to the the input file as described above.

A typical use-case while running Resummino is to compute a set of cross sections with similar but not exactly the same process parameters. For example, when computing invariant-mass or transverse momentum distributions, or scanning a mass parameter space. In that case, it would be impractical to have a huge set of similar input files. The solution is then to override one or a few input file parameters using command-line options. In

those cases, instead of having one input file per PDF subset, you can just use a common input file and use the `pdfset_lo` and `pdfset_nlo` command-line options to override the PDF subsets.

If a command-line option is specified, the value from the input file is ignored. Possible values for the command line arguments are the following:

- `particle1` and `particle2`: Replace `particle1` and `particle2` respectively
- `invariantmass` or `m`: Replaces `m`
- `transversemomentum` or `t`: Replaces `pt`
- `pdfset_lo` and `pdfset_nlo`: Replace `pdf_lo` and `pdf_nlo` respectively
- `mu_f` and `mu_r`: Replace `mu_f` and `mu_r` respectively
- `output_file` or `o`: Make Resummino create an output file with the output in a machine-readable format for further analysis (see 3.4.3); this option does not have an input-file equivalent

Resummino also offers the possibility of only running up to a certain fixed level of precision (LO or NLO), useful for debugging and for comparing with other tools. In those cases no resummation is performed and the fixed-order results are outputted. Some values which are not calculated will be set numerically to 0.

Resummino also understand the special syntax for input file - which will be interpreted as `stdin` making it useful for passing the input file on-the-fly e.g. through UNIX pipes, which allows for more advanced use cases.

3.4.3 Resummino output

Each time Resummino is called, it produces as output three cross sections (the cross section for the specified process at LO, NLO and NLO matched with NLL). This can be either a total cross section for the process or a point in a transverse momentum or invariant mass differential distribution. These numbers (including the appropriate units) will be printed to `stdout` in a human-readable form.

Optionally it can also create an output file in a machine-readable format for further analysis. In particular Resummino can output the results to a JSON format, which is a standard format available in a variety of languages and analysis tools.

However, usually a subsequent analysis of this data is required to, e.g., determine the uncertainties, or to obtain a distribution plot, which is simplified by a computer-friendly output format. While there are established standards for the input to Resummino (SLHA and LHAPDF), there is so far no clearly defined way to output cross sections in a standardized way.

The decision has been to include an option to output the results to a JSON file. This is a well-known and established format with implementations in virtually every programming language. To obtain the JSON output, you have to specify the `output_file` command-line argument as shown in 3.4.2.

The Resummino JSON output is a dictionary containing the following variables:

```
{
  "key": "",
  "pt": -1,
  "m": -1,
  "pdflo": "MSTW2008lo68cl",
  "pdfsetlo": 0,
  "pdfnlo": "MSTW2008nlo68cl",
  "pdfsetnlo": 0,
  "muf": 0.5,
  "mur": 0.5,
  "lo": 2.8873845e-03,
  "nlo": 0.0000000e+00,
  "n1l": 0.0000000e+00,
  "n1lj": 0.0000000e+00,
  "units": "pb"
}
```

3.5 Examples

For reference purposes we will include in this section some example cross sections for processes implemented in the Resummino code [39]. We chose to implement this examples in the benchmark point 31 of [61]. In this scenario $\tan\beta = 40$, $\mu > 0$, $A_0 = -500$ GeV and the SUSY-breaking-scale masses are set at $m_0 = 400$ GeV and $m_{1/2} = 600$ GeV. After renormalization group equations almost all squark and gluino masses are ~ 1.5 TeV and electroweak particles have masses ~ 250 – 850 GeV. These computations were originally done for the 8 TeV LHC run and use MSTW 2008 PDF sets [4]. We perform scale variation by multiplying the central scale which is set to the average mass of the outgoing particles by factors $1/2, 2$. We produce two sets of cross sections: In Tab. 3.2 we show results for gauginos and in Tab. 3.3 we show cross sections for another process implemented in Resummino as an example of a non-gaugino process implemented in the same software framework.

Pair	LO (fb)	NLO (fb)	NLO+NLL (fb)
$\tilde{\chi}_1^0 \tilde{\chi}_1^0$	$0.1245^{+8.6\%}_{-7.5\%}$	$0.1605^{+3.6\%}_{-3.6\%}$	$0.1554^{+0.2\%}_{-0.0\%}$
$\tilde{\chi}_2^0 \tilde{\chi}_2^0$	$0.0875^{+12\%}_{-10\%}$	$0.1065^{+4.5\%}_{-3.7\%}$	$0.1043^{+0.3\%}_{-0.0\%}$
$\tilde{\chi}_1^+ \tilde{\chi}_2^0$	$4.3674^{+9.9\%}_{-8.5\%}$	$4.8750^{+2.0\%}_{-2.4\%}$	$4.8248^{+0.3\%}_{-0.5\%}$
$\tilde{\chi}_1^- \tilde{\chi}_2^0$	$1.4986^{+10\%}_{-8.6\%}$	$1.7333^{+2.1\%}_{-2.4\%}$	$1.7111^{+0.6\%}_{-1.1\%}$
$\tilde{\chi}_1^+ \tilde{\chi}_1^-$	$2.8874^{+9.9\%}_{-8.5\%}$	$3.3463^{+3.3\%}_{-3.3\%}$	$3.3086^{+0.7\%}_{-0.3\%}$

Table 3.2: Example total cross section for different gaugino pair production at LO, NLO and NLO+NLL for benchmark point 31.

Pair	LO (fb)	NLO (fb)	NLO+NLL (fb)
$\tilde{\ell}_R^+ \tilde{\ell}_R^-$	$0.0749^{+11\%}_{-9.1\%}$	$0.0868^{+2.7\%}_{-3.0\%}$	$0.0854^{+0.2\%}_{-0.4\%}$
$\tilde{\ell}_L^+ \tilde{\ell}_L^-$	$0.0477^{+12\%}_{-10\%}$	$0.0543^{+2.8\%}_{-3.4\%}$	$0.0534^{+0.5\%}_{-0.3\%}$
$\tilde{\tau}_1^+ \tilde{\tau}_1^-$	$0.5878^{+7.6\%}_{-5.3\%}$	$0.7093^{+2.5\%}_{-2.5\%}$	$0.6985^{+0.0\%}_{-0.2\%}$

Table 3.3: Same as for 3.2 but for sleptons, as an example of non-gaugino process implemented in the same reference code.

Chapter 4

Gauginos production

In this chapter we will present the results of resummed computations for gaugino production at the LHC by using the software Resummino presented in previous chapters. The results presented in this chapter were published in [39, 47] and will follow the outlines of those. In 4.1 we will contextualize the results and present the current searches and constraints, in 4.2 we will introduce the different benchmark points that will be used for the different computations, and the results of those will be presented in 4.3 for total cross sections and in 4.4 for the invariant-mass and transverse-momentum distributions.

4.1 Current experimental searches and constraints

We will now review the current state of searches at hadron colliders for the different gauginos, as well as the current limits on the masses and parameter space. The most current limits can be found in [4] and updates. We will first briefly remember the most relevant parameters when considering the gaugino sector, and then analyze the main production channels for charginos and neutralinos, and revise the most recent constraints coming from the different hadron collider experiments, with a focus on the current LHC limits.

As we have seen, the gaugino states mix together with the higgsinos to produce the physical charginos (composed of the charged wino and higgsino states) and neutralinos (composed of the neutral bino, wino and higgsino states). The parametrization of this mixing leads to some dimensions in the parameter space. In the case of the charginos, the wino mass parameter M_2 , the higgsino mass parameter μ and the mixing $\tan\beta$. For neutralinos we also have a bino mass parameter M_1 . When one of the parameters is significantly small, the physical states are dominated by specific states and we use the nomenclature bino-line ($M_1 \ll M_2, \mu$) and similarly for wino-line ($M_2 \ll M_1, \mu$) and higgsino-like ($\mu \ll M_1, M_2$). Furthermore we can assume GUT unification of masses, which sets $M_1 = \frac{5}{3} \tan^2 \theta_W M_2$ for θ_W the weak

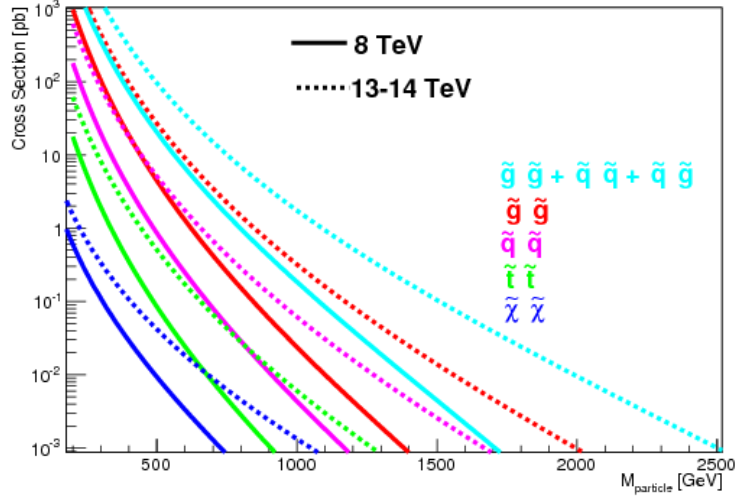


Figure 4.1: Cross sections for the pair production of different supersymmetric particles at the LHC for different mass particles. Results are shown for previous 8 TeV runs (solid) as well as for 13-14 TeV runs (dashed). Results for squarks and gluinos are computed using resummation procedures, whereas results for electroweak partners are computed using fixed-order results, motivating results from this chapter. Plot from [4].

mixing angle.

We will now revise the case of the charginos. When kinematically allowed the dominant decay mode of the charginos is the two-body process into two fermions, for example $\tilde{\chi}^{\pm} \rightarrow l\tilde{\nu}$ and $\tilde{\chi}^{\pm} \rightarrow \tilde{l}\nu$. If this process is kinematically constrained then the three-body process $\tilde{\chi}^{\pm} \rightarrow f\tilde{f}'\tilde{\chi}^0$ through virtual W or sfermions. When sfermions are heavy the dominant channel will be the W and branching ratios will be similar to W decay, whereas where sleptons are lighter and play a more significant role leptonic final states are enhanced.

These channels have been probed in different hadron colliders (LEP, Tevatron and LHC): At LEP a general lower limit of 103.5 GeV has been found through hadronic, semi-leptonic and leptonic decay modes [62, 63], except in areas of the parameter space with low sneutrino masses where there is destructive interference in chargino production, or where the mass difference between $\tilde{\chi}^{\pm}$ and $\tilde{\chi}^0$ is small. In those areas a lower limit of 92 GeV was set.

At Tevatron the focus was on associated $\tilde{\chi}_1^{\pm}\tilde{\chi}_2^0$ production, and final states with multilepton states provided the best signal against the large multijet background [64, 65]. Analysis focused on signals of at least three charged isolated leptons, for two leptons with missing transverse momentum, or two leptons with the same charge.

The program at LHC follows a similar strategy to that of Tevatron.

Since cross section for gauginos is in the relevant range at least a couple orders of magnitude smaller than for colored particles, high statistics is required. With LHC Run 1 and the first results of Run 2, ATLAS and CMS have started to improve on previous LEP and Tevatron constraints of SUSY parameter space. We will analyze then these results in more detail.

For chargino pair production the signal is searched for in the dilepton plus missing momentum channel. In a simplified model of interpretation of results, that assumed chargino decay by light sleptons, ATLAS finds a chargino mass constraint of 740 GeV for massless LSP [66] but no limits can be established for $\tilde{\chi}_1^0$ of 350 GeV or more. This limit is quite robust against slepton mass except where masses of chargino and slepton becomes similar. At the 8 TeV Run, a chargino mass limit of 180 GeV was also established through W boson decay [67] for massless LSP but no limits can be established for LSP masses of 25 GeV or more.

The trilepton plus missing momentum signal can be used to set limits on $\tilde{\chi}_1^\pm \tilde{\chi}_2^0$, assuming wino-like $\tilde{\chi}^\pm$ and $\tilde{\chi}_x^0$, bino-like $\tilde{\chi}_1^0$ and $m_{\tilde{\chi}^\pm} = m_{\tilde{\chi}_2^0}$. Branching fractions of lepton final states will be determined by the slepton masses. If we further assume \tilde{l}_R heavy the decay will be mediated mainly by \tilde{l}_L and the three lepton flavors will be produced in equal amounts. It is further assumed that sneutrinos have masses equal to $m_{\tilde{l}_L}$. With these constraints, chargino masses can be constrained at 1140 GeV by ATLAS [66] and CMS [68] for massless LSP. Limits cannot be established for LSP masses above 700 GeV. If, on the other hand, the decay is dominated by a light \tilde{L}_R the chargino will have a large higgsino component, and decay to τ will be favored. In this scenario, if a flavor-democratic case is assumed, CMS sets limits of 1060 GeV on the chargino mass for massless LSP, and if the assumption is that both $\tilde{\chi}^\pm$ and $\tilde{\chi}_2^0$ decay to τ in the final state the limit lowers to 620 GeV for massless LSP [68]. ATLAS on the other hand assumed a simplified model with $\tilde{\tau}$ significantly lighter than the other sleptons to obtain a multi-tau final state, setting a chargino mass limit of 760 GeV in that case [69].

In the case of heavy sleptons, the chargino is assumed to decay to a W boson plus LSP and the $\tilde{\chi}_2^0$ into Z or H plus LSP. In the WZ channel limits on the chargino mass can be set at 610 GeV for massless LSP by both ATLAS [66] and CMS [70], but no limits are set for LSP above 250 GeV. In the WH channel using $m_H = 125$ GeV with the Higgs decaying to $b\bar{b}$, $\gamma\gamma$ and WW by ATLAS [71] plus ZZ and $\tau^+\tau^-$ by CMS [70] assuming SM-like branching ratios, chargino masses up to 480 GeV for massless LSP can be set, and no limit for LSP above 100 GeV.

For the electroweak gaugino searched in simplified models [72, 73] for light or decoupled sleptons, ATLAS and CMS have comparable limits. In the wino and the higgsino regions the neutralino $\tilde{\chi}_1^0$ and the chargino $\tilde{\chi}_1^\pm$ have similar masses, the chargino decay products are soft. Since this is a difficult experimental case, some dedicated strategies are being followed, yet

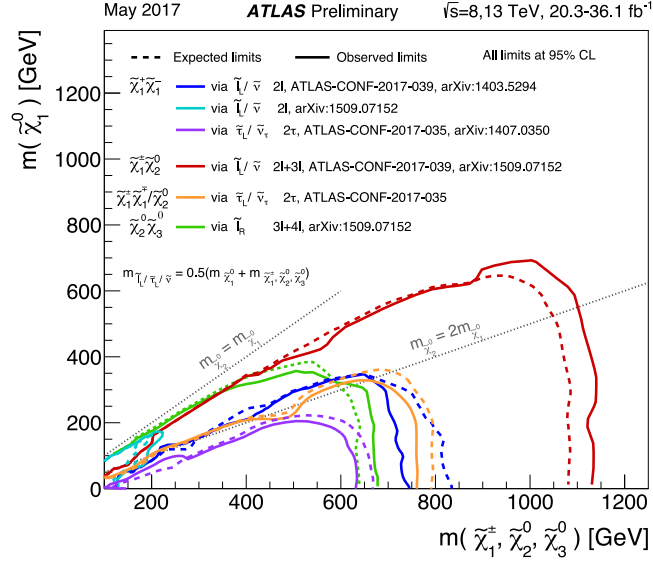


Figure 4.2: Current gaugino mass limits at 95% C.L. [4] for gaugino pair production from ATLAS experiment results at LHC under the assumption of light sleptons.

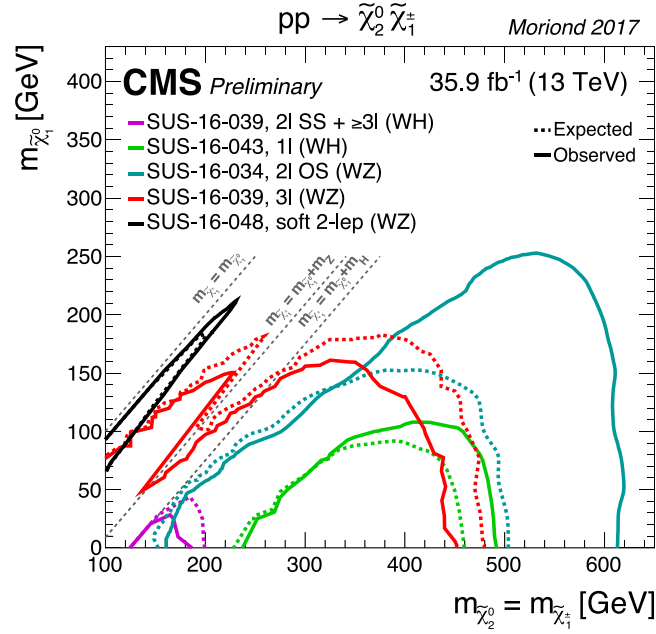


Figure 4.3: Current gaugino mass limits at 95% C.L. [4] for gaugino pair production from CMS experiment results at LHC under the assumption of decoupled sleptons and chargino decay through W^* , Z^* , H .

with limited sensitivity. Photons or jets can be used to tag such decays. As an alternative vector-boson fusion with two additional jets with large a rapidity gap can be used to suppress backgrounds.

We now switch the focus to neutralino searches. In a wide area of the MSSM parameter space for a viable dark matter candidate the LSP is the lightest neutralino $\tilde{\chi}_1^0$. Given its properties and that it is only weakly interacting it will escape detectors, and therefore detection must be done indirectly. Limits on invisible width of the Z boson could apply for neutralinos with a mass below 45.5 GeV, but they depend on the coupling which could be vanishing, and therefore no general constraint of the mass of the lightest neutralino can be set [74]. With GUT mass-unifying models a lower limit can be found from direct searches at around 47 GeV [4]. In even more constrained models like the cMSSM the limit can be improved to 50 GeV from LEP and improved by LHC to above 200 GeV [4]. In the case of gauge-mediated SUSY breaking (GMSB), the LSP will be typically a gravitino and the phenomenology is mostly determined by the nature of the NSLP. If this is a neutralino it will decay to a gravitino and a SM particle determined by the nature of that neutralino. For the case of bino-like neutralinos states with high p_T photons and missing momentum signatures can be interpreted [75, 76, 77, 78, 79]. For decays with at least two neutralinos per event, neutralinos with large non-bino components can be searched for through final states with missing momentum plus two SM bosons of γ, Z, H . This leads to a rich phenomenology explored by LHC [68, 78, 79, 80, 81].

Apart from the lightest neutralino, $\tilde{\chi}_1^0$, some searches have also focused especially on the heavier $\tilde{\chi}_2^0$. Some searches with a combined chargino production have been discussed in this section, from the assumption of equal masses $m_{\tilde{\chi}_1^\pm} = m_{\tilde{\chi}_2^0}$ the mass limits for the chargino $\tilde{\chi}_1^\pm$ also apply to the neutralino $\tilde{\chi}_1^0$. Another one of the main channels is the decay into a $\tilde{\chi}_1^0$ plus an SM boson γ, Z, H . Multilepton analyses can be used to set limits on $\tilde{\chi}_2^0\tilde{\chi}_3^0$ production, which by assuming equal mass and decay through light sleptons leads to a limit of 680 GeV for massless LSP [72]. Also channels with a $\tilde{\chi}_2^0$ decaying into $\tilde{\chi}_1^0$ have been probed and shown to be useful in measuring mass differences in case of signal [72] and even in the search itself [80, 82].

If we also consider models with R -parity violation, the LSP can decay into a multilepton final state, and these states have also been looked into. For decays with nonzero λ events with four or more charged lepton are analyzed [83], and for small couplings lepton pairs. In the case of nonzero λ' coupling events with a displaced hadronic vertex [84], and in the case of nonzero λ'' for hadronic final states and jet pair resonances.

Outside the simplified models, work on the phenomenological MSSM (pMSSM) has shown that the simplified models cannot capture some relevant physical phenomenology. In particular, LSPs compatible with the known dark matter relic density constraints need specific values of mixing

parameters and masses that are not properly captured by the simplified models.

4.2 Benchmark points

SUSY results by the LHC starting ruling out most of the SPS benchmark points that had been long in use [85], so these cMSSM points were replaced [61]. From the analogous magnetic momentum of the muon $(g - 2)_\mu$ and rare decay $b \rightarrow s\gamma$ models with positive off-diagonal Higgs mixing $\mu > 0$ and vacuum expectation values of the neutral components of the two Higgs doublets $\tan\beta$ and universal soft trilinear coupling of the Higgs fields to squarks at GUT scale A_0 satisfying $\tan\beta = 10, A_0 = 0 \text{ GeV}$ or $\tan\beta = 40, A_0 = -500 \text{ GeV}$ were chosen. A total of 49 benchmark points were selected for detailed studies.

For this study 13 out of the total 49 points were chosen in the two model lines 10.1 and 10.3 with $\tan\beta = 10, A_0 = 0 \text{ GeV}$ plus 7 points on the line 40.1 with $\tan\beta = 40, A_0 = -500 \text{ GeV}$. For more detailed analyses and for comparison with Monte Carlo predictions we focus on one specific benchmark point for each line.

For the first point with $\tan\beta = 10, A_0 = 0 \text{ GeV}$ we choose an optimistic scenario with low universal scalar mass m_0 as well as the universal gaugino mass $m_{1/2}$, which corresponds in particular to the point 1 of the LPCC numbering scheme. These parameters lead to a neutralino and chargino mass at the electroweak scale of about 150–550 GeV. Gluino and squark masses lie in the 1–2 TeV range and therefore in the allowed region from current ATLAS and CMS constraints. The production of $\tilde{\chi}_1^\pm$ together with $\tilde{\chi}_2^0$ leads often to the golden trilepton signature. We note that indeed for all the scenarios on 10.1 the lightest chargino and the sleptons always decay in first approximation to a single observable lepton and missing transverse energy.

For the second point we chose point 18 in the LPCC numbering schema, which lies on the model line 10.3. This point also has Higgs VEVs set to $\tan\beta = 10$ and vanishing trilinear coupling A_0 . This point has higher values for the universal scalar m_0 and gaugino masses $m_{1/2}$ giving slightly heavier neutralino and chargino masses in the range 250–770 GeV, whereas the squark and gluino masses stay in a similar range as point 1 in the 1–2 TeV so this point is also not excluded by ATLAS and CMS current constraints. The next-to-lightest neutralino decays mostly to a Higgs boson since it is almost pure light wino and cannot decay into heavier superpartners of the left-handed leptons and quarks. Also because of the heavy squark masses t - and u -channel squark diagrams leading to neutralino and gaugino pair production are suppressed. Final states containing one or two neutralinos $\tilde{\chi}_2^0$ are significant via s-channel weak boson exchanged with reduced destructive

interferences with the t and u channels. Since the lightest chargino decays with a 89% branching ratio to a W boson one can obtain the production rate of golden signatures from the values of the $\tilde{\chi}_2^0 \tilde{\chi}_1^\pm$ total cross sections presented in the next section after accounting for the branching ratio of a Higgs boson decaying into a pair of tau leptons and the rate of lepton W boson decays.

Finally the third selected point is point 31 in the LPCC numbering scheme, which lies in a model line similar to that of 40.1, with a large value of $\tan\beta = 40$ and large $A_0 = -500$ GeV. As in the second chosen point, we keep high universal scalar and gaugino masses. The neutralino and chargino masses are similar to those in point 18 since they do not depend drastically on the $\tan\beta, A_0$ parameters, and are in the range 250–825 GeV. Similarly with the gluino and first and second generation squark masses. However, the different $\tan\beta, A_0$ do have an important effect in the mixing among the third generation squark interaction eigenstates and (with a somewhat smaller impact) the $\tilde{\tau}$ states. From this, the masses of the lightest \tilde{t} and \tilde{b} are much lower than the average squark mass and these states are almost maximal admixtures of the left- and right-handed third-generation squark eigenstates. We also present in Tab. ?? the two main decay modes of the second neutralino, to an associated pair of stau (decaying later to a τ and $\tilde{\chi}_1^0$) and tau lepton but also at a smaller rate to a Higgs boson and missing energy carried by the lightest neutralino. As in the previous chosen points, the tripleton cross section can be deduced from the values of the total cross sections of the next section together with the branching ratios of the lightest Higgs boson to taus and the one of the tau leptonic decays.

We notice that although future experimental limits of the squark and gluino masses might exclude these cMSSM scenarios, the gaugino masses may still remain viable and their total cross sections will be approximately valid.

4.3 Total cross sections

In this section we will present next-to-leading logarithm computations for chargino and neutralino production in the benchmark points presented in Sec. 4.2. These processes have been computed initially at the leading order in the QCD running α [86] and later polarization [87] and flavor-violating [42] effects have been included. Additionally next-to-leading order corrections have been included [44] sizable due to large logarithmic contributions from soft and collinear parton emissions. Since these contributions can spoil the convergence of the perturbative series resummation procedures are necessary for reliable predictions over the relevant areas of the phase space. Transverse momentum and threshold resummation have been performed at next-to-leading logarithmic accuracy [44].

First we present in Tab. ?? total production cross sections for neutralino and chargino pairs for benchmark points 1, 18 and 31 as presented in Sec. 4.2 at the NLL threshold resummation order matched to NLO results. The LO results are computed as in [87] convoluting unpolarized partonic cross sections with the LO set of MSTW 2008 PDF with five light flavors of massless quarks as agreed by SUSY working groups of ATLAS, CMS and the LPPC. The top quark mass is set at 173.1 GeV and $m_Z = 91.1876$ GeV and $m_W = 80.403$ GeV, setting the CKM matrix to the identity matrix. The relevant SUSY spectra have been generated using SuSpect to obtain low-energy masses and parameters from the GUT values evolved down through renormalization group running at the two-loop level. The central value is found setting the factorization scale μ_F to the average final state particle masses of the produced pair and uncertainties are estimated by multiplying the central value of μ_F by factors in the 0.5–2 range. For NLO predictions the detailed computations can be found in [87] where the SM and SUSY QCD contributions are included. For NLO we use the corresponding MSTW 2008 NLO PDF sets and the theoretical uncertainties for the scale variation are performed simultaneously for μ_F and μ_R by multiplying the average particle mass by a factor 2. For PDF, the uncertainties are derived following the PDF set recommended approach, i.e. as defined by the formulas

$$(\Delta\sigma_+)^2 = \sum_{k=1}^n \{\max(\sigma_k^+ - \sigma_0, \sigma_k^- - \sigma_0, 0)\}^2, \quad (4.1)$$

with σ_0 the cross section value as computed with the central set of the PDF and σ_k^+, σ_k^- are those obtained from the $\pm\sigma$ variation along the k^{th} eigenvector of the covariance matrix of the PDF fit, and similarly

$$(\Delta\sigma_-)^2 = \sum_{k=1}^n \{\max(\sigma_0 - \sigma_k^+, \sigma_0 - \sigma_k^-, 0)\}^2, \quad (4.2)$$

with the same notations.

The numerical results show some expected features from resummation total cross sections. In the first place, we observe the large scale uncertainty of the LO results, due to the induced large logarithmic terms to give around a 10% uncertainty. This is reduced at NLO though one obtains a further renormalization scale dependency through the coupling constant in the loop contributions. We observe however that after the matching to the resummation NLL terms this dependency is reduced thanks to the dominant contributions being included in the Sudakov factor \mathcal{G} . We also observe that PDF uncertainties are not significantly reduced, which is expected since they use the same PDF sets as for NLO results.

We now show the results for the golden trilepton channel $\tilde{\chi}_2^0 \tilde{\chi}_1^+$ total cross sections as a function of their (almost equal) mass $m_{\tilde{\chi}}$ at the LHC

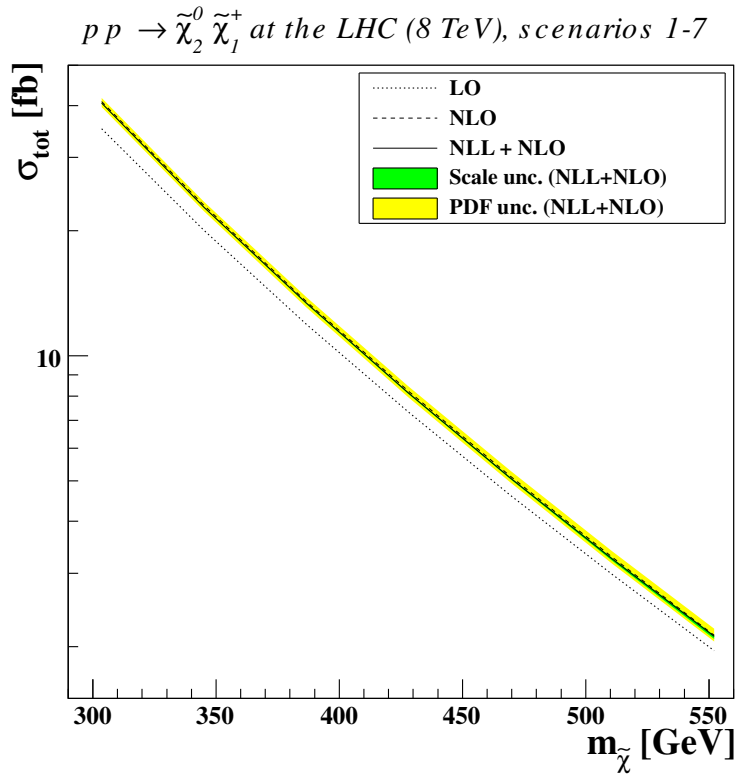


Figure 4.4: Total cross section for gaugino pair production at LO (dotted), NLO (dashed) and NLO+NLL (solid) with scale (green) and PDF (yellow) uncertainties for $\tilde{\chi}_2^0 \tilde{\chi}_1^+$ pair production as a function of their degenerate mass $m_{\tilde{\chi}}$ at the LHC at 8 TeV for benchmark points 1-7.

with 8 TeV center-of-mass energy. The results of the model line 10.1 can be seen in Fig. 4.4 for LO, NLO and NLO+NLL cross sections. The soft SUSY-breaking mass increases from 400 GeV to 700 GeV, with the gaugino masses increasing from 300 GeV to 550 GeV, and the total cross section decreasing as expected, from ~ 40 fb to ~ 2 fb. We observe a sizable NLO correction and similar NLO+NLL total results, decreasing however in uncertainty. As discussed above, the main source of uncertainty then becomes the PDF contributions. Similar results are obtained for model lines 10.3 and 40.1.

4.4 Invariant mass and transverse momentum

Signatures of gauginos and higgsinos production typically involve significant initial state QCD radiation, which has a big impact on kinematical distributions due to the potentially large logarithmic contributions in the soft and collinear regions. To obtain reliable predictions in this case it is necessary to treat these logarithmic terms at all orders in the strong coupling constant. We have analyzed how this can be done at the next-to-leading order through resummation procedures matched to next-to-leading fixed order, which leads to an appropriate description both in the soft and collinear regions as well as in the hard regions (due to the fixed-order matching). Experimental and phenomenological studies sometimes rely on Monte Carlo simulations with simulations of jet productions by using tools such as Herwig [88] or Pythia [89] which simulate QCD emission by probabilistic branching of parton using Markov Chain techniques built using the Sudakov form factor. These tools typically use only leading-logarithm accuracy (as opposed to the next-to-leading-logarithms accuracy presented in the resummation techniques employed here), sometimes including only partial next-to-leading-logarithm contributions. This is a limitation of the Monte Carlo algorithms used. Also, supersymmetric processes are typically only implemented at the leading-logarithm level and are not fully implemented into NLO tools such as MC@NLO [90] or Powheg [91].

Matrix-element approaches are accurate for hard and separated emissions, but fail in the soft and collinear limits, whereas parton showers give accurate results in the soft and collinear limits but underestimate hard emissions, which leads to the need of matching algorithms. Developments in this area include the Carani-Krauss-Kuhn-Webber (CKKW) scheme [92] and the Mangano scheme [93]. The reader is referred to the references for details on these approaches. The key property is that they avoid the double counting that arises from combining the matrix element and the parton shower results from the Sudakov form factor. These algorithms have been applied to both SM and BSM theories (see [4] and references therein for a review).

In this section we will present a comparison of between fixed next-to-leading order results, resummation up to the next-to-leading-logarithms re-

sults matches to next-to-leading order and parton showering matched to matrix elements for charginos and neutralinos for transverse momentum p_T and invariant mass M distributions. For the parton showering will follow the hard matrix elements matched following the MLM k_T scheme using the implemented in MadGraph MadEvent generator [94] with Pythia. The UFO model files [95] will be generated using FeynRules [96] for the different benchmark points obtained with SuSpect [97]. Three parton-level event samples will be generated with the pair of supersymmetric particles plus zero, one, and two extra partons. These will be merged after parton showering using the MLM scheme. The jets are generated with a minimum of $k_T \geq 50$ GeV where

$$k_T^2 \equiv \min(p_{Ti}^2, p_{Tj}^2) R_{ij} \quad (4.3)$$

for i, j the final state partons and R_{ij} the angular distance in the (η, ϕ) plane. When one of the partons is an initial state parton, the jet measure is defined as

$$k_T \equiv p_{Ti} \quad (4.4)$$

and we require in this case $k_T \geq 20$ GeV. The events are then showered using Pythia and jets reconstructed using FastJet [98] with the k_T -jet algorithm with a cutoff scale $Q = 70$ GeV. The events are selected if each jet is matched to one parton (with the exception of the two-jet sample), i.e., is the k_T -measure is smaller than Q .

As is usual we neglect all quark masses except the t quark, and use the MSTW 2008 PDF at the LO and NLO levels. The factorization and renormalization scales for the resummation method are set at the average of the mass of the final state particles, whereas for the showering algorithm is set at the jet measure at each branching. Since the value of the total cross section of the matched event sample is usually close to the original tree-level process, we reweight the produced events to the resummed cross sections obtained. We also perform on-shell subtraction of intermediate resonances which could appear in the sampled with extra partons using narrow-width approximation. Finally we employ MadAnalysis for the final results analysis.

4.4.1 Invariant mass distributions

We focus now our analysis in the invariant mass distribution $d\sigma/dM$ of the gaugino pair for the production of a lightest chargino $\tilde{\chi}_1^+$ and second lightest neutralino $\tilde{\chi}_2^0$ as shown in Fig.4.5 in the benchmark point 1. We present results for threshold resummation, fixed-order NLO calculation and LO Monte Carlo simulations with MadGraph interfaced to Pythia, which is normalized to the total resummation cross section. We find the results to be very close. We show the spectrum from $M \sim 600$ GeV since the two gauginos have similar masses of $m \sim 300$ GeV. The shape is mainly the result of the

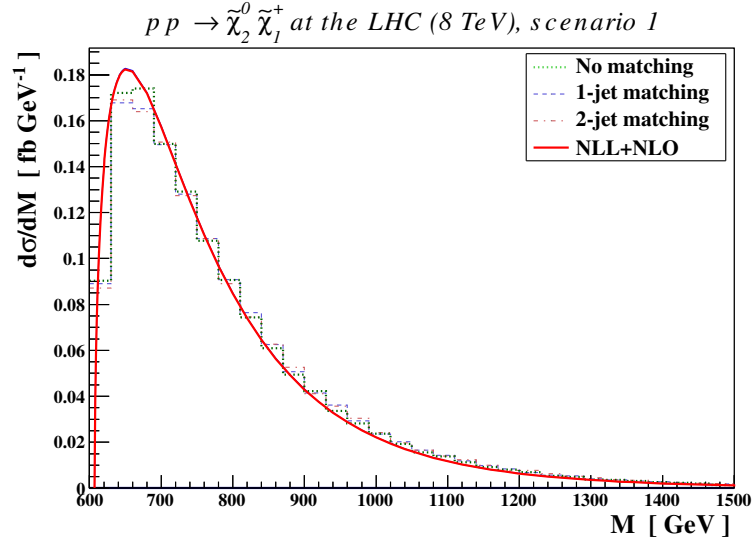


Figure 4.5: Invariant mass distribution for $\tilde{\chi}_2^0 \tilde{\chi}_1^+$ pair production with a mass of 304 GeV (benchmark point 1) at the 8 TeV LHC at NLO+NLL (red solid) compared to matrix elements matched to no jet (green), one jet (blue dashed) and two additional jets (red dot-dashed).

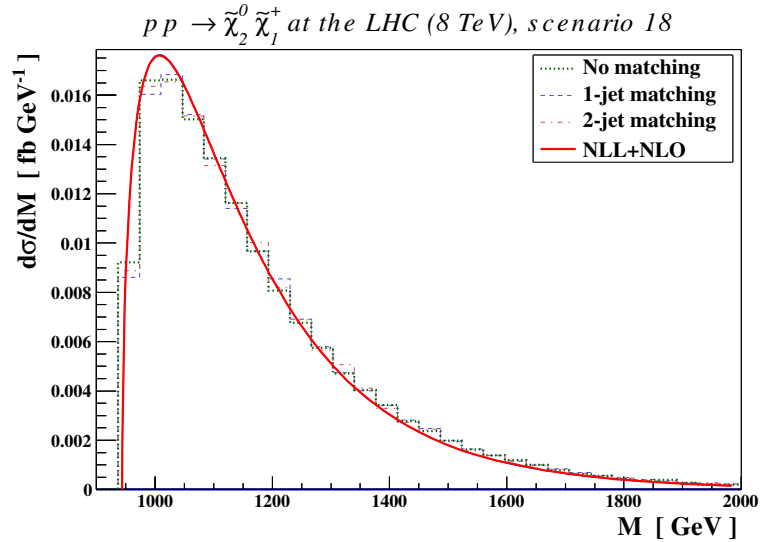


Figure 4.6: Same as Fig. 4.5 for benchmark point 18.

gaugino nature of the outgoing sparticles, since this leads to a suppression of the s channel W boson exchange with respect to the P wave production through t and u squark exchange channels with the mass of the squarks being ~ 800 GeV. The resummed contributions are similar to the fix order results since threshold effects are most relevant in the production threshold limit, i.e. with the invariant mass similar to the center-of-mass energy. The curves obtained by the different MadGraph and Pythia agree well with each other. They correspond to three different matching procedures. The “no-matching” scenario corresponds to the tree-level matrix element only, i.e. the process $pp \rightarrow \tilde{\chi}_2^0 \tilde{\chi}_1^+$ without extra radiation. Parton-level events were passed to Pythia for parton showering with no matching procedure applied, and results were normalized to the resummed results. The “1-jet matching” results has been obtained by applying the k_T -MLM matching procedure by incorporation the matrix elements containing one additional QCD emission, i.e. adding the process $pp \rightarrow \tilde{\chi}_2^0 \tilde{\chi}_1^+ j$ to the previous matrix elements with j a quark, antiquark or gluon, and matched consistently to parton showering. We again normalize to the total resummed cross section. Finally the third plot line “2-jet matching” corresponds to the addition of up to two extra partons as before, summing in this case the contribution from $pp \rightarrow \tilde{\chi}_2^0 \tilde{\chi}_1^+ jj$. For the cases of benchmark points 18 and 31 the gaugino masses are heaving at $m_{\tilde{\chi}} = 472$ GeV and $m_{\tilde{\chi}} = 479$ GeV which leads to a reduced cross section for the pair production by about an order of magnitude down to 5.22 fb and 4.81 fb respectively. The resulting behavior (using the new K factors for normalization of the MadGraph plus Pythia results) is very similar as before. We show the case of benchmark point 18 for reference in Fig.4.6.

4.4.2 Transverse momentum distributions

We now show the transverse-momentum distribution $d\sigma/dp_T$ of the combined production of lightest chargino and next-to-lightest neutralino pair $\tilde{\chi}_1^+ \tilde{\chi}_2^0$. It is easy to see that in this case the fixed-order result diverges in the limit p_T as expected because of the non-canceled logarithmic terms of the soft parton radiation. After matching to the resummed calculations the finite behavior is restored. More importantly we also observe that the effects of resummation are not confined to the $p_T \rightarrow 0$ limit but extend to intermediate transverse momentum values giving a considerably different curve shape as expected.

Similarly as before, we now analyze the three different predictions obtained with MadGraph in combination with Pythia. Again we normalize the total production rate to the resummed cross section values. We observe a good agreement between the resummed result with the MadGraph and Pythia results with additional jets, but we observe that a simple parton showering without extra jets results in a significant divergence in the mod-

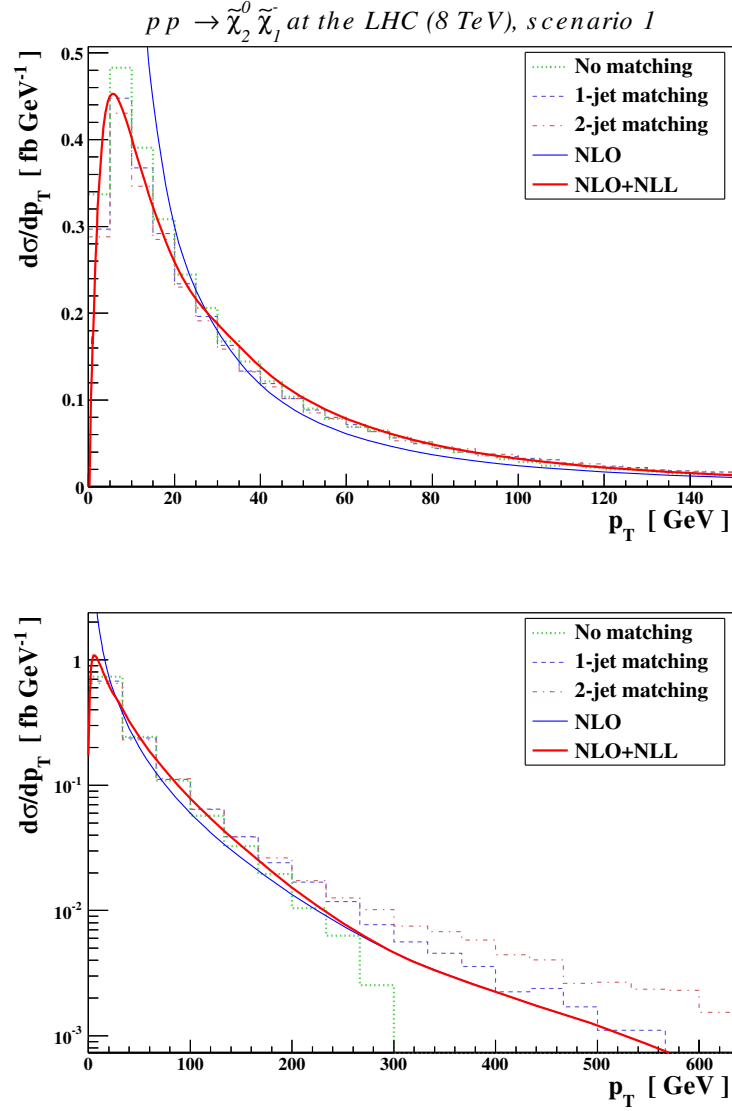


Figure 4.7: Transverse momentum p_T distribution for $\tilde{\chi}_2^0 \tilde{\chi}_1^+$ pair production for benchmark point 1 at LHC 8 TeV at fixed-order NLO (blue solid), NLO+NLL (red solid) compared to matrix elements matched to no jet (green dotted), one jet (blue dashed) as well as two jets (red dot-dashed).

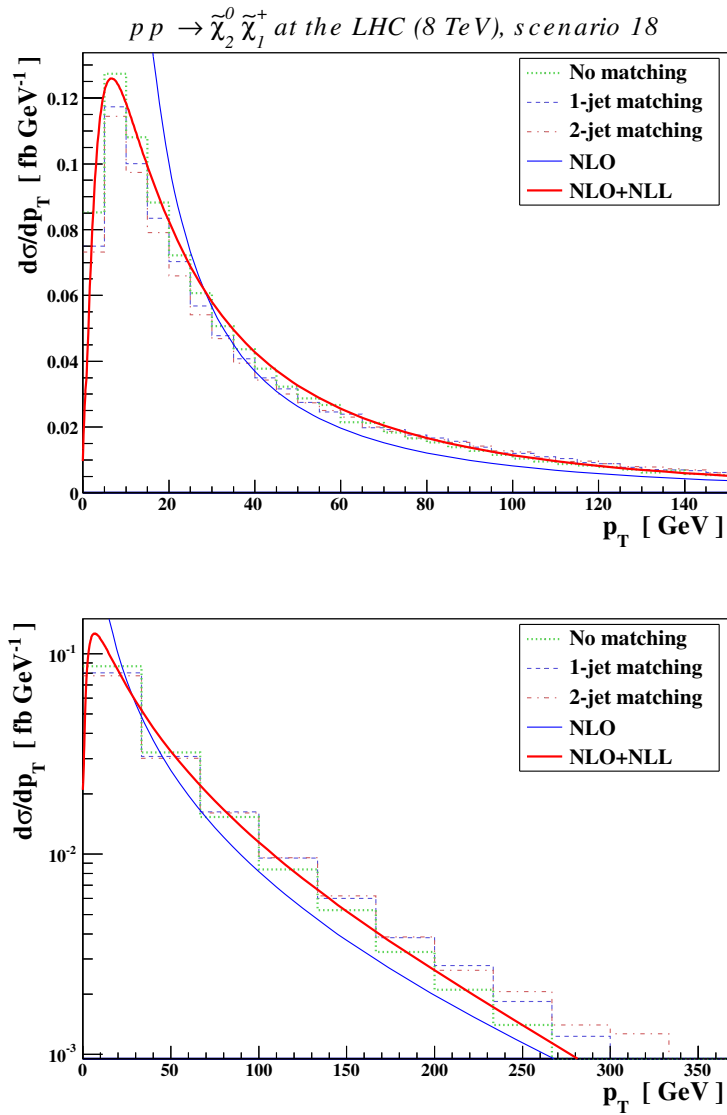


Figure 4.8: Same as Fig. 4.7 for benchmark point 18.

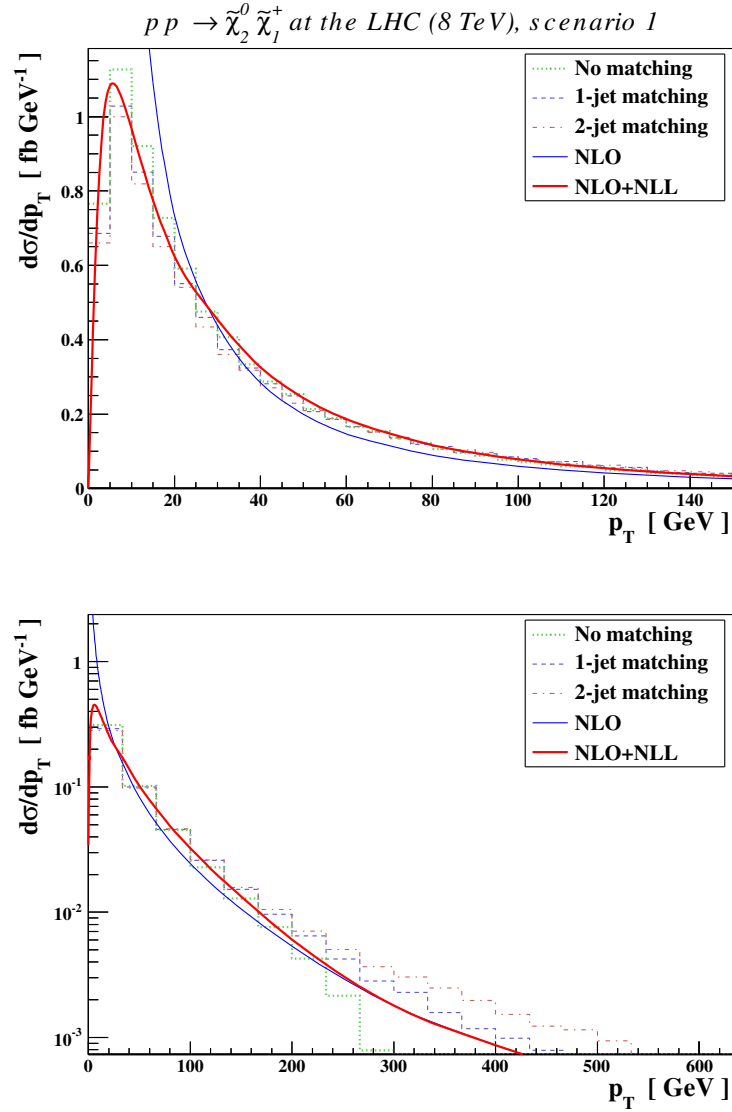


Figure 4.9: Same as for Fig. 4.7 for $\tilde{\chi}_1^- \tilde{\chi}_2^0$ pair production.

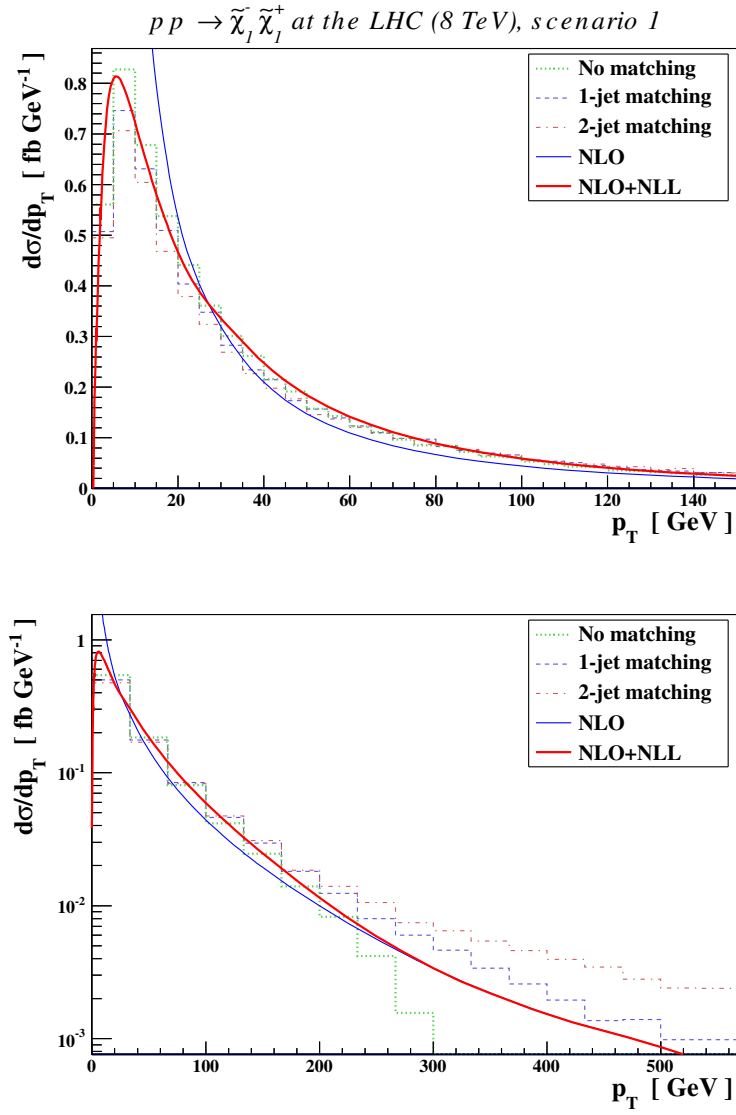


Figure 4.10: Same as for Fig. 4.7 for $\tilde{\chi}_1^+ \tilde{\chi}_1^-$ pair production.

erate p_T region, which is expected since parton showering methods do not properly address that kinematical region. In general, in the moderate p_T region we can observe a visible departure from agreement (as opposed to the invariant-mass case) for all three matching procedures. The peak position does not depend heavily on the presence of additional partons at the matrix level, but the global shape of the spectrum does. We can finally notice that the best match at those kinematical regions corresponds to the “1-jet” case, which is to be expected since that is the same matrix element levels used in the resummed case. Qualitatively similar results are obtained for benchmark point 18 in Fig. 4.8 as shown, only with rates around an order of magnitude smaller due to the larger gaugino masses. We also show in Figs. 4.9 and 4.10 the production of pairs $\tilde{\chi}_1^- \tilde{\chi}_2^0$ as well as $\tilde{\chi}_1^+ \tilde{\chi}_1^-$, again with the Monte Carlo curves normalized to the resummed values. The distributions are similar to the golden channel, but the absolute size of the latter is larger as expected for proton-proton collisions.

Part II

Minimal models

Chapter 5

Dark matter

*There are more things in heaven and earth,
Than are dreamt of in your philosophy.*

— William Shakespeare, *Hamlet*.

There is plenty of evidence, which ranges from dwarf galaxies scales to the largest cosmological scales, that the current cosmological model based on Einsteins general relativity applied to the visible matter cannot explain certain observed behaviors. As always when this kind of problems arise, when of our two premises must be false, i.e. either there is some yet unseen type of matter that accounts for the deviations, or we have to modify the current laws of physics. And in the history of science we certainly have had examples of both cases: When the motion of Uranus seemed to show anomalous, Le Verrier and Couch proposed the existence of Neptune, eventually discovered; but when the anomalies in the movement of Mercury were explained by an unseen planer Vulcan failed, we had to wait until Einsteins theory of relativity allowed us to make more precise gravitational predictions. We face a similar situation with dark matter today, although in this case, as we will see, there are reasons that make us believe that this time it is indeed a form of matter yet to be discovered.

In this chapter we will first review the current evidence for dark matter existence and some of the most promising models that account for this observed anomalies. After that we will analyze the current status of experimental detection, and finally show some standard calculations that will be required on following chapters.

5.1 Evidence for dark matter

The first observations of the existence of dark matter were realized by Zwicky in the 1930's when he measured the velocity dispersion of galaxies in the Coma cluster, which led him to find the they could not be explained by the

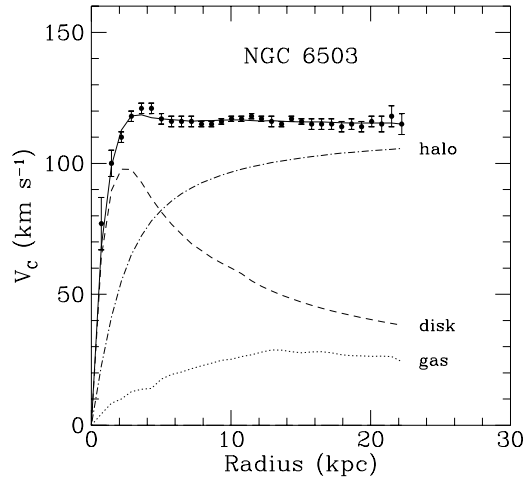


Figure 5.1: Expected and observed (solid) rotational circular velocity for several luminous objects as a function of the distance to the center. The observed value becomes flat for large r . Plot from [100].

gravitational attraction of the stars, gas and dust observed. He arrived to the conclusion that there was about six times more mass than what was visible.

5.1.1 Anomalous velocity of luminous objects

One of the oldest yet most convincing evidences for dark matter existence comes from the discrepancy between the expected and observed velocity profiles of various luminous objects, which range from stars, gas clouds, globular cluster and even entire galaxies [99]. In particular, the rotation curve of galaxies, which can be measured by combining observations of the 21 cm with surface photometry.

The expected circular velocity $v(r)$ is expected from Newtonian mechanics to vary as a function of the radius as

$$v(r) \propto \sqrt{\frac{M(r)}{r}}, \quad (5.1)$$

where $M(r) := 4\pi \int \rho(r)r^2 dr$ is the mass inside the sphere of radius r with $\rho(r)$ the density profile. However the observed velocity profile becomes flat at large r , as can be seen in a typical example in Fig. 5.1.1.

5.1.2 Gravitational lensing

A “direct” observation of dark matter densities is achieved through what is known as gravitational lensing. As predicted by General Relativity, photons

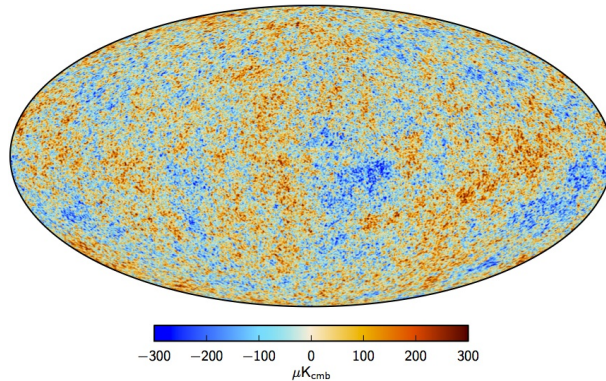


Figure 5.2: Cosmic Microwave Background variations as measured by Planck [101].

are deflected when passing through a region with some mass density due to the space-time deformation, which modifies the apparent shape and flux of the light source. This can be used to observe properties. In particular, it can be seen [100, Ch. 4] that the deflection angle can be expressed as

$$\alpha(\mathbf{x}) = \frac{4G}{c^2} \int \Sigma(\mathbf{x}') \frac{\mathbf{x} - \mathbf{x}'}{|\mathbf{x} - \mathbf{x}'|^2} d^2\mathbf{x}', \quad (5.2)$$

which in the point mass approximation simplifies to

$$\alpha = \frac{4GM}{c^2 x}, \quad (5.3)$$

where x is the impact parameter.

Arguably the most prominent example of such observations is the Bullet cluster (1E0657-558), which passed through another cluster, and hot gas was decelerated and the galaxies obeyed ballistic trajectories. Gravitational lensing was used to infer that most of the total mass also moved ballistically, indicating weak self-interaction [100].

5.1.3 Cosmological measurements

The most accurate determination of dark matter density so far comes from cosmological measurements from cosmic microwave background (CMB). On the other hand these determination relies on the assumption of a particular cosmological model, namely the Standard Model of cosmology, plus some assumptions on dark matter, in particular that it is cold, i.e. it has negligible velocity with respect to structure formation, the Λ CDM model.

Discovered in 1965 [102], The CMB constitutes the main form of radiation in the universe, and is well described by a black body radiation with $T \approx 2.73$ K. The current state-of-the-art measurements come from ESA's

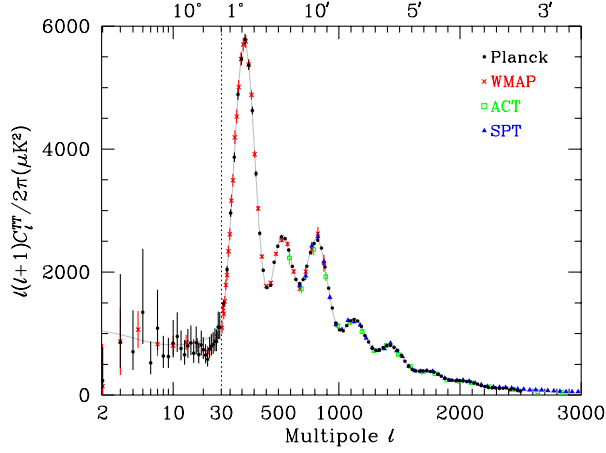


Figure 5.3: Multipole expansion of the Cosmic Microwave Background as measured by Planck [101].

Planck experiment [101] complemented by ground-based experiments such as the Atacama Cosmology Telescope, which have superseded the previous NASA’s WMAP [103] and the older seminal measurements by the COBE satellite [104]. The main observable is the very small intensity differences with respect to the observation angle, and to a minor extent the polarization. The temperature profile can be expanded using the spherical harmonic expansion as

$$T(\theta, \phi) = \sum_{lm} a_{lm} Y_{lm}(\theta, \phi). \quad (5.4)$$

The two-point function averaging over the modes is therefore

$$C_l = \sum_m \frac{|a_{lm}|^2}{2l+1}, \quad (5.5)$$

which can be seen in Fig. 5.1.3.

The universe is considered to obey Einstein’s equations with a perturbed Robertson-Walker metric. The fitted parameters [4]

$$\Omega_{\text{nbm}} h^2 = 0.1198 \pm 0.0026. \quad (5.6)$$

Some part of the baryonic matter could also contribute to dark matter,

$$\Omega_{\text{b}} h^2 = 0.02207 \pm 0.00027. \quad (5.7)$$

5.2 Models of dark matter

There is plenty of different possible extensions of the Standard Model that contain a dark matter candidate. In this section we will review only the

most relevant possibilities and the most important scenarios, both in supersymmetric and non-supersymmetric theories. The reader is referred to [100, 105] and references therein for further details.

5.2.1 Supersymmetric candidates

One of the main motivations for supersymmetric theories is as we have seen in other chapters the fact that supersymmetric theories contain natural dark matter candidates. In particular supersymmetric theories usually lead to dark matter candidates in the Weakly Interacting Massive Particle (WIMP) framework. WIMPs are particles (usually denoted χ) with cross sections of the order of the weak interaction with masses approximately in the $\sim 10 \text{ GeV} - 10 \text{ TeV}$ mass range [4]. Initially at $T > m_\chi$ they were in thermal equilibrium with SM particles and they “freeze out” once their production and annihilation rates become out of equilibrium. After the freeze out happens the comoving WIMP density remains essentially constant. The freeze out typically happens at $T \sim m_\chi/20$ in many scenarios [4] which means that at freeze out the dark matter candidate is already non-relativistic. More details and the mathematical framework for these calculations is presented later in this chapter in section 5.3.

The most important WIMP candidate is arguably the supersymmetric LSP with exact R-parity [106] as seen in Ch. 2. Since the dark matter candidate must be neutral, sneutrinos and neutralinos are the obvious candidate choices. WIMP searches have ruled out the former (see [4] for a review), but theoretical and especially experimental work continues with the latter. In particular it is known [100] that a neutralino LSP gives rise to the right thermal relic density in several different regions of the parameter space [4]: When the LSP χ is mostly a bino or photino if m_χ and some sleptons have masses somewhat below 150 GeV, or if m_χ is close to the mass of some sfermion (leading to coannihilations), or if $2m_\chi$ is close to the mass of the CP-odd supersymmetric Higgs; or when χ has large higgsino or wino component.

5.2.2 Non-supersymmetric candidates

Outside the supersymmetric framework there are also many different ways to realize dark matter candidates [100]. Some non-supersymmetric theories also contain WIMPs similar to the supersymmetric case. Examples include the lightest T -odd particle in Little Higgs models with T -parity or technibaryons in technicolor theories. Sterile neutrinos are also possible dark matter candidates [107], and extra dimensional theories offer also viable candidates, e.g. in Universal Extra Dimensions (UED) models or as the lightest Kaluza-Klein particle [105]. A full study of these is outside the scope of this chapter. A review of the examples mentioned as well as others can be found

in [4, 100, 105].

5.3 Relic density calculation

An important observable which has been measured with a great precision is the relic density of dark matter particles. At high temperatures dark matter particles were supposed to be in thermal equilibrium with standard model particles. As temperature decreased (time increased)

The density of dark matter particles today can be computed using the Boltzmann equation, which describes the evolution of the number density n of dark matter candidates,

$$\frac{dn_i}{dt} = -3Hn_i - \langle\sigma v\rangle(n^2 - n_{\text{eq}}^2), \quad (5.8)$$

where H is the Hubble parameter and $\langle\cdot\rangle$ represents the thermal average.

The first term in the RHS in (5.8) accounts for the expansion of the universe, and the second term for the annihilations (in both directions).

Combining (5.8) with the equation for the entropy density s , $\frac{ds}{dt} = -3Hs$ and defining $Y := n/s$ and $x := m/T$ with T the photon temperature, we obtain

$$\frac{dY}{dx} = \frac{1}{3H} \frac{ds}{dx} \langle\sigma v\rangle (Y^2 - Y_{\text{eq}}^2). \quad (5.9)$$

The Hubble parameter can be computed using the Friedman equation as

$$H^2 = \frac{8\pi}{3M_{\text{P}}^2} \rho. \quad (5.10)$$

At the same time, the energy and entropy densities can be related to the photon temperature by

$$\rho = \frac{\pi^2}{30} g_{\text{eff}}(T) T^4, \quad s = \frac{2\pi^2}{45} h_{\text{eff}}(T) T^3, \quad (5.11)$$

with g_{eff} and h_{eff} the effective degrees of freedom.

It is customary to define a degrees of freedom parameter $g_*^{1/2}$ by

$$g_*^{1/2} = \frac{h_{\text{eff}}}{g_{\text{eff}}^{1/2}} \left(1 + \frac{1}{3} \frac{T}{h_{\text{eff}}} \frac{dh_{\text{eff}}}{dT} \right), \quad (5.12)$$

which allows us to rewrite (5.9) as

$$\frac{dY}{dx} = - \left(\frac{45}{\pi M_{\text{P}}^2} \right)^{-1/2} \frac{g_*^{1/2} m}{x^2} \langle\sigma v\rangle (Y^2 - Y_{\text{eq}}^2) \quad (5.13)$$

Without coannihilations

$$\langle\sigma v\rangle = \frac{\int_0^\infty dp p^2 W(s) K_1(\sqrt{s}/T)}{m^4 T K_2^2(m/T)} \quad (5.14)$$

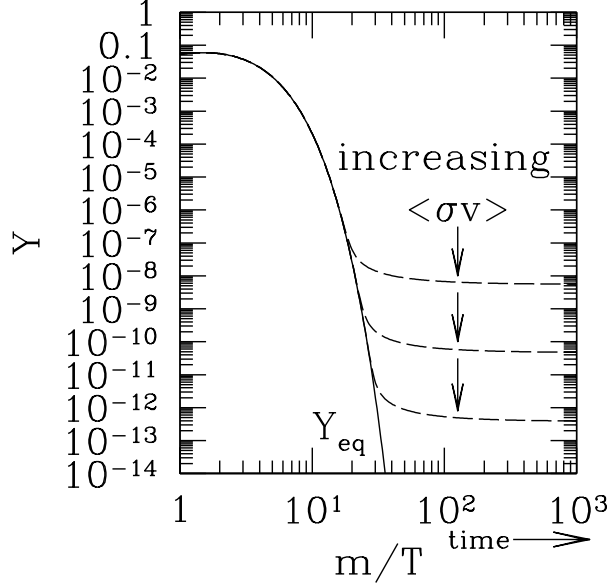


Figure 5.4: Dark matter density as a function of the temperature (time) in a typical freeze-out process [105]. Note the present-day WIMP relic density as a result of the freeze-out and its dependence on the dark matter annihilation cross section via $\langle \sigma v \rangle$.

where $W(s)$ is the annihilation rate per unit volume and unit time,

$$W(s) := 4\sigma_{ij} \sqrt{(p_i \cdot p_j)^2 - m_i^2 m_j^2} \quad (5.15)$$

All that is left is to compute $W(s)$ for our particular process, integrate the thermal average (5.14), insert it into (5.13), and solve it, possibly numerically, with the initial condition $Y = Y_{\text{eq}}$ at $x \approx 1$ to obtain the present WIMP abundance Y_0 . With that, the relic density will be given by

$$\Omega h^2 = \frac{\rho^0 h^2}{\rho_c^0} = \frac{m s_0 Y_0 h^2}{\rho_c^0}, \quad (5.16)$$

with ρ_c^0 the present critical density and s_0 the present entropy density. If we use $T_0 = 2.726$ K and $h_{\text{eff}}(T_0) = 3.91$, which corresponds to photons and three neutrino species, we can compute the prefactors, giving

$$\Omega h^2 \approx (2.755 \times 10^8 \text{ GeV}) Y_0 m. \quad (5.17)$$

A typical numerical solution for (5.13) is shown in Fig. 5.3.

5.4 Dark matter detection

In this section we will study the different dark matter detection possibilities depending on whether the incoming or outgoing particles in the relevant

process investigated are standard model or dark matter candidates.

5.4.1 Direct detection

Direct detection experiments aim to measure the interactions of the dark matter particles in the Milky Way's halo with elastically scatter off nuclei. Assuming a WIMP model for the dark matter candidate, the flux on Earth should be of the order of $(10^5 \text{ cm}^{-2} \text{ s}^{-1})(100 \text{ GeV}/m)$ [100], which is sufficiently large to cause measurable effects. The information the experiments try to measure is the rate R (directional or not) of nuclear recoils and its energy E_R .

The rate R for a nucleus of mass M is given by

$$\frac{dR}{dE_R} = \frac{\rho_0}{mM} \int_{v_0}^{\infty} v f(x) \frac{d\sigma}{dE_R}(v, E_R) dv, \quad (5.18)$$

with ρ_0 the local dark matter density, σ the cross section for the scattering and $f(v)$ the speed distribution in the detector frame.

Since we know that the scattering is non-relativistic, the recoil energy can be obtained in terms of the scattering angle in the center of mass frame easily as

$$E_R = \frac{\mu^2 v^2 (1 - \cos \theta)}{m}, \quad (5.19)$$

where μ is the reduced mass of the dark matter particle-nucleus system.

The total event rate can be obtained by integrating (5.18),

$$R = \int_{E_T}^{\infty} dE_R \frac{\rho_0}{mM} \int_{v_0}^{\infty} v f(x) \frac{d\sigma}{dE_R}(v, E_R) dv, \quad (5.20)$$

for a threshold energy E_T for the detector.

The cross section σ can be obtained by first computing the dark matter particle-quark interaction and then convoluting with the hadronic matrix elements describing the nucleon content in quarks and gluons (which leads to large uncertainties).

This cross section σ can be separated into spin-dependent and spin-independent components

$$\frac{d\sigma}{dE_R} = \frac{d\sigma_{SD}}{dE_R} + \frac{d\sigma_{SI}}{dE_R}, \quad (5.21)$$

so that the final cross section can be calculated by adding both contributions,

$$\frac{d\sigma}{dE_R} = \frac{m}{2\mu^2 v^2} (\sigma_0^{SD} F_{SD}^2(E_R) + \sigma_0^{SI} F_{SI}^2(E_R)), \quad (5.22)$$

with the form factor $F(E_R)$ includes the dependence on the momentum transfer $q := \sqrt{2mE_R}$, and σ_0 is the cross section at zero momentum transfer.

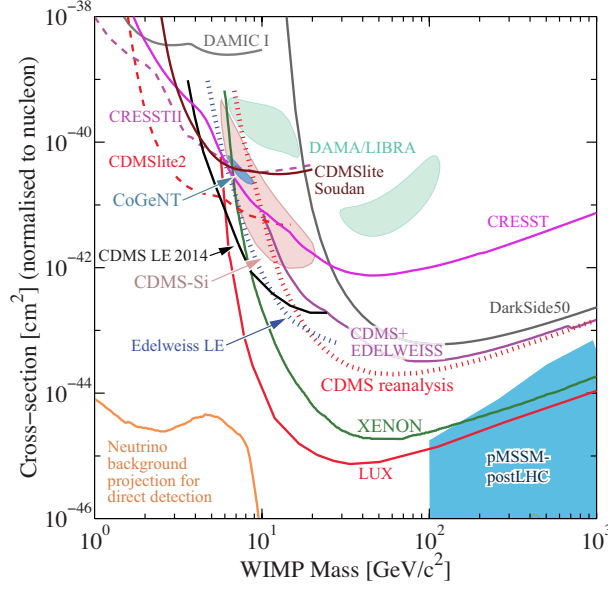


Figure 5.5: Dark matter spin independent cross sections as a function of the dark matter candidate [4]. The relevant experiments are indicated in the captions.

The spin-dependent contribution is given by the axial-vector couplings,

$$\mathcal{L} \supset \alpha_S \bar{\chi} \chi \bar{q} q + \alpha_V \bar{\chi} \gamma_\mu \chi \bar{q} \gamma^\mu q, \quad (5.23)$$

whereas the spin-independent contribution arises from the scalar and vector couplings

$$\mathcal{L} \supset \alpha_A (\bar{\chi} \gamma^\mu \gamma_5 \chi) (\bar{q} \gamma_\mu \gamma_5 q). \quad (5.24)$$

5.4.2 Indirect detection

Indirect detection experiments focus on detecting byproduct particles produced by annihilation or decay of dark matter particles. Arguably the most interesting case is the emission of gamma rays, since they travel in straight lines and are not strongly absorbed in the local universe.

The annihilation rate in a given direction with angle ϕ with respect to the galactic center can be obtained as [108]

$$\Phi_\gamma \approx (0.94 \times 10^{-13} \text{ cm}^{-5} \text{ sr}^{-1}) N_\gamma \sigma v \left(\frac{100 \text{ GeV}}{m} \right)^2 J(\phi), \quad (5.25)$$

where we have defined

$$J(\phi) := \frac{1}{8.5 \text{ kpc}} \left(\frac{1}{0.3 \text{ GeV cm}^{-3}} \right)^2 \int_{\mathcal{L}} \rho^2(l) dl(\phi), \quad (5.26)$$

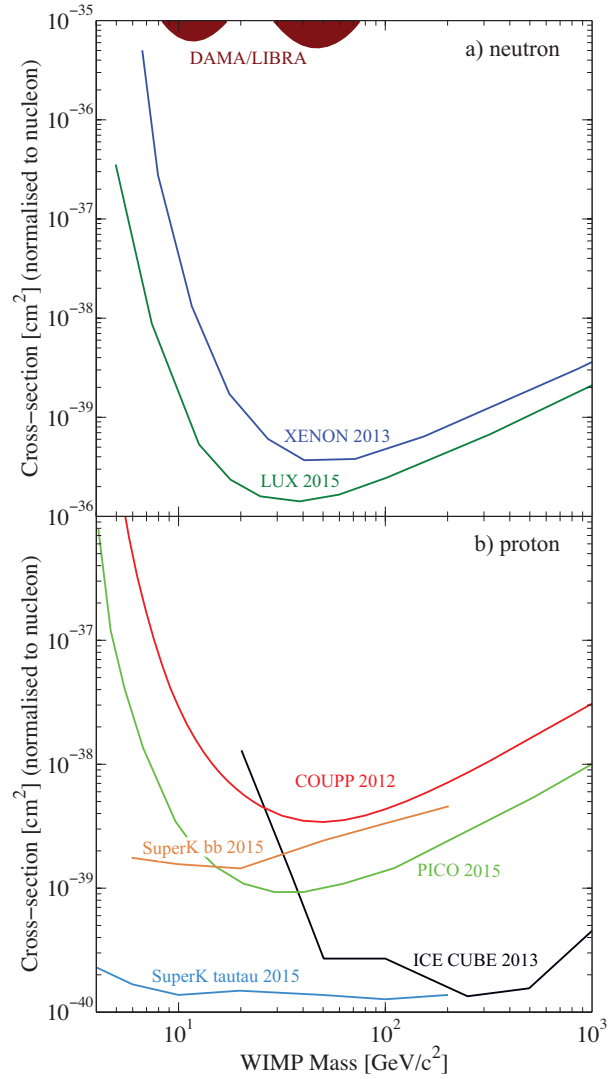


Figure 5.6: Dark matter WIMP cross sections for spin-dependent couplings as a function of the dark matter candidate mass for interactions with neutron (top) or proton (bottom) [4]. The relevant experiments are indicated in the captions.

where \mathcal{L} represents the line of sight, and $\rho(l)$ the dark matter density along \mathcal{L} .

There are of course several possible sources of gamma rays in the universe, so it is important to understand the features of emission due to dark matter. There are basically two types of gamma ray emission due to dark matter annihilation. When the dark matter particle decays into quarks and gauge bosons (with later hadronization and ion decays) we observe a continuum spectrum, as opposed to direct annihilation to gamma rays which gives rise to characteristic spectral features difficult to explain by other means [109]. In any case these signals must be compared to predictions of other astrophysical gamma sources (like common power laws or exponential cut-offs typical of pulsars). Together with spatial information this can be used to identify dark matter sources [110]. (For example more spherical emission is expected from dark matter halos instead of conventional diffuse emission, and square density dependence of dark matter sources contrasts with linear density dependence of conventional gamma ray flux [111, 112]).

Different experiments observe different energy ranges of gamma ray emissions. In the range 100 MeV–100 GeV pair-conversion telescopes of satellites like the Fermi Large Area Telescope (Fermi-LAT) are used. Above 100 GeV Cherenkov telescopes (HESS, MAGIC, VERITAS) are more sensitive. There are some tradeoffs between the two alternatives: Satellite experiments have smaller effective areas, but are basically background free, whereas experiments on Earth have smaller field of views, and are typically used for dark matter only a relatively small fraction of the time (around 10%) [109]. Some constraints from gamma ray detectors are shown in Fig. 5.7.

Gamma rays are not the only possible cosmic rays which may originate from dark matter interactions. Neutrinos and charged rays are also object of intensive study. In the case of neutrinos, they can be used to probe for dark matter annihilation similarly to gamma rays, but its most interesting contribution is from the scattering of dark matter particles by hydrogen in the Sun, which is very sensitive to the spin-dependent contribution. The experiments IceCube and ANTARES are the most prominent example of such searches. Some results from IceCube are shown in Fig. 5.7. For annihilation current limits by neutrino telescopes are only competitive for very high dark matter particle masses, but for the spin-dependent contribution of the dark matter particle-nucleon interaction they currently hold state-of-the-art results [109].

With respect to charged cosmic rays, the most prominent signature are the anti-proton and positron channels, since antiparticles are rarely produced in secondary processes what allows a good detectable signal for dark matter annihilation. The main experiments for this signals are PAMELA and AMS.

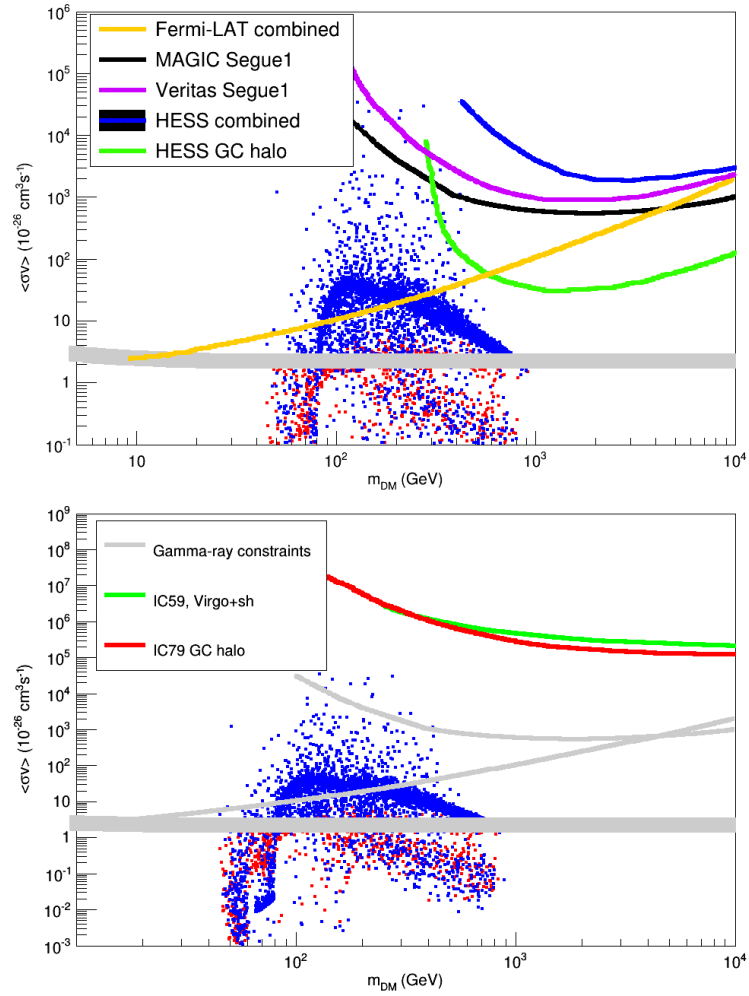


Figure 5.7: (Top) Current indirect detection constraints on averaged cross section vs. dark matter mass from Fermi-LAT, HESS dwarf galaxies and halo, VERITAS and MAGIC. (Bottom) Constraints on annihilation cross section vs. dark matter mass obtained by neutrino telescope IceCube Virgo cluster and the multipole analysis of the halo 79. From [109].

5.4.3 Collider searches

As we have seen, all present-day information we have about dark matter is obtained from gravitational sources at cosmological scales. This includes the overall dark matter density in the universe, as well as information about its density distribution at the galaxy level. Measurements at the particle level are however of vital importance. In particle physics, mass and coupling measurements are necessary to deeply understand its behavior and how it fits together with the rest of the particles in the various models, and ultimately unveil its nature. Also, astrophysical measurements depend crucially on the mass of the dark matter candidate as well as on the relevant cross section, be it the scattering cross section for direct detection or annihilation cross section for indirect detection experiments.

Chapter 6

Neutrino masses

It is by now well established experimentally that neutrinos must have nonzero mass and mixing [4]. In this chapter we will review the evidence for neutrino masses, why the Standard Model does not allow for such masses and the theoretical possibilities to extend the Standard Model to include them. First we will review some of the evidence for nonzero neutrino masses in 6.1, in 6.2 we will review the theoretical conditions to accommodate nonzero neutrino masses, and will focus on the Majorana case in 6.3. We will then investigate mechanisms to generate Majorana masses in beyond the standard model theories in the seesaw mechanism in 6.4 as well as in radiative seesaw variants in 6.5. Finally we will close the chapter by analyzing the lepton flavor violation consequences of these type of models 6.6.

6.1 Evidence for neutrino masses

Oscillations are an experimental consequence of neutrino flavor mixing, requiring nonzero neutrino masses. We can see this by taking a neutrino of a given flavor (say, produced by an electroweak process involving a given lepton flavor), and expressing it as a combination of mass eigenstates,

$$\nu_{lL}(x) = \sum_j U_{lj} \nu_{jL}, \quad (6.1)$$

for l one of e, μ, τ . The matrix U is a unitary matrix known as the Pontecorvo-Kami-Nakagawa-Sakata, or PMNS matrix for short.

So far all neutrino oscillation data can be described by three flavors, and data on Z invisible decay width is only compatible with three light flavors coupling to Z [4]. This does not rule out the possibility of heavier or sterile neutrinos that can in general mix with the known neutrinos.

Another crucial neutrino issue is that of its nature. Being electrically neutral, massive neutrinos can be either Dirac or Majorana particles [113]. In the Dirac case some lepton charge, usually the total lepton charge L must

be conserved, and the neutrino ν and antineutrino $\bar{\nu}$ will be distinguished by its number L , whereas in the Majorana case, no lepton charge is conserved and the neutrino ν and antineutrino $\bar{\nu}$ would be the same particle. We will mainly focus on the Majorana case throughout this chapter.

In the case of three light neutrinos the neutrino PMNS matrix can be parametrized by three angles and one CP violation phase for Dirac or three CP violation phases for Majorana neutrinos [114],

$$U = VP \quad (6.2)$$

with

$$V = \begin{pmatrix} c_{12}c_{13} & s_{12}c_{13} & s_{13}e^{-i\delta} \\ -s_{12}c_{23} - c_{12}s_{23}s_{13}e^{i\delta} & c_{12}c_{23} - s_{12}s_{23}s_{13}e^{i\delta} & s_{23}c_{13} \\ s_{12}s_{23} - c_{12}c_{23}s_{13}e^{i\delta} & -c_{12}s_{23} - s_{12}c_{23}s_{13}e^{i\delta} & c_{23}c_{13} \end{pmatrix}, \quad (6.3)$$

where $c_{ij} = \cos \theta_{ij}$ and $s_{ij} = \sin \theta_{ij}$, and

$$P = \text{diag}(1, e^{i\alpha_{21}/2}, e^{i\alpha_{31}/2}), \quad (6.4)$$

with α_{21}, α_{31} the two extra CP violation phases in the Majorana case.

The amplitude of the probability to observe a neutrino $\nu_{l'}$ if a neutrino ν_l was produced after a time T and a distance L can be written as [115]

$$A(\nu_l \rightarrow \nu_{l'}) = \sum_j U_{l'j} D_j U_{jl}^\dagger \quad (6.5)$$

, where D_j described the propagation of the neutrino between the source and the detection point, and can be found using relativistic quantum mechanics to be

$$D_j = e^{-i(E_j T - p_j L)}, \quad (6.6)$$

and the associated probability is then

$$P(\nu_l \rightarrow \nu_{l'}) = |A(\nu_l \rightarrow \nu_{l'})|^2. \quad (6.7)$$

The relevant quantity for the calculation of (6.7) is

$$\delta\phi_{jk} = (E_j - E_k)T - (p_j - p_k)L, \quad (6.8)$$

which after some considerations (see, e.g., [4]) can be shown to be

$$\delta\phi_{jk} \approx \frac{m_j^2 - m_k^2}{2p} L, \quad (6.9)$$

for $p = (p_j + p_k)/2$. This phase difference $\delta\phi_{jk}$ is a Lorentz invariant.

This computation assumes a plane wave propagation, and a wave packet description introduces some conditions, most importantly the condition of

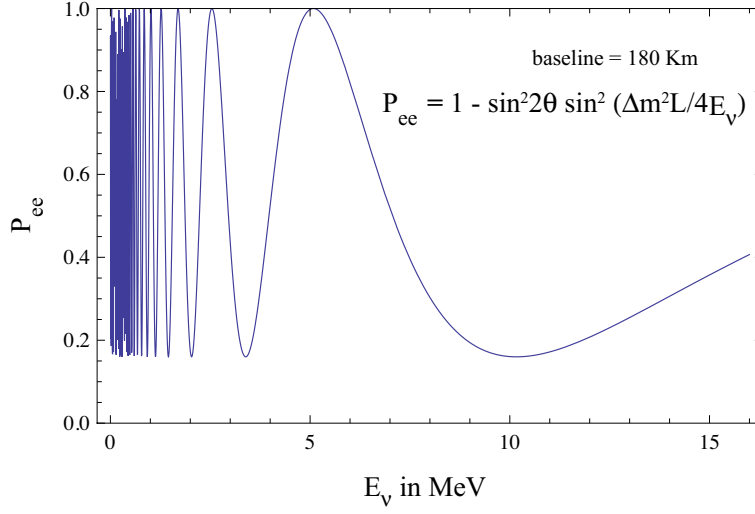


Figure 6.1: Example of neutrino oscillations as a function of the energy of the neutrino for a baseline of 180 km [116].

overlapping of the wave packets for the different flavors at the detection point.

From eqs. (6.5), (6.6) and (6.9) we obtain the oscillation probabilities

$$P(\nu_l \rightarrow \nu'_l) = \sum_j |U_{\nu'_j}|^2 |U_{lj}|^2 + 2 \sum_{j>k} |U_{\nu'_j} U_{l'_j}^* U_{lk} U_{l'_k}^*| \cos \left(\frac{\Delta m_{jk}}{2p} L - \phi_{l'l;jk} \right), \quad (6.10)$$

for neutrinos and

$$P(\bar{\nu}_l \rightarrow \bar{\nu}'_l) = \sum_j |U_{\nu'_j}|^2 |U_{lj}|^2 + 2 \sum_{j>k} |U_{\nu'_j} U_{l'_j}^* U_{lk} U_{l'_k}^*| \cos \left(\frac{\Delta m_{jk}}{2p} L - \phi_{l'l;jk} \right), \quad (6.11)$$

where l, l' represent e, μ, τ and $\phi_{l'l;jk} = \arg \left(U_{\nu'_j} U_{l'_j}^* U_{lk} U_{l'_k}^* \right)$.

We see from eq. (6.5) that to have nonzero neutrino oscillations, at least two neutrinos should have different masses and $U \neq 1$, i.e., there should be lepton mixing. For the mixing effects to be large, the neutrino oscillation length L_{jk}^ν for $j \neq k$ should be of the order or, of smaller than the source-detector distance L , so that there is enough time for neutrinos to oscillate before reaching the detector, in particular,

$$\frac{|\Delta m_{jk}^2|}{2p} L = 2\pi \frac{L}{L_{jk}^\nu} \gtrsim 1, \quad j \neq k. \quad (6.12)$$

It can be easily seen from eqs. (6.10) and (6.11) that $P(\nu_l \rightarrow \nu'_l) = P(\bar{\nu}_{l'} \rightarrow \bar{\nu}_l)$, which is a consequence of CPT invariance. For CP invariance

we have $P(\nu_l \rightarrow \nu_{l'}) = P(\bar{\nu}_l \rightarrow \bar{\nu}_{l'})$, and for T invariance $P(\nu_l \rightarrow \nu_{l'}) = P(\nu_{l'} \rightarrow \nu_l)$, $P(\bar{\nu}_l \rightarrow \bar{\nu}_{l'}) = P(\bar{\nu}_{l'} \rightarrow \bar{\nu}_l)$. It can be seen from eqs. (6.10) and (6.11) that CP violation can only occur if $\phi_{l'l';jk} \neq \pi q$ for $q = 0, 1, 2$, which is only possible if $U_{l'j}U_{lj}^*U_{lk}U_{l'k}^* \in \mathbb{C} \setminus \mathbb{R}$. From what we have seen, To measure CP and T violation in neutrino oscillations we can consider the following asymmetries

$$A_{\text{CP}}^{\prime l} := P(\nu_l \rightarrow \nu_{l'}) - P(\bar{\nu}_l \rightarrow \bar{\nu}_{l'}), \quad (6.13)$$

and

$$A_{\text{T}}^{\prime l} := P(\nu_l \rightarrow \nu_{l'}) - P(\nu_{l'} \rightarrow \nu_l), \quad (6.14)$$

and we can actually compute from eqs. (6.10) and (6.11) in the case of CP violation

$$A_{\text{CP}}^{\prime l} = 4 \sum_{j>k} \Im(U_{l'j}U_{lj}^*U_{lk}U_{l'k}^*) \sin\left(\frac{\Delta m_{jk}}{2p}L\right) \quad (6.15)$$

If we consider mixing of the three neutrinos with $0 < \Delta_{21}^2 < |\Delta_{31(32)}^2|$ and $|U_{e3}|^2 = |\sin\theta_{13}|^2 \ll 1$, then Δ_{21}^2 and θ_{12} are the parameters associated with solar ν_e oscillations, and Δ_{31}^2 , θ_{12} and θ_{23} are associated with the atmospheric ν_μ oscillations. Thus, θ_{12} and θ_{23} are denoted solar and atmospheric neutrino mixing angles and sometimes noted as $\theta_{12} = \theta_\odot$ and $\theta_{23} = \theta_A$ and similarly Δ_{21}^2 and Δ_{31}^2 are referred to as solar and atmospheric neutrino mass squared differences and noted as Δ_\odot^2 and Δ_A respectively.

Neutrino oscillations have been shown to exist by experiments involving solar, atmospheric, reactor and accelerator neutrinos.

Neutrino oscillation experiments are classified by the average energy of the neutrinos detected \bar{E} and the source-detector distance L . As we have seen, the requirement $L_{jk}^\nu \lesssim 2\pi L$ determines the minimal values of squared mass differences Δm^2 that can be measured, $\min(\Delta m^2) \sim 2\bar{E}/L$. In general, this value is relatively small.

Table 6.1: Current best fits for neutrino mixing parameters. From [4].

Parameter	Best fit ($\pm 1\sigma$)
Δm_{21}^2 [10^{-5} eV ²]	$7.54_{-0.22}^{+0.26}$
$ \Delta m_{21}^2 $ [10^{-3} eV ²]	2.43 ± 0.06 (2.38 ± 0.06)
$\sin^2 \theta_{12}$	0.308 ± 0.017
$\sin^2 \theta_{23}, \Delta m^2 > 0$	$0.437_{-0.023}^{+0.033}$
$\sin^2 \theta_{23}, \Delta m^2 < 0$	$0.455_{-0.031}^{+0.039}$
$\sin^2 \theta_{13}, \Delta m^2 > 0$	$0.0234_{-0.0019}^{+0.0020}$
$\sin^2 \theta_{13}, \Delta m^2 < 0$	$0.0240_{-0.0022}^{+0.0019}$

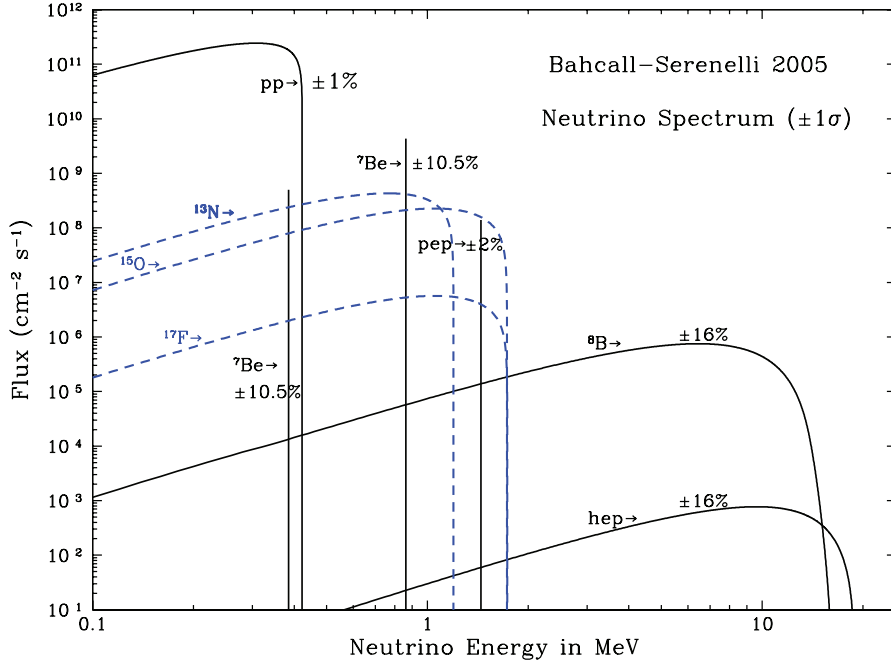


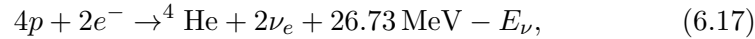
Figure 6.2: Solar neutrino energy spectrum in the standard solar model [117].

6.1.1 Solar neutrino experiments

We can write the reactions by which Solar neutrinos are produced as



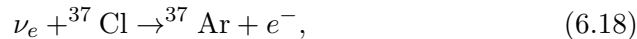
which after positron annihilation and considering the solar thermal energy gives rise to



where E_ν represents the energy of the neutrinos, with an average value of \bar{E}_ν 0.6 MeV.

One needs a model of the sun to predict the fluxes of the neutrino emissions of the sun. As more information has been obtained and better theoretical models have been developed, these predictions have been updated. In particular we show in 6.2 the predictions of one of these models. In any way, since the first solar electron neutrino observations, it has been significant that the flux was smaller than predicted by theoretical models, as we will now discuss.

One of the first experiments to observe was Homestake based of a method by Pontecorvo [118], and which consists on the neutrino interaction on ${}^{37}\text{Cl}$ as follows



where the argon atoms which are produced are radioactive and can be collected and measured for several times its half-life so as to measure its signal.

As we have already said, it was already apparent a mismatch between predicted neutrino fluxes and the measurement, giving raise to the solar neutrino problem. Also later other experiments like GALLEX and GNO at Grand Sasso, or SAGE in Russia confirmed these results.

Later the Kamiokande experiment in Japan was able to perform real-time measurements through νe scattering,

$$\nu_x + e^- \rightarrow \nu_x + e^- \quad (6.19)$$

in a water Cherenkov detector. This experiment is directional, and can therefore drastically reduce the background by taking advantage of the correlation between the angles of the neutrino and the recoil electron, and guaranteeing also that the electrons came from the direction of the sun. This was later followed by the Super-Kamiokande experiment [119] which improved its statistics. It is important to note that this experiment is in principle sensitive to all neutrino flavors, but has a much higher sensitivity to ν_e .

6.2 Majorana neutrinos and the Weinberg operator

In the SM there are in principle no right-handed neutrinos ν_R , and therefore the only possible neutrino mass term is of Majorana type. However, the combination $\bar{\nu}_L^c \nu_L$ is clearly an SU(2) triplet, so a higher-dimensional term is needed to generate masses. With the SM particle content the least-dimensional term that can generate Majorana neutrino masses after EWSB is the is unique $d = 5$ Weinberg operator [120],

$$\delta L = \frac{1}{2} \frac{K_{\alpha\beta}^5}{\Lambda} (\bar{L}_\alpha \tilde{H}^*) (\tilde{H}^\dagger L_\beta) + \text{h.c.}, \quad (6.20)$$

where α, β are the families, and Λ is the new-physics scale. This operator is nonrenormalizable as can be seen from its dimensionality. It can be seen as an effective operator of seesaw, or a one-loop [121].

6.3 Majorana masses

We will briefly review a couple of important aspects of massive Majorana fermions, since we will require them to study massive Majorana neutrinos. There are of course theories of massive Dirac neutrinos, but we will not study those cases here.

The Lagrangian for a massive Majorana particle is given by

$$\mathcal{L} = \frac{i}{2}\bar{\chi}\not{\partial}\chi - \frac{1}{2}m\bar{\chi}\chi, \quad (6.21)$$

where we assume $m \in \mathbb{R}$. We can decompose the Majorana field into two chiral spinors

$$\chi = e^{i\alpha}\psi_L + e^{i\beta}\psi_L^c, \quad (6.22)$$

in such a way that the Majorana field satisfies the extended Majorana condition

$$\chi^c = e^{-(\alpha+\beta)}\chi. \quad (6.23)$$

In this way the mass term is given by

$$\mathcal{L} \sim -\frac{m}{2}\left(e^{-i(\alpha-\beta)}\bar{\psi}_L\psi_L^c + e^{-i(\alpha-\beta)}\bar{\psi}_L^c\psi_L\right). \quad (6.24)$$

By defining $M := me^{i(\alpha-\beta)}$, we obtain

$$\mathcal{L} \sim -\frac{M}{2}\bar{\psi}_L^c\psi_L + \text{h.c.} \quad (6.25)$$

This term obviously breaks lepton number. Also, the mass M is at this point complex, but the phase can be absorbed in the ψ_L field. This motivates the next section.

As we have seen, the Majorana mass matrix is constructed in principle with complex values. A naive diagonalization of a Majorana mass matrix using the common eigenvalue decomposition can lead to negative masses. (The matrix is still Hermitian and so the eigenvalues are still real.) The reason is that the Majorana condition possesses a degree of freedom which has to be exploited to obtain physically-sensible values for the mass by redefinition of the fields (ψ_L in the previous section). The diagonalization in this case can be done by using the Takagi decomposition [122], which is in fact a particular case of the well-known Singular Value Decomposition. We will review this diagonalization method and analyze its physical significance.

Firstly, we should recall the traditional eigenvalue decomposition. It is well known that for every nonsingular matrix $M \in \mathbb{C}^{n \times n}$ there exists a matrix U such that

$$UMU^{-1} = \text{diag}(m_1, \dots, m_n), \quad (6.26)$$

where m_i are the eigenvalues of M . It can also be easily seen that $M = M^\dagger \implies U^{-1} = U^\dagger$, $m_n \in \mathbb{R}$, and that $M = M^T \implies U^{-1} = U^T$.

The Singular Value Decomposition, unlike the eigenvalue decomposition, can be applied to any arbitrary matrix $M \in \mathbb{C}^{m \times n}$ (also nonsquare and singular matrices). For any such matrix, it can be shown that there exist $V \in \mathbb{C}^{\min(m,n) \times m}$ and $W^{-1} = W^\dagger \in \mathbb{C}^{n \times \min(m,n)}$ such that

$$V^*MW^\dagger = \text{diag}(m_1, \dots, m_{\min(m,n)}), \quad (6.27)$$

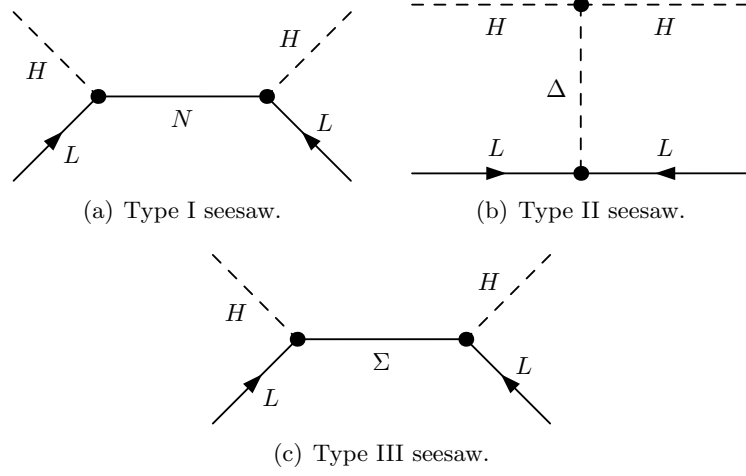


Figure 6.3: The three tree level realizations of the Weinberg operator, corresponding to the three seesaw mechanisms.

with $m_i \geq 0, \forall i \in (1, \dots, \min(m, n))$.

In the case of a symmetric matrix $M = M^T \in \mathbb{C}^{n \times n}$, it can be shown that there exists a matrix $U \in \mathbb{C}^{n \times n}$ such that $U^{-1} = U^\dagger$ and

$$U^* M U^\dagger = \text{diag}(m_1, \dots, m_n) \quad (6.28)$$

with $m_i \geq 0, \forall i$. This is the so-called Takagi decomposition.

Although very similar to the eigenvalue decomposition, the Takagi decomposition is actually a particular case of a Singular Value Decomposition where $V = W^*$. In particular, it should be noted that in general U^* is not necessarily the inverse of U^\dagger .

Physically, this corresponds to a redefinition of the fields (through the mixing matrices). In particular, those fields with negative masses can be redefined as $\xi \rightarrow i\gamma_5 \xi$, or equivalently, $\xi_{R(L)} \rightarrow \pm i \xi_{R(L)}$.

6.4 Seesaw and inverse seesaw models

The simplest way to generate the effective term in Eq. (6.20) in a renormalizable framework is arguably the seesaw mechanism, in which the Weinberg operator is realized as an effective term which is the result of integrating out a heavy field in a tree-level process. It can be seen that there are three and only three ways to obtain the effective term (6.20) at tree-level (see, e.g., Ref. [123]).

In the so-called Type-I seesaw [124], we assume the existence of an $SU(2)$ singlet ν_R and a mass term of the form

$$\delta\mathcal{L} = f \bar{\nu}_R \nu_L \langle \phi^0 \rangle + \frac{M}{2} \bar{\nu}_R^c \nu_R + \text{h.c.} \quad (6.29)$$

By the Takagi diagonalization of the mass matrix for (ν_L, ν_R) ,

$$\begin{pmatrix} 0 & m \\ m & M \end{pmatrix} \quad (6.30)$$

the Dirac mass term in Eq. (6.29) induces a mass

$$m_{\nu_L} \simeq \frac{m^2}{M} \quad (6.31)$$

for the left-handed neutrino. Another way to see this is to look at the process in Fig. 6.3(a) and integrate out the highly massive ν_R . The smallness of the neutrino mass thus in this case arises naturally associated to the large new scale M .

In the Type-II seesaw [125, 126, 127, 128, 129, 130], which we can see in Fig. 6.3(b), we alternatively introduce an SU(2) triplet scalar χ . The lagrangian in this case would be

$$\delta\mathcal{L} = \frac{1}{2}H\bar{L}^cL\chi + \lambda M\phi\phi\chi + M^2\chi^*\chi + \text{h.c.} \quad (6.32)$$

By integrating out χ the effective term would be

$$\delta\mathcal{L}_{\text{eff}} = \frac{h\lambda}{2M}\phi\phi\bar{L}^cL. \quad (6.33)$$

A last option, known as Type-III seesaw [131], is to introduce a fermionic SU(2) triplet Σ to couple to the SU(2), which leads to

$$YH\bar{L}^c\Sigma + \frac{M}{2}\bar{\Sigma}^c\Sigma. \quad (6.34)$$

By integrating out the heavy Σ in diagram Fig. 6.3(c) we obtain an effective (6.20) term.

In the seesaw models we have seen, the masses of the neutrinos are of the order $m_\nu \sim v^2/\Lambda$. For $\mathcal{O}(1)$ couplings and the current limits on the neutrino masses, this means that the new scale Λ is close to the Planck scale and in any case far out of reach of current (and future) colliders.

Models with an accessible new physics scale require a suppression mechanism for neutrino mass. We will present in the next sections two examples of these mechanisms, namely the inverse seesaw and the radiative seesaw models. It is also possible that the operator in (6.20) is forbidden or suppressed by a yet unknown mechanism and therefore higher dimensional effective operators are required, but we will not study that possibility here.

We will also briefly mention the inverse seesaw model [132] as an alternative to the radiative seesaw models we will study later.

In the inverse seesaw the mechanism that suppresses the neutrino mass is the small amount of lepton number violation and not a large energy scale.

The model contains right-handed neutrinos as well as the corresponding number of singlets S_i which couple in a lepton-number conserving way. A suppression mechanism for the right-handed neutrino Majorana mass term must be supposed (e.g., some additional symmetry). In this way, the lepton-number violation comes from the singlet Majorana mass term,

$$\mathcal{L} \sim Y \bar{L} \tilde{H} \nu_R + m_R \bar{S}^c \nu_R + \frac{1}{2} m_S \bar{S}^c S + \text{h.c.} \quad (6.35)$$

The mass matrix is therefore

$$M = \begin{pmatrix} 0 & m_R \\ m_R^T & m_S \end{pmatrix}, \quad (6.36)$$

which for $M_S \ll M_R$ gives rise to two heavy Majorana neutrinos with similar masses (difference $\sim m_S$). By integrating out these heavy particles at tree level (with the same diagram as in Type-I seesaw) gives a neutrino mass matrix

$$M_\nu = v^2 Y^2 M_R^{-1} M_S (M_R^{-1})^T. \quad (6.37)$$

Comparing this to the normal seesaw mechanism, we see that $m_\nu \propto Y^2 M_S M_R^{-1}$ instead of $m_\nu \propto Y^2$, and therefore a small $M_S M_R^{-1}$ acts as a suppression mechanism.

6.5 Radiative seesaw models

It is also possible to generate the operator (6.20) via loop diagrams. In this way, the neutrino mass is naturally suppressed by the loop integrals entering the diagram. A systematic study of all 1-loop scenarios can be found in [121]. We will briefly review the canonical Zee model [133].

In the Zee model, we introduce a scalar field $S \sim (1, -1)$ to break lepton number,

$$\mathcal{L} \sim \kappa \bar{L}_i^c L_j S^* + \text{h.c.} \quad (6.38)$$

and at least a second Higgs doublet, so that in the Higgs sector we obtain a term of the form

$$\mathcal{L} \sim \lambda H_i H_j S + \text{h.c.} \quad (6.39)$$

From (6.38) and (6.39), lepton number is broken by two units and a Majorana mass term is induced from the diagram in Fig. 6.3(a),

$$m_{ij} = \frac{1}{16\pi^2} \kappa (m_j^2 - m_i^2) \lambda_{12} \frac{v_2}{v_1} \frac{1}{m_S^2 - m_h^2} \log \frac{m_S^2}{m_h^2} \quad (6.40)$$

where $m_i = m_{l_i}$. A mixing term is induced from (6.39) between S and h_\pm^\dagger . If we assume $\lambda \sim m_h$, $m_S \gg m_h$, $v_1 \simeq v_2$, then the neutrino mass matrix is found to be

$$m_{ij} \sim \frac{1}{16\pi^2} \kappa m_h \frac{m_j^2 - m_i^2}{m_S^2}. \quad (6.41)$$

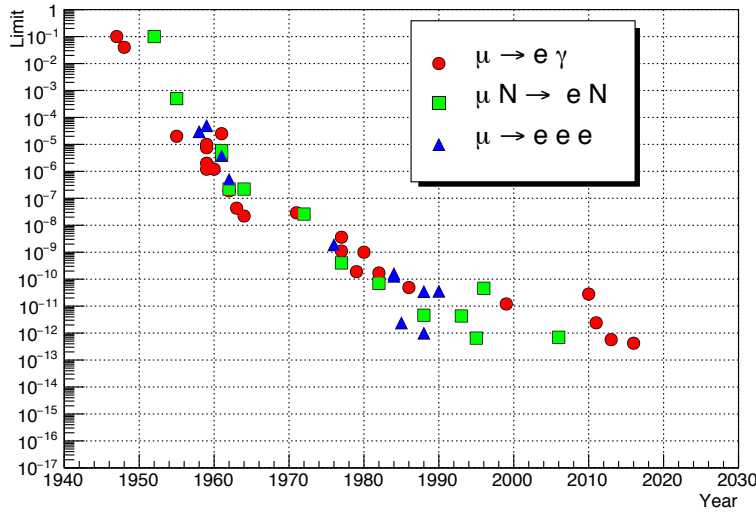


Figure 6.4: Best lepton flavor violation constraints by year. Initially the best constraints are those from cosmic ray muons, later from stopped pion beams, and more recently from stopped muon beams, corresponding to the three clusters in the image. Current constraints are set by MEG [134]. From [135].

6.6 Lepton flavor violation processes

A concept distinct from but closely related to neutrino masses is that of lepton flavor violation [136]. Lepton flavor is necessarily violated to generate neutrino masses as we have seen in eq. (6.25). (Although neutrino masses is not the only meaningful way to break lepton number, see e.g. [137].) However lepton flavor has never been observed violated despite the considerable experimental efforts and has been severely constrained by ever-improving experiments (see fig. 6.4). The current best limits are set by constraints on the muonic channels $\text{BR}(\mu \rightarrow e\gamma)$ and $\text{BR}(\mu \rightarrow 3e)$, as we will review in Ch. 8. The former is usually evaluated in the form of $\mu^+ \rightarrow e^+\gamma$. The reason for this is that obviously the cross sections for π^+ are larger from proton collisions than for π^- , but more importantly muon capture, i.e. the fact that muons captured in the nucleus typically lead to ejection of nucleons and photons producing accidental rates in the detector [135]. Trivial Dirac masses in the SM lead to unobservables rates of $\text{BR}(\mu \rightarrow e\gamma) \sim \mathcal{O}(10^{-54})$ which makes this process a great beyond the standard model physics probe [138]. It is also important to mention the $\text{BR}(\mu \rightarrow 3e)$ which also has competitive limits as we will review.

Another of the promising channels to probe lepton flavor violation is muonic atoms, $1s$ bound states with a μ^- stopped in the target. The muon then decays either through SM channels or new physics lepton-flavor-

violating processes. A typical process is the $\mu - e$ conversion, $\mu^- + (A, Z) \rightarrow e^- + (A, Z)$. The rate for this process typically increases with the atomic number and is maximum around $30 \leq Z \leq 60$ [139]. The signature for this process is a monoenergetic electron with energy of ~ 100 GeV (the particular value is target-dependent) easily detectable and therefore a very good experimental channel. The tightest constraints come from CR($\mu - e, Ti$) [4]. We will review this and other channels in Ch. 8.

Chapter 7

Minimal models

*Frustra fit per plura quod potest fieri per pauciora.*¹

— William of Ockham, *Summa Totius Logicae*.

As we have seen in previous chapter, neutrino masses and dark matter are the most important issues of the electroweak sector of the standard model. Thus, it seems motivated to attempt to find models that combine the solutions to both problems extending the standard model minimally. In this chapter we will present the theoretical developments for a minimal model of neutrino masses with dark matter candidates that will be later investigated numerically.

We will first review in 7.1 previous minimal models in the literature for neutrino masses to establish the context for the model we will study. We will then in 7.2 precisely define this model mathematically and explore its particle content and symmetries. Finally we will investigate its phenomenology in 7.3 from a theoretical point of view, as well as analyze the limits of the computation from the self-energy of the dark matter candidate mass. Numerical results are deferred to a later chapter.

7.1 Introduction and review of current minimal models

One of the first (and simplest) models that can explain neutrino masses and its smallness is the Zee model [133]. This model proposes the extension of the SM with a single scalar field h and two Higgs boson doublets Φ_1, Φ_2 . The singlet h then couples to the leptons on one side as well to the Higgs doublets. Of the Higgs doublets only Φ_1 couples to the leptons. This can

¹It is futile to do with more things that which can be done with fewer.

be seen from the lagrangian

$$\mathcal{L} \supset f Li\tau_2 Lh + m_{12}\Phi_1 i\tau_2 \Phi_2 h^\dagger + \frac{m_l}{\langle \Phi_1 \rangle} \bar{L}\Phi_1 l_R + \text{h.c.}, \quad (7.1)$$

where $m_{12} = -m_{21}$ is a real mass parameter, f is an antisymmetric coupling. The neutrino obtains its mass at one loop.

The mass patterns of the Zee model are very distinctive and well studied [140]. If the couplings f do not have a strong hierarchy, the two heavy neutrinos ν_2, ν_3 are very degenerate and mix almost maximally to give ν_μ, ν_τ . The neutrino ν_1 is therefore almost ν_e with a much smaller mass $m_1 \ll m_2 \sim m_3$.

Given that apart from neutrino masses the the other main issue of the electroweak sector of the standard model is dark matter, this led to the study of neutrino masses in combination with dark matter. The initial Zee model was also analyzed in the context of dark matter [141], and especially later some models were proposed that combined the explanation for neutrino masses with dark matter candidates [142, 143], but especially relevant is that of Ma [144], where the standard model is extended with three singlet fermions N_i and a scalar doublet η , all Z_2 -odd. The Yukawa interactions are then given by

$$\mathcal{L} \supset f(\phi^- \nu + \bar{\phi}^0 l)l^c + h(\nu\eta^0 - l\eta^+)N + \text{h.c.}, \quad (7.2)$$

where we have suppressed some indices for clarity. In this model neutrinos obtain Majorana masses through a one-loop radiative seesaw mechanism, and the dark matter candidate is the lightest of η^0 or N_1 .

The one-loop mass generation of the Zee and Ma models can actually be understood as a particular case in a general study of the one-loop Weinberg operator realizations, and all such models have been classified [121]. Furthermore, of these, the possibilities that naturally contain dark matter candidates have also been systematically classified [145]. We will use these classifications to contextualize the studied model in the next sections.

7.2 Definition of the model

The extension of the Standard Model that we studied [146], with respect to the general classification of one-loop neutrino mass models belongs to the T1-iii family [121], and in particular corresponds to the T1-3-A family with $\alpha = 0$ (where setting α sets the hypercharge) in the classification of models with neutrino masses and dark matter [145].

To extend the Standard Model we add a two chiral (i.e., one vector-like) fermionic $SU(2)$ doublets, noted D and D' , one left-handed singlet fermion S , as well as two real scalar singlets ϕ_i . The second scalar singlet is added to guarantee enough degrees of freedom in the neutrino mass generation.

As is usual in this type of models, a Z_2 symmetry is added to the Standard Model gauge group to guarantee the stability of the dark matter candidate. As expected, new fields are odd, whereas Standard Model fields are even under this new Z_2 symmetry. Thus, the charges of the new particles under the $SU(2) \times U(1) \times Z_2$ gauge group are given by

$$D = \begin{pmatrix} \psi \\ E \end{pmatrix} \sim (2, -\frac{1}{2}, -), \quad D' = \begin{pmatrix} -E' \\ \psi' \end{pmatrix} \sim (2, \frac{1}{2}, -), \quad (7.3)$$

in the case of the fermionic doublets, and

$$S \sim (1, 0, -), \quad \phi_i \sim (1, 0, -) \quad (7.4)$$

for the fermion and scalar singlets, respectively. We show the Standard Model electroweak sector charges to fix notations:

$$H = \begin{pmatrix} \phi^+ \\ \phi^- \end{pmatrix} \rightsquigarrow \begin{pmatrix} 0 \\ \frac{1}{\sqrt{2}}(v+h) \end{pmatrix} \sim (2, \frac{1}{2}, +), \quad L_i = \begin{pmatrix} \nu_{iL} \\ e_{iL} \end{pmatrix} \sim (2, -\frac{1}{2}, +), \quad (7.5)$$

where, as usual, H is the Higgs doublet, and L is the lepton doublet, and

$$e_{iR} \sim (1, 1, +) \quad (7.6)$$

for the right-handed electron singlet. The rest of the Standard Model particles also have Z_2 charge +1.

The most general Lagrangian terms that we can add to the Standard Model lagrangian compatible with the symmetries we introduced can be expressed as

$$\mathcal{L} \sim \alpha_{ij} \bar{D}' L_j^c \phi_i - \mu \bar{D}^c D' - \beta \bar{D}^c H S - \beta' \bar{D}' \tilde{H} S^c \quad (7.7)$$

$$- \gamma_{h\phi} H^* H \phi^2 - \gamma_\phi \phi^4 - \frac{1}{2} m_\phi^2 \phi^2 - \frac{1}{2} m_S \bar{S}^c S + \text{h.c.} \quad (7.8)$$

where we define

$$\tilde{H} := i\sigma_2 H. \quad (7.9)$$

The second line of the equation represents the scalar potential, and the first line contains the terms most relevant for the rest of the discussion, which includes a Dirac mass term for the vector-like fermionic doublet, a Majorana mass term for the fermionic singlet, and Yukawa interactions terms for the fermionic singlet and doublet, plus a Yukawa term with the Standard Model lepton doublet. This last interaction term is the most relevant to our discussion since it is what allows for the generation of nonzero neutrino masses.

The scalar fields ϕ do not acquire a vacuum expectation value, and the neutrinos remain massless at tree level. But at one loop a Majorana mass term is generated for the neutrinos. A necessary condition for this is that the Lagrangian must violate lepton number, which we can see as the following: The scalar fields ϕ have naturally lepton number zero, and similarly the Majorana fermionic singlet S . But that being the case, the α and β terms in (7.7) cannot be lepton-number-conserving simultaneously unless $\alpha_{ij} = \beta_k = 0$, in which case neutrino masses will vanish.

Once expanded, the lagrangian includes the mass terms,

$$\mathcal{L}_m = -\mu\bar{\psi}^c\psi' - \mu\bar{E}^cE - \frac{v\beta}{2}\bar{\psi}^cS \quad (7.10)$$

$$- \frac{v\beta'}{2}\bar{\psi}'S^c - \frac{1}{2}m_S\bar{S}^cS - \frac{1}{2}m_\phi\phi^2 + \text{h.c.} \quad (7.11)$$

and the couplings with the Standard Model particles,

$$\mathcal{L}_Y = \alpha_{ij}\bar{\psi}'\nu_{jL}^c\phi_i + \alpha_{ij}\bar{E}'\nu_{eL}^c\phi_i + \frac{\beta}{\sqrt{2}}\bar{\psi}^cSh + \frac{\beta'}{\sqrt{2}}\bar{\psi}'S^ch + \text{h.c.} \quad (7.12)$$

From (7.10) and defining $\Psi := (\psi, \psi', S)$, the mass matrix can be written as

$$m_\Psi = \frac{1}{2} \begin{pmatrix} 0 & \mu & \frac{\beta v}{\sqrt{2}} \\ \mu & 0 & \frac{\beta' v}{\sqrt{2}} \\ \frac{\beta v}{\sqrt{2}} & \frac{\beta' v}{\sqrt{2}} & \frac{1}{2}m_S \end{pmatrix}, \quad (7.13)$$

and the physical particles and its masses are obtained by diagonalization. If we let χ_i be the i -th physical particle and m_i its mass (with $m_i < m_j$ for $i < j$), and ξ the diagonalization (with the negative-mass corrections) matrix,

$$\Psi_i \equiv \xi_{ij}\chi_j, \quad (7.14)$$

we can write the relevant couplings from (7.12) as

$$\alpha_{ij}\bar{\psi}'\nu_{jL}^c\phi_i = \alpha_{ij}\xi_{2k}\bar{\chi}_k\nu_j^c\phi_i. \quad (7.15)$$

7.3 Phenomenology

In this section we will investigate the potential phenomenological signatures that our model can have in order to later constrain its different parameters.

7.3.1 Collider constraints

First of all we notice that apart from the Majorana fermions our particle spectrum contains a charged Dirac fermion with mass μ is is constrained by collider searches to be larger than about 103.5 GeV [4], plus two natural scalars $\phi_{1,2}$.

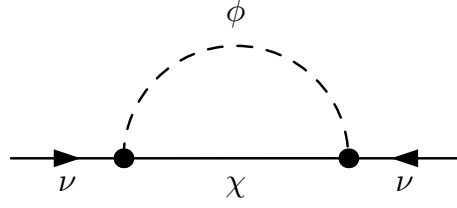


Figure 7.1: Diagram for one-loop radiative neutrino mass generation in our model.

7.3.2 Neutrino masses

Neutrino masses are obtained at one loop through a radiative seesaw mechanism, similar to that of [147]. The main diagram contributing to the neutrino masses is shown in Fig. 7.3 can be computed as

$$M_{ij}^{k,r} = \frac{1}{16\pi^2} \Gamma_{jk}^r \Gamma_{ik}^r m_k \times \left((1 + \Delta) - \frac{m_k^2}{m_k^2 - m_r^2} \log \left(\frac{m_k^2}{\mu^2} \right) + \frac{m_r^2}{m_k^2 - m_r^2} \log \left(\frac{m_r^2}{\mu^2} \right) \right), \quad (7.16)$$

where Γ_{lm}^r is the coupling between ϕ_r , χ_m , and ν_L^c in Fig. 7.3, and which corresponds to the couplings in (7.15), i.e., $\Gamma_{lm}^r := \alpha_{rl} \xi_{2m}$; $\Delta \propto \frac{1}{\epsilon}$, and μ is an arbitrary renormalization constant. (We will see that the results will be independent of μ .)

The neutrino mass matrix element m_{ij}^ν generated by the radiative seesaw mechanism can therefore be computed using (7.16) and (7.15). Taking $\alpha \in \mathbb{R}$ for simplicity of the notation:

$$m_{ij}^\nu = \sum_{k,r} M_{ij}^k = \sum_{k,r} \frac{1}{16\pi^2} m_k \alpha_{ri} \alpha_{rj} \xi_{2k} \xi_{2k} \left(\frac{m_k^2}{m_k^2 - m_r^2} \log \left(\frac{m_k^2}{m_r^2} \right) \right), \quad (7.17)$$

where we have used the fact that

$$\sum_k \xi_{2k} m_k \xi_{k2}^T = (m_\Psi^T)_{22} = 0. \quad (7.18)$$

At this point we notice that the final result is finite and thus independent of the unphysical renormalization factor μ as expected. (This is only true for the sum of all the diagrams, whereas each diagram independently diverges, and thus the μ factor in (7.16).)

In the limit where $\beta, \beta' \ll \mu, m_S$, we can diagonalize (7.13) analytically at leading order in β, β' as

$$\xi = \begin{pmatrix} \frac{i}{\sqrt{2}} & \frac{1}{\sqrt{2}} & \frac{2m_S\beta + 4\mu\beta'}{m_S^2 - 4\mu^2} v \\ -\frac{i}{\sqrt{2}} & \frac{1}{\sqrt{2}} & \frac{2m_S\beta' + 4\mu\beta}{m_S^2 - 4\mu^2} v \\ i \frac{\beta' - \beta}{m_S + 2\mu} \frac{v}{\sqrt{2}} & \frac{\beta + \beta'}{2\mu - m_S} \frac{v}{\sqrt{2}} & 1 \end{pmatrix} + \mathcal{O}(\beta^2) + \mathcal{O}(\beta'^2) + \mathcal{O}(\beta\beta') \quad (7.19)$$

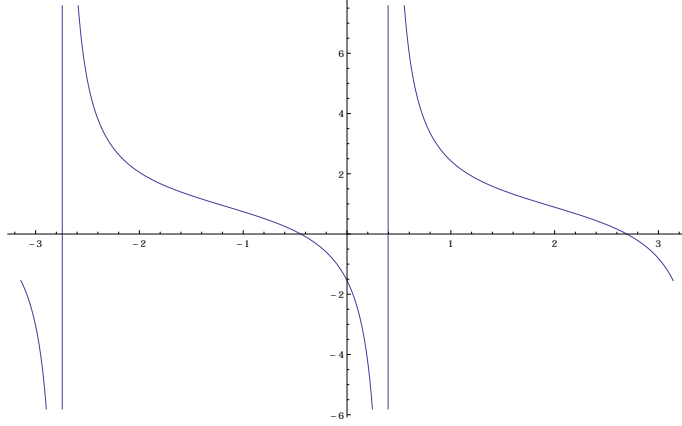


Figure 7.2: Ratio of the α corresponding to τ over the one corresponding to e with respect to the angle θ .

so the neutrino masses (7.17) can be expressed as

$$m_{ij}^\nu = \sum_r \frac{1}{16\pi^2} m_S \alpha_{ri}^2 \left(\frac{2m_S \beta' + 4\mu\beta}{m_S^2 - 4\mu^2} \right)^2 v^2 \left(\frac{m_S^2}{m_S^2 - m_r^2} \log \left(\frac{m_S^2}{m_r^2} \right) \right). \quad (7.20)$$

For the numerical scan we reparametrize the model by using neutrino mixing data [4] instead of α_i as free parameters using a Casas-Ibarra-like reparametrization [148].

First, notice, how (7.17) can be rewritten in the form

$$m_{ij} = \alpha_{ir}^T F_r \alpha_{rj}, \quad (7.21)$$

with

$$F_r = \sum_k \frac{1}{16\pi^2} m_k \xi_{2k} \xi_{2k} \left(\frac{m_k^2}{m_k^2 - m_r^2} \log \left(\frac{m_k^2}{m_r^2} \right) \right), \quad (7.22)$$

With this we can write the coupling matrix α as

$$\alpha = iU^* \sqrt{m} O \sqrt{F^{-1}}, \quad (7.23)$$

where $m = \text{diag}(m_1, m_2, m_3)$, $F = \text{diag}(F_1, F_2)$ and O is a 3×2 matrix such that $OO^T = 1$, which can be expressed as

$$O = \begin{pmatrix} 0 & 0 \\ \cos \theta & \pm \sin \theta \\ -\sin \theta & \pm \cos \theta \end{pmatrix}. \quad (7.24)$$

Because U in our case is given it is easy to see that there will be a relation between the different α values. just by multiplying the matrices in (7.23) we see that the ratios are fixed by the θ value as shown in Fig. 7.3.2. In

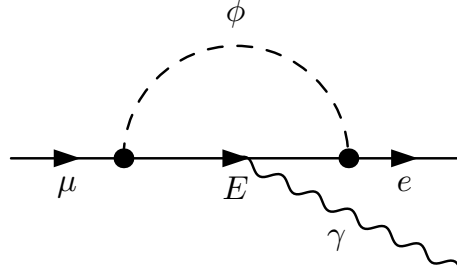


Figure 7.3: Diagram responsible for lepton flavor violation in our model.

LFV Process	Present Bound	Future Sensitivity
$\mu \rightarrow e\gamma$	5.7×10^{-13} [149]	6×10^{-14} [150]
$\tau \rightarrow e\gamma$	3.3×10^{-8} [151]	$\sim 3 \times 10^{-9}$ [152]
$\tau \rightarrow \mu\gamma$	4.4×10^{-8} [151]	$\sim 3 \times 10^{-9}$ [152]
$\mu \rightarrow eee$	1.0×10^{-12} [153]	$\sim 10^{-16}$ [154]
$\tau \rightarrow \mu\mu\mu$	2.1×10^{-8} [155]	$\sim 10^{-9}$ [152]
$\tau^- \rightarrow e^- \mu^+ \mu^-$	2.7×10^{-8} [155]	$\sim 10^{-9}$ [152]
$\tau^- \rightarrow \mu^- e^+ e^-$	1.8×10^{-8} [155]	$\sim 10^{-9}$ [152]
$\tau \rightarrow eee$	2.7×10^{-8} [155]	$\sim 10^{-9}$ [152]
$\mu^-, \text{Ti} \rightarrow e^-, \text{Ti}$	4.3×10^{-12} [156]	$\sim 10^{-18}$ [157, 158]
$\mu^-, \text{Au} \rightarrow e^-, \text{Au}$	7×10^{-13} [159]	
$\mu^-, \text{Al} \rightarrow e^-, \text{Al}$		$10^{-15} - 10^{-18}$ [160]
$\mu^-, \text{SiC} \rightarrow e^-, \text{SiC}$		10^{-14} [161]

Table 7.1: Current experimental bounds and future sensitivities for the most important LFV observables.

particular, we see that a large ratio (which we need to satisfy dark matter and LFV constraints) is only possible for two very narrow windows of values of θ , separated by π .

7.3.3 Lepton flavor violation

This model leads to lepton flavor violating processes. The most stringent experimental limits come from constraints in $\text{BR}(\mu \rightarrow e\gamma)$.

In our model, we can obtain this value similarly to [162]

$$\text{BR}(\mu \rightarrow e\gamma) = \frac{3\alpha_{\text{em}}}{64\pi G_{\text{F}}^2 m_E^4} \left| \sum_r \alpha_{r,1} \alpha_{r,2} G(m_{\phi_r}^2/m_E^2) \right|^2, \quad (7.25)$$

where [163]

$$G(x) = \frac{2 - 3x - 6x^2 + x^3 + 6x \log x}{6(x-x)^4}. \quad (7.26)$$

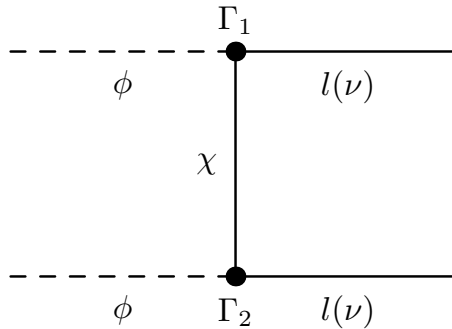


Figure 7.4: General diagram for relic density computations.

A similar expression also holds for the related processes $\tau \rightarrow \mu\gamma$ and $\tau \rightarrow e\gamma$. Other processes have more complicated analytical expressions and will be analyzed numerically, as shown in the following chapter.

In these models, typically the tightest lepton flavor violation constraint comes from the $\mu \rightarrow e\gamma$ process. But this situation may change in the near future with the experimental improvements achieved for other processes. We show a summary of this in table 7.1.

Lepton flavor violation constraints impose two conditions on the parameters of our model. Firstly, the particle in the loop must be not too heavy; and secondly the relevant couplings α must be of the order 0.1 to 1. This is compatible with neutrino masses since although very similar neutrino mass generation processes and lepton flavor violating processes differ in that the former violates lepton number whereas the latter does not. Thus, both constraints are compatible as long as β remains small, from what we saw in previous sections.

7.3.4 Dark matter

The dark matter candidate will be the lightest neutral particle with Z_2 charge -1 . In general this dark matter candidate could be in our model any of the two scalars or one of the three Majorana fermions. Both options are possible since the masses are free parameters in our lagrangian. In the fermionic case, the phenomenology will be similar to that of the singlet-doublet model [164, 165, 166], which has been investigated in the literature (see e.g. [167, 168, 169, 170, 171]). It is known in this case [172] that adjusting the mixing between the singlet and the doublet it is possible to obtain the right relic density for masses below around 1 TeV. In our specific case coannihilations with the extra scalar may introduce slight modifications result.

We will therefore focus our attentions in the case where the dark matter candidate is one of the scalars. We have in this case we have two possible scenarios. When the dominant interaction of the scalar is with the Stan-

Standard Model Higgs boson we have a so-called singlet scalar or Higgs-portal mode [173, 174, 175] with annihilations mediated by the Higgs. This type of models have been extensively studied in the literature (e.g. [176, 177, 178, 179, 180]). We will therefore in the following work with the second option, i.e. when the Yukawa interactions are the dominant mechanism. In this case the dark matter candidate will annihilate into leptons through the t -channel diagrams as seen in fig. 7.4 with the fermions propagators and which will be proportional to α^4 . We have therefore nontrivial relations between neutrino masses, lepton flavor violating, and dark matter processes, which will give rise to a rich phenomenology and potentially a stark avenue to constraint the different parameters.

As we have already seen, the mediator cannot have too large a mass, and the parameter α must be of order one, as seen for lepton flavor violating processes. We also notice that the dark matter candidate will be leptophilic, which will have implications for direct detection processes as we will analyze in later sections.

Given the described setup, the dark matter annihilation rate into charged leptons is given, in the non-relativistic limit, by [181]

$$\sigma v(\phi_1\phi_1 \rightarrow \ell^+\ell^-) = \frac{\alpha_{1\ell}^4 v^4}{60\pi} \frac{v^4}{m_{\phi_1}^2} \frac{1}{(1 + m_E^2/m_{\phi_1})^2}. \quad (7.27)$$

This expression accounts in principle for any possible combination of lepton pairs, although we will see that given the lepton flavor violation constraints from $\mu \rightarrow e\gamma$ the final state with $\tau^+\tau^-$ will dominate numerically. One important aspect to note is the somewhat unusual strong velocity dependence $\sim v^4$ which will have effects on indirect detection signatures as we will see in the next chapter. For neutrinos, the corresponding annihilating cross section has t and u channel contributions from the exchanges of neutral fermions $\chi_l\chi_m$,

$$\begin{aligned} \sigma v(\phi_1\phi_1 \rightarrow \nu\bar{\nu}') &= \sum_{l,m} \frac{m_{\phi_1}^2 v^2 \alpha_{1\nu}^2 \alpha_{1\nu'}^2 \xi_{2l}^2 \xi_{2m}^2}{12\pi} \\ &\times \frac{2m_{\phi_1}^2 m_{\chi_l} m_{\chi_m} + m_{\chi_l}^2 (m_{\phi_1}^2 + m_{\chi_m}^2) + m_{\phi_1}^2 (m_{\phi_1}^2 + m_{\chi_m}^2)}{(m_{\phi_1}^2 + m_{\chi_l}^2)^2 (m_{\phi_1}^2 + m_{\chi_m}^2)^2} \\ &+ \mathcal{O}(v^4). \end{aligned} \quad (7.28)$$

7.3.5 Dark matter self-energy

The self-energy of the dark matter candidate plays an important role in the understanding of the limits of the phenomenological calculations since the results are limited to regions where the corrections are negligible in

comparison to the mass of the particle itself. Therefore we will now turn the focus to the computation for this self-energy.

The contributions to the dark matter self-energy will come from diagrams like in Fig. ???. Here the leptons in the loop can correspond to either neutral ν, χ pairs, or charges l^\pm, E^\pm pairs. We will compute both cases at the same by setting general couplings $\Gamma_{1(2)} = L^{(\prime)}\mathbf{P}_L + R^{(\prime)}\mathbf{P}_R$. The result of computing the loop can be then written as a function of the so-called form factor A as

$$\mathcal{M} = \frac{i}{(4\pi)^2} A(p^2), \quad (7.29)$$

with the form factor in this case given by

$$A(p^2) = [2(LL' + RR')m_1m_2B_0 - 2(LR' + RL')(A_0(m_1^2) + m_0^2B_0 + p^2B_1)], \quad (7.30)$$

where we have used as is customary the definitions of the scalar integrals

$$A_0(m^2) = m^2(\Delta - \log \frac{m^2}{\mu^2} + 1) \quad (7.31)$$

and where for B_0 we take the approximation of negligible mass in one of the loop particles (either ν or l^\pm in this case)

$$B_0(p^2, 0, m^2) = \Delta - \log \frac{m^2}{\mu^2} + 2 + \frac{m^2 - p^2}{p^2} \log \left(\frac{m^2 - p^2}{m^2} \right) \quad (7.32)$$

and the scalar coefficient of the two-point function

$$B_1(p^2, m_1^2, m_2^2) = \frac{1}{2p_1^2} (A_0(m_1^2) - A_0(m_2^2) - (p_1^2 - m_2^2 + m_1^2)B_0(p^2, m_1^2, m_2^2)) \quad (7.33)$$

In our particular case, we notice that in the case of the neutral loop, the α coefficients are suppressed by the mixing matrix elements η , and that even for the charged contribution only the contribution for the larger α is sizable. By estimating the order of magnitude of the different terms (and in particular taking into account the loop suppression factors) it can be seen that the contribution becomes relevant in the TeV region, which is as we will see ruled out because of phenomenological reasons.

Chapter 8

Results

In this chapter we will present our numerical investigations of the model presented in the preceding chapter. We will start by describing our numerical setup in 8.1, and then present and analyze the numerical results obtained in 8.2.

8.1 Numerical implementation

We will start by presenting the different components entering the numerical computations as well as their mutual relationships.

8.1.1 Overview

The software setup for the numerical computations involves several components linked together which are summarized in Fig. 8.1:

1. The model is defined using **SARAH**.
2. **SPheno** takes the model parameters (at the lagrangian-level), and computes the masses, mixing matrices and branching ratios.
3. **FlavorKit** computes branching ratios relevant for lepton flavor violation.
4. **DarkSUSY** computes the relevant observables for dark matter constraints.
5. Finally we have a program that controls these computations, and makes the necessary scans of the parameter space (using the Metropolis-Hasting Markov Chain Monte Carlo algorithm as well as through defined grids or random scans).

The compilation of all the external programs for a given model is handled by the BSM Tool Box scripts [182], which eases the process.

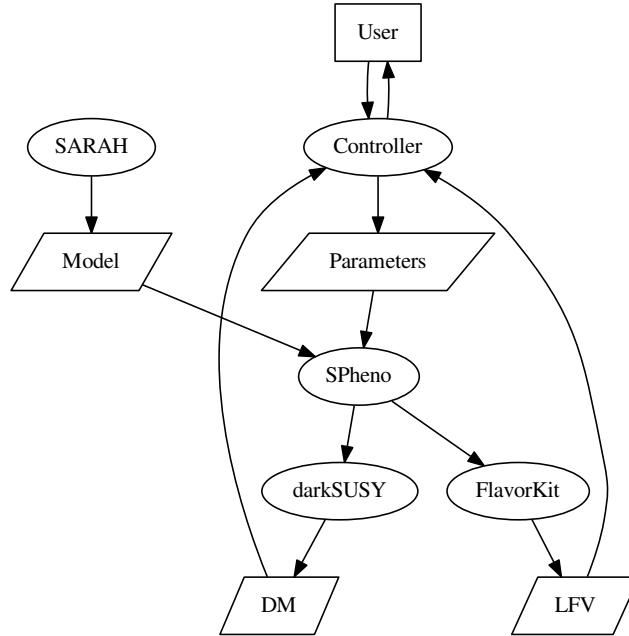


Figure 8.1: Diagram of the different components of our software setup for numerical computations and mutual dependencies.

8.1.2 SARAH

The input to SARAH is our model definition in files using their own conventions, and which must include the lagrangian, the list of particle definitions (gauge and mass eigenstates) and the list of parameters. We used as template the SM example included in the distribution, which also served as model (together with the seesaw models also included in the distribution).

8.1.3 SPHeno

SPHeno computes all the masses and mixing matrices for our model given a set of input parameters. It includes FlavorKit. Calls to SPHeno are expensive though, and therefore a previous filter for potentially viable points is used.

8.1.4 Micromegas

In a first attempt Micromegas was used to compute dark matter constraints. However, there seems to exist numerical difficulties in the integration in

CalcHEP, in particular it seems that the integration of different diagrams is done in such a way that it misses a crucial cancelation between them. A plot of these discrepancies between CalcHEP and analytical results can be seen in Fig. 8.2.

8.1.5 DarkSUSY

For the implementation of the relic density computations we use DarkSUSY. We use the equation for σv from [183], taking only the τ contribution (i.e., ignoring the negligible contributions from e, μ , that were always far below 1%), which gives

$$\sigma v = \frac{\alpha_{13}^4 v^4}{60\pi m_{\phi_1}^2} \frac{1}{1 + (m_E/m_{\phi_1}^2)^4}. \quad (8.1)$$

We use this to compute the invariant annihilation rate as defined in the DarkSUSY manual, and use the function `dsrdens()` from the DarkSUSY package, which computes the relic density for general (not necessarily SUSY)

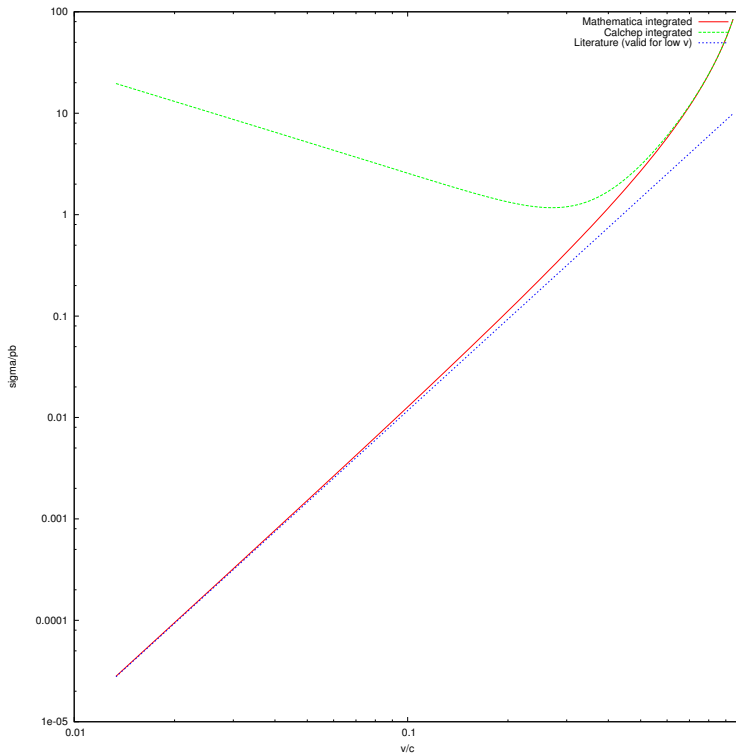


Figure 8.2: Comparison of the annihilation cross section as computed analytically by us and integrated using Mathematica (red line), the expected value at low velocity from [183] (blue line), and result from CalcHEP (green line).

models. The computations done in this way were checked to roughly match approximate analytical results.

8.2 Numerical results

For the reasons we have seen in previous chapters, we expect non-trivial interactions between dark matter, neutrino masses and lepton flavor phenomenology. In the following we will analyze in more detail these interactions. To this end we first scan through viable models which respect current the experimental constrains, and then analyze the potential effects of future improvements on these bounds, especially in the lepton flavor violation case.

After the Casa-Ibarra-like parametrization we saw in the previous chapter, we are left with a total of seven free parameters in the model, namely $m_{\phi_{1,2}}, \mu, m_S, \beta_{1,2}, \theta$. We do the sampling in two steps: First, we use a Markov Chain Monte Carlo method to learn about our space parameter and its regions of interest. Then using this information we sample over the allowed values for those models imposing the following constraints:

- **Neutrino masses:** We use the reparametrization shown in the previous chapter so that neutrino mass constraints are automatically satisfied in our parameter scan.
- **Dark matter relic density:** $\Omega_{\text{DM}} h^2 \sim 0.12$
- **Lepton flavor violation:** $\text{BR}(\mu \rightarrow e\gamma) < 5.8 \times 10^{-13}$

We also impose an arbitrary perturbativity limit on dimensionless couplings of three. We assume that the dark matter relic density is obtained via thermal freeze-out and ignore coannihilation effects by imposing a lower bound of $1.2m_{\phi_1}$ on masses. Lastly we impose an upper bound on mass of 10 TeV.

8.2.1 Parameter space

First we start to investigate the viable parameter space region. We show in fig. 8.3 the viable points as projected in the (m_ϕ, α_{1i}) for $i = e, \mu, \tau$. We notice that the lepton flavor violation constraint imposed on $\text{BR}(\mu \rightarrow e\gamma)$ suppressed $\alpha_{e1}, \alpha_{\mu 1}$ and therefore $\alpha_{\tau 1}$ can be or order 1, as required as we will see for the correct dark matter relic density, and therefore dark matter annihilates into $\tau^+\tau^-$ dominantly. We also observe how $\alpha_{\tau 1}$ increases with the dark matter mass, reaching the perturbativity limit at around $m_\phi \sim 600$ GeV, therefore imposing an upper bound of the dark matter candidate.

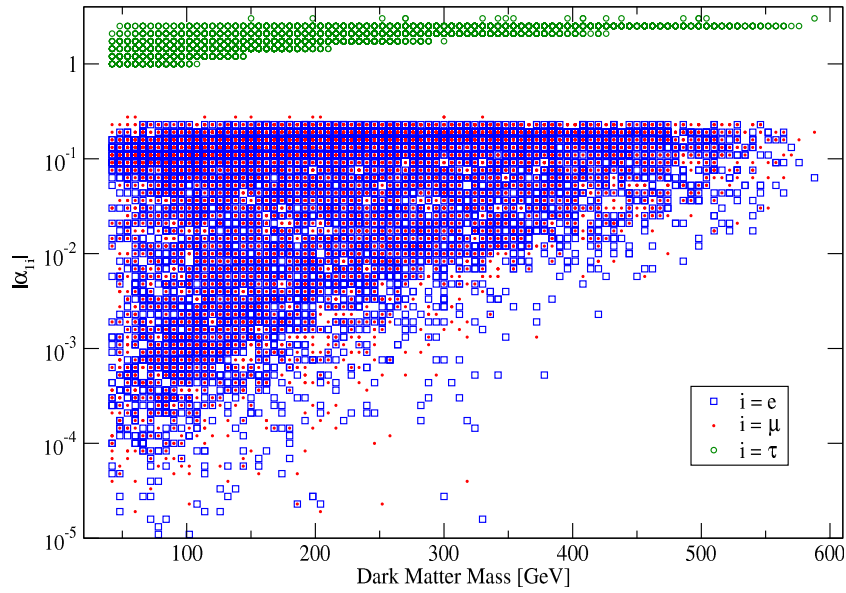


Figure 8.3: Values of neutrino couplings α_{1i} vs. dark matter candidate mass for viable models. The α_{1i} determine the dark matter annihilation rate and therefore there must be at least one non-negligible.

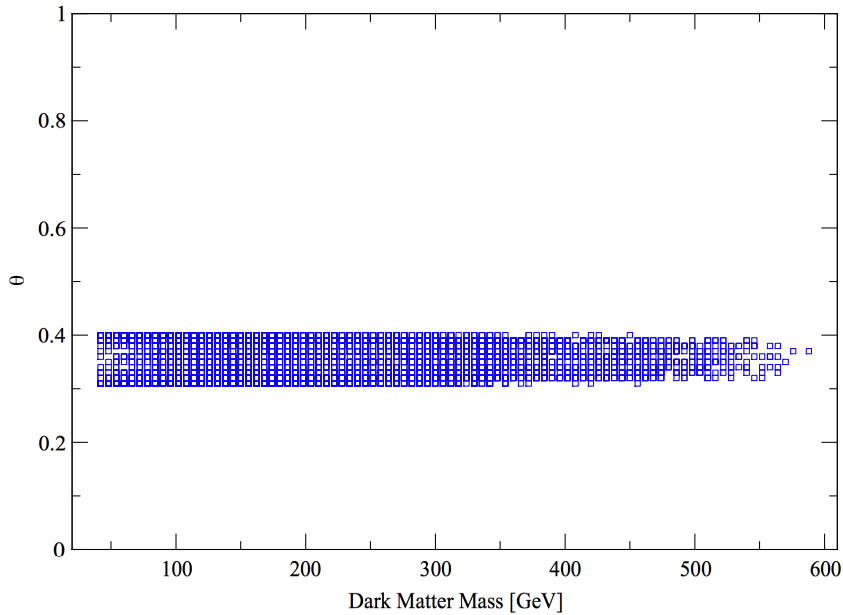


Figure 8.4: Values of θ as a function of the dark matter candidate mass for viable models. Notice how the conditions obtained in Ch. 7 mean that θ is constrained to a very narrow set of values.

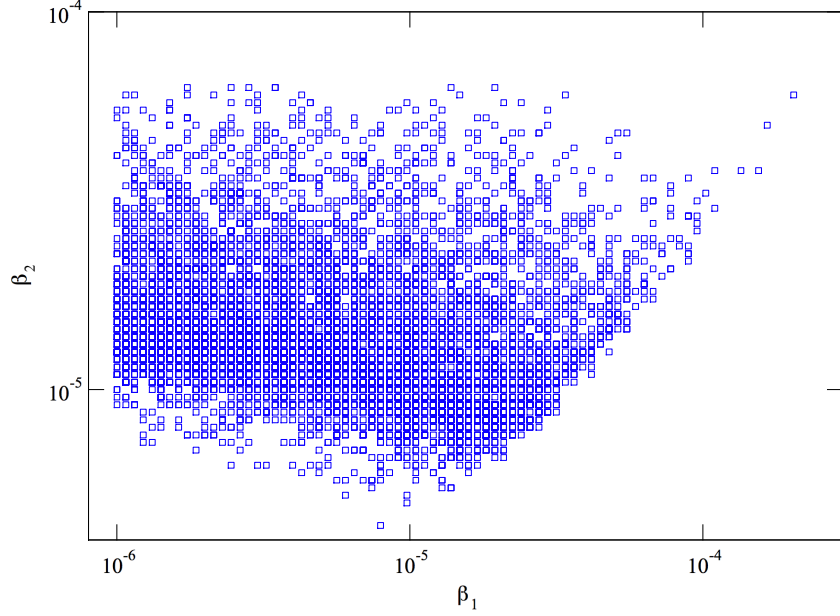


Figure 8.5: Values of β_2 vs. β_1 for viable models. Neutrino mass constraints impose that these be small.

The condition $\alpha_{1\tau} \gg \alpha_{1e}, \alpha_{1\mu}$ is not satisfied for generic values of the α_{ij} couplings. According to Eq. (7.23), we have that

$$\frac{\alpha_{1\tau}}{\alpha_{1e}} = \frac{\sqrt{m_2^\nu} \cos(\theta)(-c_{23}s_{12}s_{13} - c_{12}s_{23}) - \sqrt{m_3^\nu} \sin(\theta)c_{13}c_{23}}{\sqrt{m_2^\nu} \cos(\theta)c_{13}s_{12} - \sqrt{m_3^\nu} \sin(\theta)s_{13}}, \quad (8.2)$$

and

$$\frac{\alpha_{1\tau}}{\alpha_{1\mu}} = \frac{\sqrt{m_2^\nu} \cos(\theta)(-c_{23}s_{12}s_{13} - c_{12}s_{23}) - \sqrt{m_3^\nu} \sin(\theta)c_{13}c_{23}}{\sqrt{m_2^\nu}(c_{12}c_{23} - s_{12}s_{13}s_{23}) \cos(\theta) - c_{13}\sqrt{m_3^\nu}s_{23} \sin(\theta)}. \quad (8.3)$$

If we now require $\alpha_{1\tau} \gg \alpha_{1e}, \alpha_{1\mu}$ we get that, for typical values of the neutrino parameters, $\theta \sim 0.35$. The left panel of Fig. 4 shows the value of θ for our set of viable models. We see that, indeed, θ varies only within a narrow range around 0.35. Thus, the dark matter constraint and the limits on LFV processes select a rather specific value for θ .

We know that the neutrino masses arise from nonzero β couplings, and therefore imposing the small neutrino masses should make the β parameters small. This is what we in fact see in fig. 8.5, which shows the projection of the viable models onto the (β_1, β_2) plane. We observe that β_1 has an upper bound of 10^{-4} and that β_2 is also constrained to lie between 10^{-6} and 10^{-4} .

The dark matter relic density constraint imposes a strong correlation between the masses of the dark matter particle and the Dirac fermion which mediates the annihilation. We show in fig. 8.6 the ratio of these two masses,

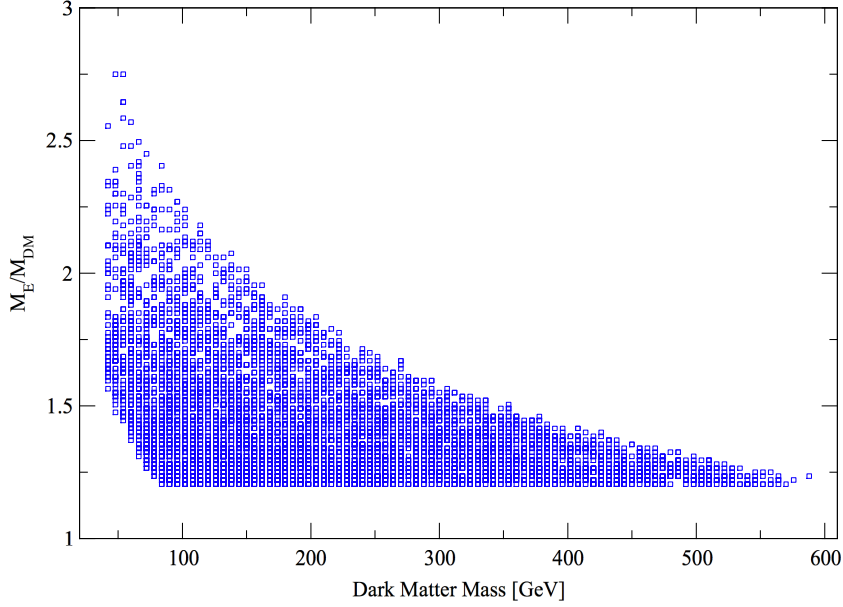


Figure 8.6: Ratio of the charged Dirac fermion E and the dark matter mass as a function of the dark matter candidate. Relic density favors a relatively small ratio.

m_E/m_ϕ as a function of the dark matter candidate. We note that as previously seen the lower bound of 1.2 is imposed to prevent coannihilations. We see that the two masses tend to be more similar the higher the dark matter mass, and this bounds the charged fermion mass to be small than around 720 GeV.

The masses of two of the Majorana fermions are going to be in general similar to each other since the mass split is generated by the small β parameters, being then both close to μ . The other Majorana fermion S can have in general a different mass. We plot in fig. 8.7 the largest mass of the three Majorana fermions and notice that although it can reach its upper bound of 10 TeV it tends to concentrate close to the dark matter mass.

8.2.2 Lepton flavor violation processes

We will focus in this section in the most relevant lepton flavor violating processes and compare their predicted rates with current and future experimental bounds. We will see that the most promising constraints will be $\text{BR}(\mu \rightarrow e\gamma)$ and $\text{CR}(\mu - e)$.

First we investigate lepton flavor processes involving τ . In particular, in fig. 8.8 we show the branching ratios for processes $\tau \rightarrow \mu\gamma$ and $\tau \rightarrow e\gamma$ for given dark matter masses. We also show the current experimental bounds (solid lines) as well as the expected future constraints (dashed lines). We

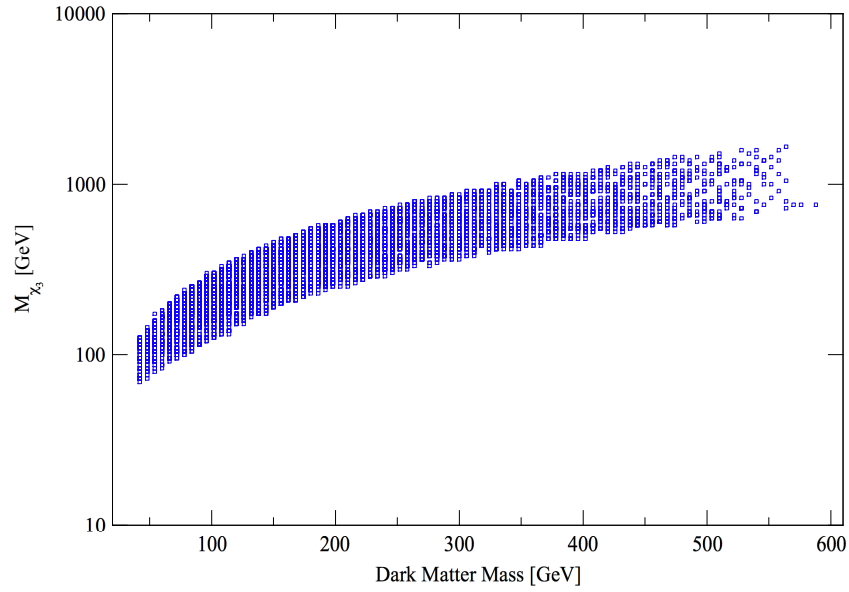


Figure 8.7: Mass of the heaviest odd Majorana fermion as a function of the dark matter candidate mass.

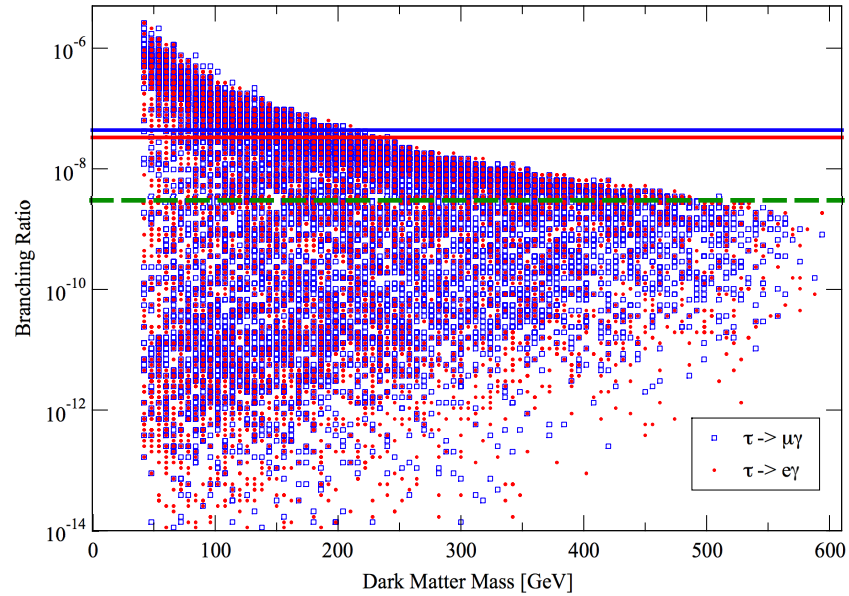


Figure 8.8: Branching ratios of $\tau \rightarrow \mu\gamma$ (blue squares) and $\tau \rightarrow e\gamma$ (red stars) as a function of the dark matter candidate mass. Solid lines are the current experimental limits, and dashed lines the expected future sensitivities.

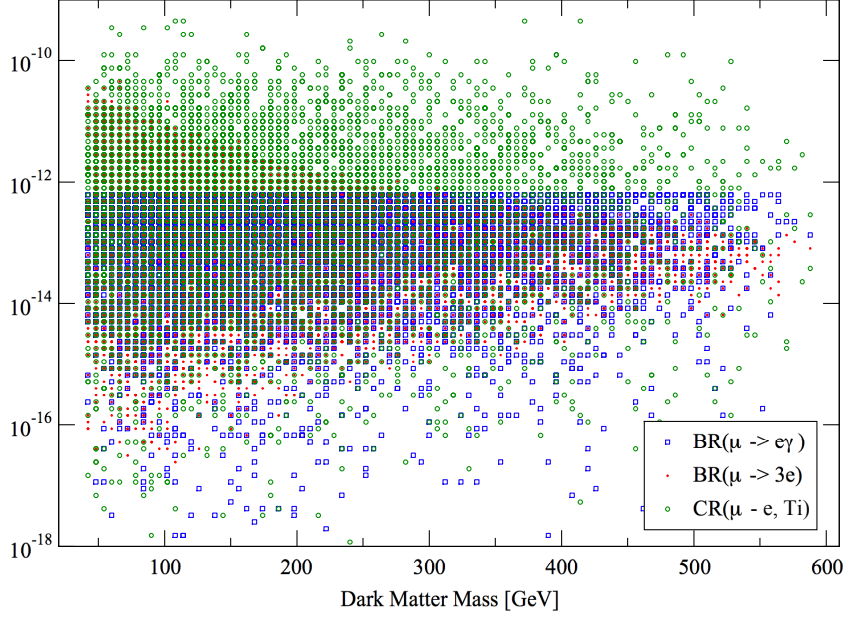


Figure 8.9: Branching ratios of the most relevant lepton flavor violating processes as a function of the dark matter candidate mass for viable models.

notice that both processes have similar behavior and values, and that in general the range tends to concentrate for larger dark matter masses, with the maximum clearly diminishing with the dark matter mass. We also note that for dark matter masses below around 250 GeV the limits are already competitive, and that future bounds can significantly constrain the viable model space for all dark matter masses.

The most relevant processes for lepton flavor violation are expected to be those related to $\mu - e$. We show them in fig. 8.9, in particular the branching ratios for $\mu \rightarrow e\gamma$ and $\mu \rightarrow 3e$ as well as the conversion rate $\text{CR}(\mu - e, \text{Ti})$. The current limits on $\text{BR}(\mu \rightarrow e\gamma)$ are only exceeded for low masses, but we observe that the one for $\text{CR}(\mu - e, \text{Ti})$ can be relevant over the whole dark matter mass range.

We analyze also the interaction between the different lepton flavor violating processes. For that we plot in fig. 8.10 $\text{BR}(\mu \rightarrow e\gamma)$ against $\text{BR}(\mu \rightarrow 3e)$, and in ?? $\text{BR}(\mu \rightarrow e\gamma)$ against $\text{CR}(\mu - e, \text{Ti})$. Again we show for every process the current experimental bound with a solid line and the expected future values in a dashed line. As we have already observed, current limits on $\mu \rightarrow 3e$ and $\mu - e$ are already competitive to rule out viable points, and thus imposing $\text{BR}(\mu \rightarrow e\gamma)$ limits is not necessary to analyze the lepton flavor violation phenomenology of this model. It is also important to notice that future improvements in $\text{BR}(\mu \rightarrow e\gamma)$ are not expected to be dramatic in terms of ruling out viable models, but improvements on $\mu \rightarrow 3e$ and $\mu - e$

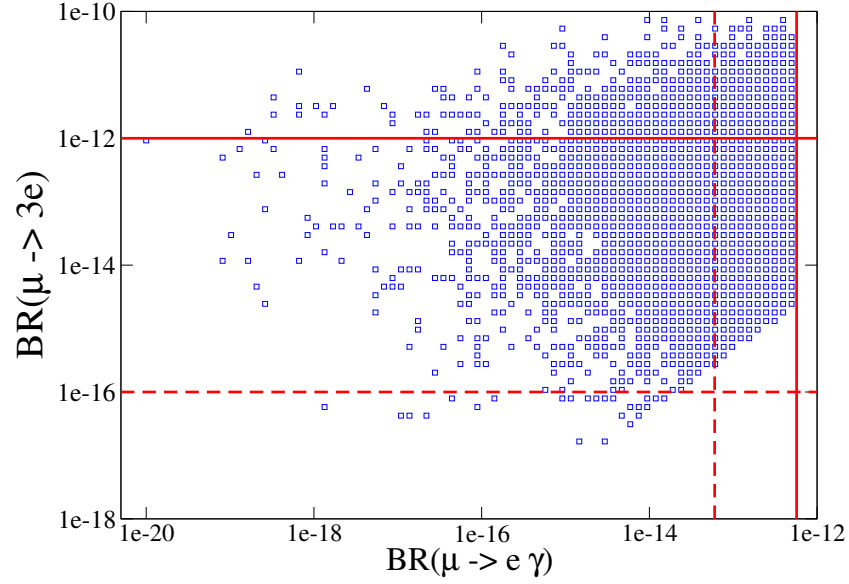


Figure 8.10: Relationship between branching ratios for $\mu \rightarrow e\gamma$ and $\mu \rightarrow 3e$. Solid lines are current experimental constraints and dashed lines are expected future sensitivities.

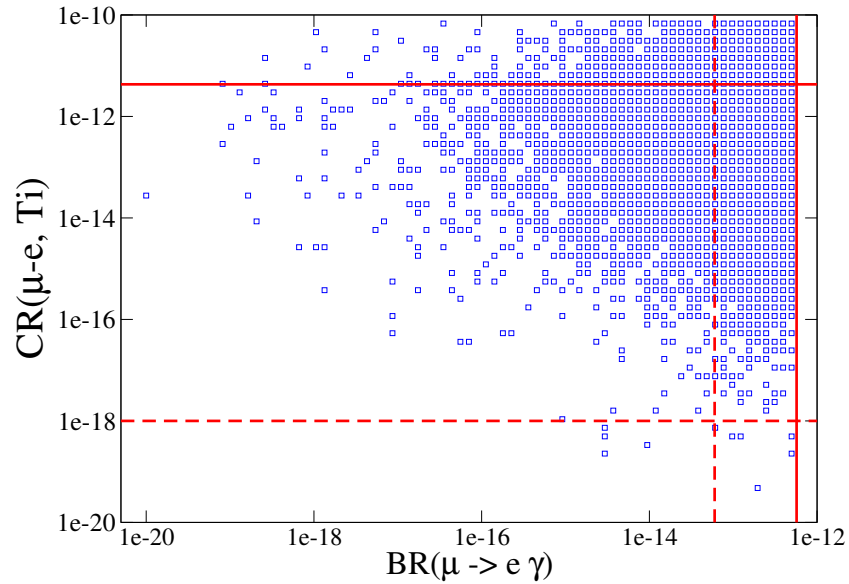


Figure 8.11: Similarly as 8.10 for $\mu \rightarrow e\gamma$ and $\mu - e$ conversion.

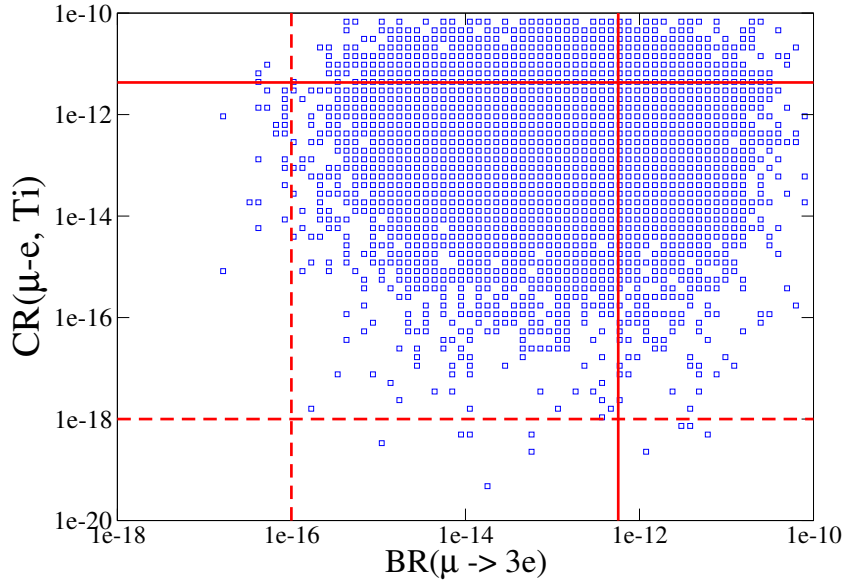


Figure 8.12: Similarly as 8.10 for $\mu \rightarrow 3e$ and $\mu - e$ conversion.

have the potential to rule out significant portions of the currently viable parameter space. In fact, as can be seen in fig. 8.12, where we plot $\text{BR}(\mu \rightarrow 3e)$ against $\text{CR}(\mu - e, \text{Ti})$, each of those two processes have the potential to rule out a significant portion of the viable parameter space, but when combined together no single viable point remains, which points towards the fact that improvements in lepton flavor constraints have the potential to probe the viable parameter space almost completely, or even completely.

8.2.3 Direct detection

Direct detection is not a promising path to phenomenologically study this model, because the dark matter particle is leptophilic, having vanishing tree-level scattering cross sections with nuclei. Even though radiative corrections generate a small nonzero contribution, they are still negligible with respect to detection purposes. At one loop, contributions mediated by Higgs and photon are possible. Similar effects have been studied [184] and the signals were below expected future sensitivities. Since in our case this would be even more suppressed by lepton masses and β parameters, this possibility is not a viable probing method.

8.2.4 Indirect detection

With respect to indirect detection, we notice that in this model the velocity suppression is v^4 for Majorana particles. Given the $v \sim 10^{-3}$ dependency for dark matter particles in the galactic halo, this implies around twelve

orders of magnitude below the thermal annihilation rate. However, and although neutrino, positron and antiproton channels are not expected to be of relevancy, internal bremsstrahlung processes [185] can have a sizable effect [183, 186] through high-energy gamma-ray emission which could potentially be observed in gamma-ray telescopes.

8.2.5 Collider phenomenology

Since the model contains several particles theoretically in range for LHC searches, we will briefly review the possibility of collider searches. In particular there is a charged fermion and the dark matter scalar which should be both in the hundreds of GeV. In particular our model seems to have similarities with the MSSM gaugino sector, where the Z_2 -odd charged and neutral particles correspond to the charginos and neutralinos. However, the fermions in the model do not decay via “golden” channel with missing transverse energy (as studied in Ch. 4), but directly into two charged leptons, a charged lepton and a neutrino or two neutrinos plus dark matter particles, which are invisible. Therefore the tripleton ATLAS and CMS analyses do not apply in our case. Two-lepton final states have been analyzed by ATLAS [67] and CMS [187], but with assumptions on the slepton masses. The case of Z' searches [188, 189] lack the missing transverse energy requirement, and W' analyses [188, 190] rely on the partial reconstruction of an s -channel resonance that is not applicable in this case. Therefore these analysis do not impose limits to the model, and a study would require a full reanalysis of the full signal together with background and detector simulations. Even in that case no significant further constraints are expected to the presented parameter space study.

Conclusions

Chapter 9

Conclusions

In particle physics, precision plays a central role. The standard model of particle physics yields results with accuracies unheard of in other branches of physics and science for that matter, yet there is clear evidence that a new framework will be needed to overcome some important theoretical and phenomenological difficulties. Only very precise theoretical results coupled with sources of very precise experimental measures can point to how these beyond the standard model frameworks may look like, for in physics accuracy has a qualitative and not only quantitative effect, and more precise predictions and measurements can rule out whole set of theories and drastically change our view of the universe. In this work, we have explored some different avenues to apply these concepts in the search for beyond the standard model physics in the era of unprecedented energies at hadron colliders such as the LHC and increasingly impressively accurate electroweak measurements.

We have started with a (necessarily very) brief summary of the standard model and its limitations that has served to put into context the following work. After that, this work has been divided in two more or less distinct parts, with of them focusing on one approach to precision predictions for particle physics: A first part has focused on supersymmetry at hadron colliders, and therefore has dealt with perturbative quantum chromodynamics (for resummation); and a second part has focused on non-supersymmetric minimal models for neutrino masses and dark matter. A further common theme in these two parts is that the sectors investigated were predominantly the electroweak sector of each of the model families (the supersymmetric electroweak sector with gauginos and obviously the electroweak sector of the standard model for the second part).

The first block comprises Ch. 2 to Ch. 4, and as discussed we have focused on precision predictions for supersymmetry at hadron collider. In particular we have focused on resummation predictions for gaugino¹ production. We

¹We have used the word gaugino to mean charginos and neutralinos throughout this work.

have started in Ch. 2 by presenting the necessary theoretical components for further analyses, namely an introduction to quantum chromodynamics as required to investigate hadron collider phenomenology, a necessarily concise presentation of resummation, where we have attempted to present the formalism as close to our implementation of it as possible (together with a more general introduction to simplify the developments), and lastly a presentation of the basic of supersymmetry to contextualize the gauginos in the theory. We have tried to present in these introductions as much as possible all details required for the later developments, but obviously some details had to be left out for space reasons. The reader is referred to the references pointed out in the different sections as a source of further details as required.

In Ch. 3 we have introduced the software Resummino that was developed for computations resummation predictions for beyond the standard model particle production. This software has been developed throughout time by different people in the research group of Prof. Michael Klasen [40, 41, 42, 43, 44, 45, 46, 39, 47, 48, 12]. In this thesis we present the work on the software presented in [39] comparing with previous versions of the code, and later in Ch. 3 we review the results published in [47] for gaugino production and that are widely used by experimental collaborations ATLAS and CMS. Further work has continued on this code as can be seen e.g. in [10].

In the second part, which comprises Ch. 5 to Ch. 8 of this thesis, we have focused on the electroweak sector of the standard model. In particular we have studied the issues of dark matter and neutrino masses as problems of the standard model of particle physics, and have set up a computational framework that allowed us to analyze theoretically and phenomenologically a possible minimal model that combined the solution to both issues.

In Ch. 5 we have reviewed the problem of dark matter, the existing evidence for the existence of dark matter, some of the different theoretical models that provide dark matter candidates, and the different experimental ways that have been and are being used to detect and measure it, as well as some practical aspects on relic density calculations.

In Ch. 6 we have focused on the issue of neutrino masses, and have reviewed some of the experimental evidence for a nonzero mass of neutrinos, have analyzed how the neutrino mass can be approached as an extension of the standard model, how such mass terms can look like, and some of the theoretical possibilities to realize such masses, as well as the lepton flavor violation consequences of those theoretical possibilities, which are phenomenologically very relevant.

In Ch. 7 we have presented the model we have analyzed from a theoretical point of view. We have contextualized it in terms of other previous or similar models, we have defined it mathematically in detail, and have analyzed its phenomenology, for dark matter, neutrino masses, lepton flavor violation, and collider constraints, as well as analyzed the the theoretical limits of these calculations.

Finally in Ch. 8 we have presented the numerical results of the phenomenological study. The first part of the chapter contains a more or less detailed explanation of the computational framework used to perform these analyses, and some of the limitations encountered as well as the solutions found, and in the second part of the chapter we have reviewed the results originally published in [146], with again a focus on dark matter, neutrino masses, lepton flavor violation as well as collider phenomenology. A similar variation of this framework has been later used in a related study for another minimal model originally presented in [191].

Overall we have presented in this work some distinct approaches to the issue of precision in particle physics, and have presented results which can be used to constrain the parameter space of some both supersymmetric and non-supersymmetric models and with the ever-increasing accuracy of the different running experiments test the current theoretical beyond the standard model ideas, leading to unforeseen new theoretical frameworks that will shape our understanding of Nature.

Appendix A

Gauginos total cross sections

For reference we present here the total cross sections tables for gaugino pair production from the computations in Ch. 4. The reader is referred to that chapter for further details.

Process	m_1 [GeV]	m_2 [GeV]	LO [fb]	NLO [fb]	NLO+NLL [fb]
$pp \rightarrow \chi_1^0 \chi_1^0$	161.7	161.7	0.81 ^{+5.8%} _{-5.3%}	1.06 ^{+3.5%} _{-3.0%} ^{+2.8%} _{-2.0%}	1.03 ^{+0.5%} _{-0.6%} ^{+2.9%} _{-2.0%}
$pp \rightarrow \chi_1^0 \chi_1^-$	161.7	303.5	0.16 ^{+6.0%} _{-5.5%}	0.20 ^{+2.5%} _{-2.4%} ^{+2.9%} _{-2.4%}	0.20 ^{+0.0%} _{-0.3%} ^{+2.9%} _{-2.5%}
$pp \rightarrow \chi_2^0 \chi_2^0$	303.8	303.8	0.85 ^{+9.2%} _{-7.9%}	1.07 ^{+3.5%} _{-3.5%} ^{+3.1%} _{-2.2%}	1.05 ^{+0.0%} _{-0.4%} ^{+3.5%} _{-1.9%}
$pp \rightarrow \chi_2^0 \chi_3^0$	303.8	526.5	0.21 ^{+9.4%} _{-8.1%}	0.25 ^{+2.6%} _{-2.9%} ^{+3.2%} _{-2.3%}	0.25 ^{+0.1%} _{-0.5%} ^{+3.2%} _{-2.3%}
$pp \rightarrow \chi_2^0 \chi_1^-$	303.8	303.5	14.46 ^{+6.7%} _{-6.1%}	17.25 ^{+1.6%} _{-1.7%} ^{+3.0%} _{-2.6%}	17.05 ^{+0.2%} _{-0.7%} ^{+3.1%} _{-2.6%}
$pp \rightarrow \chi_3^0 \chi_4^0$	526.5	542.4	0.83 ^{+11.0%} _{-9.3%}	0.97 ^{+2.8%} _{-3.3%} ^{+3.9%} _{-2.4%}	0.96 ^{+0.4%} _{-0.9%} ^{+3.8%} _{-2.5%}
$pp \rightarrow \chi_3^0 \chi_1^-$	526.5	303.5	0.12 ^{+9.4%} _{-8.1%}	0.15 ^{+2.6%} _{-2.9%} ^{+3.8%} _{-2.9%}	0.15 ^{+0.1%} _{-0.6%} ^{+3.8%} _{-3.0%}
$pp \rightarrow \chi_3^0 \chi_2^-$	526.5	542.2	0.42 ^{+11.2%} _{-9.5%}	0.50 ^{+2.8%} _{-3.3%} ^{+4.9%} _{-3.6%}	0.49 ^{+0.4%} _{-0.9%} ^{+4.9%} _{-3.5%}
$pp \rightarrow \chi_4^0 \chi_2^-$	542.4	542.2	0.39 ^{+11.3%} _{-9.6%}	0.47 ^{+2.7%} _{-3.2%} ^{+4.9%} _{-3.6%}	0.46 ^{+0.5%} _{-1.1%} ^{+4.9%} _{-3.7%}
$pp \rightarrow \chi_1^+ \chi_1^0$	303.5	161.7	0.38 ^{+6.0%} _{-5.4%}	0.46 ^{+2.5%} _{-2.4%} ^{+2.8%} _{-2.1%}	0.46 ^{+0.2%} _{-0.5%} ^{+2.9%} _{-2.1%}
$pp \rightarrow \chi_1^+ \chi_2^0$	303.5	303.8	35.16 ^{+6.3%} _{-5.8%}	40.90 ^{+1.6%} _{-1.7%} ^{+2.9%} _{-2.2%}	40.51 ^{+0.0%} _{-0.3%} ^{+2.9%} _{-2.2%}
$pp \rightarrow \chi_1^+ \chi_3^0$	303.5	526.5	0.34 ^{+9.2%} _{-7.9%}	0.40 ^{+2.6%} _{-2.9%} ^{+3.7%} _{-2.4%}	0.40 ^{+0.0%} _{-0.3%} ^{+3.6%} _{-2.5%}
$pp \rightarrow \chi_1^+ \chi_1^-$	303.5	303.5	25.64 ^{+6.6%} _{-5.9%}	30.37 ^{+1.7%} _{-1.9%} ^{+2.7%} _{-2.0%}	30.04 ^{+0.0%} _{-0.5%} ^{+2.7%} _{-2.1%}
$pp \rightarrow \chi_2^+ \chi_3^0$	542.2	526.5	1.27 ^{+11.1%} _{-9.4%}	1.46 ^{+2.9%} _{-3.3%} ^{+4.4%} _{-2.7%}	1.45 ^{+0.3%} _{-0.7%} ^{+4.3%} _{-2.9%}
$pp \rightarrow \chi_2^+ \chi_4^0$	542.2	542.4	1.21 ^{+11.2%} _{-9.5%}	1.37 ^{+2.7%} _{-3.2%} ^{+4.4%} _{-2.8%}	1.36 ^{+0.4%} _{-0.8%} ^{+4.6%} _{-2.6%}
$pp \rightarrow \chi_2^+ \chi_2^-$	542.2	542.2	0.86 ^{+10.9%} _{-9.3%}	1.00 ^{+2.6%} _{-3.1%} ^{+4.0%} _{-2.4%}	0.99 ^{+0.4%} _{-0.9%} ^{+4.1%} _{-2.4%}

Table A.1: Total cross sections for gaugino pair production for the 8 TeV LHC run for benchmark point 1 at LO, NLO and NLO+NLL. Cross sections below 0.1 fb are omitted.

Process	m_1 [GeV]	m_2 [GeV]	LO [fb]	NLO [fb]	NLO+NLL [fb]
$pp \rightarrow \chi_1^0 \chi_1^0$	249.6	249.6	$0.13^{+8.6\%}_{-7.5\%}$	$0.16^{+3.5\%+3.3\%}_{-3.4\%-2.3\%}$	$0.16^{+0.2\%+3.5\%}_{-0.3\%-2.4\%}$
$pp \rightarrow \chi_2^0 \chi_1^-$	471.9	471.8	$1.63^{+10.0\%}_{-8.6\%}$	$1.88^{+1.8\%+4.1\%}_{-2.4\%-3.1\%}$	$1.86^{+0.6\%+4.1\%}_{-1.2\%-3.1\%}$
$pp \rightarrow \chi_1^+ \chi_2^0$	471.8	471.9	$4.73^{+9.8\%}_{-8.4\%}$	$5.28^{+1.8\%+3.9\%}_{-2.4\%-2.5\%}$	$5.22^{+0.3\%+4.0\%}_{-0.6\%-2.5\%}$
$pp \rightarrow \chi_1^+ \chi_1^-$	471.8	471.8	$3.13^{+9.8\%}_{-8.4\%}$	$3.57^{+1.9\%+3.5\%}_{-2.5\%-2.2\%}$	$3.52^{+0.4\%+3.7\%}_{-0.7\%-2.3\%}$
$pp \rightarrow \chi_2^+ \chi_3^0$	766.3	754.0	$0.16^{+14.2\%}_{-11.6\%}$	$0.17^{+3.5\%+6.1\%}_{-4.2\%-3.8\%}$	$0.17^{+1.0\%+6.1\%}_{-1.8\%-3.8\%}$
$pp \rightarrow \chi_2^+ \chi_4^0$	766.3	766.6	$0.15^{+14.3\%}_{-11.7\%}$	$0.16^{+3.4\%+6.1\%}_{-4.2\%-3.9\%}$	$0.16^{+1.1\%+6.1\%}_{-1.8\%-4.0\%}$
$pp \rightarrow \chi_2^+ \chi_2^-$	766.3	766.3	$0.11^{+13.6\%}_{-11.2\%}$	$0.12^{+3.1\%+6.0\%}_{-3.9\%-3.5\%}$	$0.12^{+1.0\%+6.0\%}_{-1.8\%-3.6\%}$

Table A.2: Same as Tab. A.1 for benchmark point 18.

Process	m_1 [GeV]	m_2 [GeV]	LO [fb]	NLO [fb]	NLO+NLL [fb]
$pp \rightarrow \chi_1^0 \chi_1^0$	251.7	251.7	$0.12^{+8.6\%}_{-7.5\%}$	$0.16^{+3.5\%+3.3\%}_{-3.4\%-2.3\%}$	$0.15^{+0.2\%+3.4\%}_{-0.3\%-2.4\%}$
$pp \rightarrow \chi_2^0 \chi_1^-$	478.5	478.5	$1.50^{+10.1\%}_{-8.6\%}$	$1.73^{+1.8\%+4.2\%}_{-2.4\%-3.1\%}$	$1.71^{+0.6\%+4.1\%}_{-1.2\%-3.2\%}$
$pp \rightarrow \chi_1^+ \chi_2^0$	478.5	478.5	$4.37^{+9.9\%}_{-8.5\%}$	$4.86^{+1.8\%+3.9\%}_{-2.4\%-2.5\%}$	$4.81^{+0.3\%+4.2\%}_{-0.6\%-2.6\%}$
$pp \rightarrow \chi_1^+ \chi_1^-$	478.5	478.5	$2.89^{+9.9\%}_{-8.5\%}$	$3.28^{+1.9\%+3.5\%}_{-2.5\%-2.3\%}$	$3.24^{+0.5\%+3.8\%}_{-0.7\%-2.3\%}$

Table A.3: Same as Tab. A.1 for benchmark point 31.

Bibliography

- [1] R. K. Ellis, W. J. Stirling, and B. R. Webber, *QCD and Collider Physics* (Cambridge University Press, 2003).
- [2] J. C. Collins and D. E. Soper, *Ann. Rev. Nucl. Part. Sci.* **37**, 383 (1987).
- [3] S. Bethke, *Eur. Phys. J. C.* **64**, 689 (2009).
- [4] C. Patrignani et al., *Chin. Phys. C* **40**, 100001 (2016).
- [5] D. J. Gross and F. Wilczek, *Phys. Rev. Lett.* **30**, 1343 (1973).
- [6] H. D. Politzer, *Phys. Rev. Lett.* **30**, 1346 (1973).
- [7] G. F. Sterman, in *QCD and beyond. Proceedings, Theoretical Advanced Study Institute in Elementary Particle Physics, TASI-95, Boulder, USA, June 4-30, 1995* (1995), pp. 327–408, hep-ph/9606312.
- [8] G. Sterman, *Nucl. Phys. B* **281**, 310 (1987).
- [9] S. Catani and L. Trentadue, *Nucl. Phys.* **B327**, 323 (1989).
- [10] M. Rothering, Ph.D. thesis, WWU (2017).
- [11] B. Fuks, Ph.D. thesis, Université de Grenoble (2007).
- [12] J. Debove, Ph.D. thesis, Université de Grenoble (2010).
- [13] C. Borschensky, Ph.D. thesis, Universität Münster (2016).
- [14] V. Theeuwes, Ph.D. thesis, Universität Münster (2015).
- [15] T. Kinoshita, *J. Math. Phys.* **3**, 650 (1962).
- [16] T. D. Lee and M. Nauenberg, *Phys. Rev.* **133**, B1549 (1964).
- [17] G. Altarelli and G. Parisi, *Nucl. Phys. B* **126**, 298 (1977).
- [18] S. Catani and L. Trentadue, *Nucl. Phys. B* **327**, 323 (1989).

- [19] J. C. Collins, D. Soper, and G. Sterman, Nucl. Phys. B **250**, 199 (1985).
- [20] S. Catani, D. de Florian, and M. Grazzini, Nucl. Phys. B **596**, 299 (2001).
- [21] D. de Florian and M. Grazzini, Nucl. Phys. Lett. **85**, 4678 (2000).
- [22] D. de Florian and M. Grazzini, Nucl. Phys. B **616**, 247 (2001).
- [23] S. P. Martin, pp. 1–98 (1997), [Adv. Ser. Direct. High Energy Phys.18,1(1998)], hep-ph/9709356.
- [24] R. Haag, J. T. Lopuszanski, and M. Sohnius, Nucl. Phys. **B88**, 257 (1975), [,257(1974)].
- [25] S. R. Coleman and J. Mandula, Phys. Rev. **159**, 1251 (1967).
- [26] J. Rosiek (1995), hep-ph/9511250.
- [27] J. Alwall, M. Herquet, F. Maltoni, O. Mattelaer, and T. Stelzer, JHEP **1006**, 128 (2011), arXiv:1106.0522 [hep-ph].
- [28] C. Balazs and C. P. Yuan, Phys. Rev. **D56**, 5558 (1997), hep-ph/9704258.
- [29] F. Landry, R. Brock, P. M. Nadolsky, and C. P. Yuan, Phys. Rev. **D67**, 073016 (2003), hep-ph/0212159.
- [30] G. A. Ladinsky and C. P. Yuan, Phys. Rev. **D50**, R4239 (1994), hep-ph/9311341.
- [31] Q.-H. Cao, C.-R. Chen, C. Schmidt, and C. P. Yuan (2009), 0909.2305.
- [32] C. Balazs and C. P. Yuan, Phys. Lett. **B478**, 192 (2000), hep-ph/0001103.
- [33] W. Beenakker et al., JHEP **1612**, 133 (2016).
- [34] W. Beenakker et al., JHEP **1412**, 023 (2014).
- [35] W. Beenakker et al., JHEP **1605**, 153 (2016).
- [36] W. Beenakker, R. Hopker, M. Spira, and P. M. Zerwas, Nucl. Phys. **B492**, 51 (1997), hep-ph/9610490.
- [37] W. Beenakker, M. Kramer, T. Plehn, M. Spira, and P. M. Zerwas, Nucl. Phys. **B515**, 3 (1998), hep-ph/9710451.

- [38] W. Beenakker, M. Klasen, M. Kramer, T. Plehn, M. Spira, and P. M. Zerwas, *Phys. Rev. Lett.* **83**, 3780 (1999), [Erratum: *Phys. Rev. Lett.*100,029901(2008)], [hep-ph/9906298](#).
- [39] B. Fuks, M. Klasen, D. R. Lamprea, and M. Rothering, *Eur. Phys. J.* **C73**, 2480 (2013), 1304.0790.
- [40] G. Bozzi, B. Fuks, and M. Klasen, *Nucl. Phys.* **B794**, 46 (2008), 0709.3057.
- [41] G. Bozzi, B. Fuks, and M. Klasen, *Phys. Rev.* **D74**, 015001 (2006), [hep-ph/0603074](#).
- [42] G. Bozzi, B. Fuks, B. Herrmann, and M. Klasen, *Nucl. Phys.* **B787**, 1 (2007), 0704.1826.
- [43] G. Bozzi, B. Fuks, and M. Klasen, *Nucl. Phys.* **B777**, 157 (2007), [hep-ph/0701202](#).
- [44] J. Debove, B. Fuks, and M. Klasen, *Nucl. Phys.* **B842**, 51 (2011), 1005.2909.
- [45] J. Debove, B. Fuks, and M. Klasen, *Phys. Lett.* **B688**, 208 (2010), 0907.1105.
- [46] J. Debove, B. Fuks, and M. Klasen, *Nucl. Phys.* **B849**, 64 (2011), 1102.4422.
- [47] B. Fuks, M. Klasen, D. R. Lamprea, and M. Rothering, *JHEP* **10**, 081 (2012), 1207.2159.
- [48] B. Fuks, M. Klasen, and M. Rothering, *JHEP* **07**, 053 (2016), 1604.01023.
- [49] M. Rothering, Master's thesis, Universität Münster (2012).
- [50] T. Jezo, M. Klasen, D. R. Lamprea, F. Lyonnet, and I. Schienbein, *JHEP* **12**, 092 (2014), 1410.4692.
- [51] D. R. Lamprea, Master's thesis, Universität Münster (2012).
- [52] T. Hahn and M. Perez-Victoria, *Comput. Phys. Commun.* **118**, 153 (1999), [hep-ph/9807565](#).
- [53] S. Catani, S. Dittmaier, M. H. Seymour, and Z. Trocsanyi, *Nucl. Phys.* **B627**, 189 (2002), [hep-ph/0201036](#).
- [54] S. Catani and M. H. Seymour, *Nucl. Phys.* **B485**, 291 (1997), [Erratum: *Nucl. Phys.*B510,503(1998)], [hep-ph/9605323](#).

- [55] M. Galassi et al., *GNU Scientific Library Reference Manual* (Network Theory Ltd., 2009).
- [56] G. P. Lepage, *J. Comp. Phys.* **27**, 192 (1978).
- [57] B. Gough, *GNU Scientific Library Reference Manual - Third Edition* (Network Theory Ltd., 2009), 3rd ed., ISBN 0954612078, 9780954612078.
- [58] A. Buckley, J. Ferrando, S. Lloyd, K. Nordström, B. Page, M. Rfenacht, M. Schnherr, and G. Watt, *Eur. Phys. J.* **C75**, 132 (2015), 1412.7420.
- [59] P. Skands et al., *JHEP* **0407**, 036 (2004).
- [60] B. C. Allanach et al., *Comp. Phys. Commun.* **180**, 8 (2009).
- [61] S. S. AbdusSalam et al., *Eur. Phys. J.* **C71**, 1835 (2011), 1109.3859.
- [62] LEP2 SUSY Working Group, LEPSUSYWG/01-03.1.
- [63] LEP2 SUSY Working Group, LEPSUSYWG/02-04.1.
- [64] CDF Collab., CDF Note 10636 (2011).
- [65] D0 Collab., *Phys. Lett. B* **680**, 34 (2009).
- [66] ATLAS Collab., ATLAS-CONF **2017**, 039 (2017).
- [67] ATLAS Collab., *JHEP* **1405**, 071 (2014).
- [68] CMS Collab., arXiv:1709.05406.
- [69] ATLAS Collab., arXiv:1708.07875.
- [70] CMS Collab., CMS-PAS-SUS-17-004.
- [71] ATLAS Collab., *Eur. Phys. J.* **C75**, 208 (2015).
- [72] ATLAS Collab., *Phys. Rev. D* **93**, 052002 (2016).
- [73] CMS Collab., *JHEP* **1511**, 189 (2015).
- [74] H. Dreiner et al., *Eur. Phys. J.* **C62**, 547 (2009).
- [75] LEP2 SUSY Working Group, LEPSUSYWG/04-09.1.
- [76] CDF Collab., *Phys. Rev. Lett.* **104**, 011801 (2010).
- [77] D0 Collab., *Phys. Rev. Lett.* **2015**, 221802 (2010).
- [78] ATLAS Collab., *Eur. Phys. J.* **C76**, 517 (2016).

- [79] CMS Collab., arXiv:1707.06193.
- [80] ATLAS Collab., Eur. Phys. J. **C77**, 144 (2017).
- [81] CMS Collab., Phys. Rev. D **90**, 902007 (2014).
- [82] CMS Collab., JHEP **04**, 124 (2016).
- [83] ATLAS Collab., ATLAS-CONF-2016-075.
- [84] CMS Collab., Phys. Rev. D **91**, 012007 (2015).
- [85] B. C. Allanach et al., Eur. Phys. J. **C25**, 113 (2002), hep-ph/0202233.
- [86] V. D. Barger, R. W. Robinett, W.-Y. Keung, and R. J. N. Phillips, Phys. Lett. **131B**, 372 (1983).
- [87] J. Debove, B. Fuks, and M. Klasen, Phys. Rev. **D78**, 074020 (2008), 0804.0423.
- [88] G. Corcella, I. G. Knowles, G. Marchesini, S. Moretti, K. Odagiri, P. Richardson, M. H. Seymour, and B. R. Webber, JHEP **01**, 010 (2001), hep-ph/0011363.
- [89] T. Sjostrand, S. Mrenna, and P. Z. Skands, JHEP **05**, 026 (2006), hep-ph/0603175.
- [90] S. Frixione and B. R. Webber, JHEP **06**, 029 (2002), hep-ph/0204244.
- [91] S. Frixione, P. Nason, and C. Oleari, JHEP **11**, 070 (2007), 0709.2092.
- [92] S. Catani, F. Krauss, R. Kuhn, and B. R. Webber, JHEP **11**, 063 (2001), hep-ph/0109231.
- [93] M. L. Mangano, M. Moretti, F. Piccinini, and M. Treccani, JHEP **01**, 013 (2007), hep-ph/0611129.
- [94] J. Alwall, M. Herquet, F. Maltoni, O. Mattelaer, and T. Stelzer, JHEP **06**, 128 (2011), 1106.0522.
- [95] C. Degrande, C. Duhr, B. Fuks, D. Grellscheid, O. Mattelaer, and T. Reiter, Comput. Phys. Commun. **183**, 1201 (2012), 1108.2040.
- [96] C. Duhr and B. Fuks, Comput. Phys. Commun. **182**, 2404 (2011), 1102.4191.
- [97] A. Djouadi, J.-L. Kneur, and G. Moultaka, Comput. Phys. Commun. **176**, 426 (2007), hep-ph/0211331.
- [98] M. Cacciari, G. P. Salam, and G. Soyez, Eur. Phys. J. **C72**, 1896 (2012), 1111.6097.

- [99] V. C. Rubin and W. K. Ford, Jr., *Astrophys. J.* **159**, 379 (1970).
- [100] G. Bertone, *Particle Dark Matter* (Cambridge University Press, 2010).
- [101] P. A. R. Ade et al. (Planck), *Astron. Astrophys.* **594**, A13 (2016), 1502.01589.
- [102] A. A. Penzias and R. W. Wilson, *Astrophys. J.* **142**, 419 (1965).
- [103] E. Komatsu et al. (WMAP), *Astrophys. J. Suppl.* **180**, 330 (2009), 0803.0547.
- [104] S. Odenwald, J. Newmark, and G. F. Smoot (1996), [astro-ph/9610238](#).
- [105] G. Bertone, D. Hooper, and J. Silk, *Physics Reports* **405**, 279 (2005).
- [106] G. Jungman, M. Kamionkowski, and K. Griest, *Phys.Rept.* **267**, 195 (1996), [hep-ph/9506380](#).
- [107] M. Drewes and B. Garbrecht, *JHEP* **1303**, 096 (2013), 1206.5537.
- [108] L. Bergström, P. Ullio, and J. Buckley, *Astropart. Phys.* **9**, 137 (1998).
- [109] J. Conrad, [arXiv:1411.1925 \[hep-ph\]](#).
- [110] T. Bringmann and C. Weniger, *Phys. Dark Univ.* **1**, 194 (2012).
- [111] S. Ando and E. Komatsu, *Phys. Rev. D* **73**, 023521 (2006).
- [112] A. Cuoco, A. Sella, J. Conrad, and S. Hannestad, *Mon. Not. Roy. Astron. Soc.* **414**, 2040 (2011).
- [113] E. Majorana, *Nuovo Cimento* **5**, 171 (1937).
- [114] S. T. Petcov, *Adv. High Energy Phys.* **2013**, 852987 (2013), 1303.5819.
- [115] A. G. Cohen, S. L. Glashow, and Z. Ligeti, *Phys. Lett. B* **678**, 191 (2009).
- [116] S. Goswami et al., *Nucl. Phys. B (Proc. Supp.)* **143**, 121 (2005).
- [117] J. N. Bahcall, A. M. Serenelli, and S. Basu, *Astrophys. J.* **621**, L85 (2005), [astro-ph/0412440](#).
- [118] B. Pontecorvo, *Sov. Phys. JETP* **26**, 984 (1968).
- [119] Y. Fukuda et al. (Super-Kamiokande Collaboration), *Phys.Rev.Lett.* **81**, 1562 (1998), [hep-ex/9807003](#).

- [120] S. Weinberg, Phys. Rev. Lett. **43**, 1566 (1979).
- [121] F. Bonnet, M. Hirsch, T. Ota, and W. Winter, JHEP **1207**, 153 (2012), arXiv:1204.5862 [hep-ph].
- [122] T. Takagi, Japanese J. Math. **1**, 83 (1927).
- [123] A. Abada, C. Biggio, F. Bonnet, M. Gavela, and T. Hambye, JHEP **0712**, 061 (2007).
- [124] P. Minkowski, Phys. Lett. B **67**, 421 (1977).
- [125] M. Magg and C. Wetterich, Phys. Lett. B **94**, 61 (1980).
- [126] J. Schechter and J. Valle, Phys. Rev. D **22**, 2227 (1980).
- [127] C. Wetterich, Nucl. Phys. B **187**, 343 (1981).
- [128] G. Lazarides, Q. Shafi, and C. Wetterich, Nucl. Phys. B **181**, 187 (1981).
- [129] R. N. Mohapatra and G. Senjanovic, Phys. Rev. D **23**, 165 (1981).
- [130] T. P. Cheng and L.-F. Li, Phys. Rev. D **22**, 2680 (1980).
- [131] R. Foot, H. Lew, X. He, and G. C. Joshi, Z. Phys **C44**, 441 (1989).
- [132] R. N. Mohapatra and J. Valle, Phys. Rev. D **34**, 1642 (1986).
- [133] A. Zee, Phys. Lett. **93B**, 389 (1980).
- [134] A. M. Baldini et al. (MEG), Eur. Phys. J. **C76**, 434 (2016), 1605.05081.
- [135] L. Calibbi and G. Signorelli, Riv. Nuovo Cim. **41**, 1 (2018), 1709.00294.
- [136] S. M. Bilenky and S. T. Petcov, Rev. Mod. Phys. **59**, 671 (1987), [Erratum: Rev. Mod. Phys.60,575(1988)].
- [137] S. L. Glashow and S. Weinberg, Phys. Rev. **D15**, 1958 (1977).
- [138] R. H. Bernstein and P. S. Cooper, Phys. Rept. **532**, 27 (2013), 1307.5787.
- [139] A. M. Teixeira, in *28th Rencontres de Blois on Particle Physics and Cosmology Blois, France, May 29-June 3, 2016* (2016), 1612.06194, URL <https://inspirehep.net/record/1504987/files/arXiv:1612.06194.pdf>.

- [140] A. Yu. Smirnov and M. Tanimoto, Phys. Rev. **D55**, 1665 (1997), hep-ph/9604370.
- [141] A. Yu. Smirnov and Z.-j. Tao, Nucl. Phys. **B426**, 415 (1994), hep-ph/9403311.
- [142] L. M. Krauss, S. Nasri, and M. Trodden, Phys. Rev. **D67**, 085002 (2003), hep-ph/0210389.
- [143] K. Cheung and O. Seto, Phys. Rev. **D69**, 113009 (2004), hep-ph/0403003.
- [144] E. Ma, Phys.Rev. **D73**, 077301 (2006), hep-ph/0601225.
- [145] D. Restrepo, O. Zapata, and C. E. Yaguna, JHEP **1311**, 011 (2013), arXiv:1308.3655 [hep-ph].
- [146] S. Esch, M. Klasen, D. R. Lamprea, and C. E. Yaguna, Eur. Phys. J. **C78**, 88 (2018), 1602.05137.
- [147] E. Ma, Phys. Rev. D **73**, 077301 (2006), arXiv:hep-ph/0601225.
- [148] J. A. Casas and A. Ibarra, Nucl. Phys. B **618**, 171 (2001).
- [149] J. Adam et al. (MEG Collaboration), Phys.Rev.Lett. **110**, 201801 (2013), 1303.0754.
- [150] A. M. Baldini et al. (2013), 1301.7225.
- [151] B. Aubert et al. (BaBar Collaboration), Phys.Rev.Lett. **104**, 021802 (2010), 0908.2381.
- [152] T. Aushev et al. (2010), 1002.5012.
- [153] U. Bellgardt et al. (SINDRUM), Nucl. Phys. **B299**, 1 (1988).
- [154] A. Blondel et al. (2013), 1301.6113.
- [155] K. Hayasaka et al., Phys. Lett. **B687**, 139 (2010), 1001.3221.
- [156] C. Dohmen et al. (SINDRUM II), Phys. Lett. **B317**, 631 (1993).
- [157] The PRISM/PRIME Group (2006), http://j-parc.jp/researcher/Hadron/en/pac_0606/pdf/p20-Kuno.pdf.
- [158] A. Sato, PoS **NUFACT08**, 105 (2008).
- [159] W. H. Bertl et al. (SINDRUM II), Eur. Phys. J. **C47**, 337 (2006).

- [160] R. P. Litchfield, in *Interplay between Particle and Astroparticle physics London, United Kingdom, August 18-22, 2014* (2014), 1412.1406, URL <http://inspirehep.net/record/1332516/files/arXiv:1412.1406.pdf>.
- [161] H. Natori (DeeMe), Nucl. Phys. Proc. Suppl. **248-250**, 52 (2014).
- [162] S. Fraser, E. Ma, and O. Popov, Phys. Lett. B **737**, 280 (2014), arXiv:1408.4785 [hep-ph].
- [163] S. Kanemitsu and K. Tobe, Phys. Rev. D **86**, 095025 (2012).
- [164] N. Arkani-Hamed, S. Dimopoulos, and S. Kachru (2005), hep-th/0501082.
- [165] R. Mahbubani and L. Senatore, Phys. Rev. **D73**, 043510 (2006), hep-ph/0510064.
- [166] F. DEramo, Phys. Rev. D **76**, 08522 (2007), arXiv:0705.4493 [hep-ph].
- [167] R. Enberg, P. J. Fox, L. J. Hall, A. Y. Papaioannou, and M. Papucci, JHEP **11**, 014 (2007), 0706.0918.
- [168] T. Cohen, J. Kearney, A. Pierce, and D. Tucker-Smith, Phys. Rev. **D85**, 075003 (2012), 1109.2604.
- [169] C. Cheung and D. Sanford, JCAP **1402**, 011 (2014), 1311.5896.
- [170] L. Calibbi, A. Mariotti, and P. Tziveloglou, JHEP **10**, 116 (2015), 1505.03867.
- [171] C. E. Yaguna, Phys. Rev. **D92**, 115002 (2015), 1510.06151.
- [172] D. Restrepo, A. Rivera, M. Snchez-Pelez, O. Zapata, and W. Tangarife, Phys. Rev. **D92**, 013005 (2015), 1504.07892.
- [173] C. Burgess, M. Pospelov, and T. ter Veldhuis, Nucl.Phys. **B619**, 709 (2001), hep-ph/0011335.
- [174] H. Davoudiasl, R. Kitano, T. Li, and H. Murayama, Phys. Lett. **B609**, 117 (2005), hep-ph/0405097.
- [175] V. Barger, P. Langacker, M. McCaskey, M. J. Ramsey-Musolf, and G. Shaughnessy, Phys.Rev. **D77**, 035005 (2008), 0706.4311.
- [176] R. Dick, R. B. Mann, and K. E. Wunderle, Nucl. Phys. **B805**, 207 (2008), 0803.1444.
- [177] C. E. Yaguna, JCAP **0903**, 003 (2009), 0810.4267.

- [178] A. Goudelis, Y. Mambrini, and C. Yaguna, *JCAP* **0912**, 008 (2009), 0909.2799.
- [179] S. Profumo, L. Ubaldi, and C. Wainwright, *Phys. Rev.* **D82**, 123514 (2010), 1009.5377.
- [180] J. M. Cline, K. Kainulainen, P. Scott, and C. Weniger, *Phys. Rev.* **D88**, 055025 (2013), 1306.4710.
- [181] F. Giacchino, L. Lopez-Honorez, and M. H. G. Tytgat, *JCAP* **1310**, 025 (2013), 1307.6480.
- [182] F. Staub, T. Ohl, W. Porod, and C. Speckner, *CPC* **183**, 2165 (2012).
- [183] F. Giacchino, L. Lopez-Honorez, and M. H. G. Tytgat, *JCAP* **1310**, 025 (2013), arXiv:1307.6480 [hep-ph].
- [184] A. Ibarra, C. E. Yaguna, and O. Zapata, *Phys. Rev.* **D93**, 035012 (2016), 1601.01163.
- [185] T. Bringmann, L. Bergstrom, and J. Edsjo, *JHEP* **01**, 049 (2008), 0710.3169.
- [186] T. Toma, *Phys. Rev. Lett.* **111**, 091301 (2013), 1307.6181.
- [187] CMS Collab., CMS-PAS-SUS-12-022.
- [188] ATLAS Collaboration (2015), ATLAS-CONF-2015-070.
- [189] CMS Collaboration (2015), CMS-PAS-EXO-15-005.
- [190] CMS Collaboration (2015), CMS-PAS-EXO-15-006.
- [191] S. Esch, M. Klasen, and C. E. Yaguna (2018), 1804.03384.

Acknowledgements

I would like to thank the following people without whom this work would have been impossible:

- First of all, my advisor Prof. Michael Klasen, for giving me the opportunity of doing this work, for his patience and support during this time, and for everything he taught me.
- Jun. Prof. Anna Kulesza and Prof. Christian Weinheimer for being my second and third advisors.
- Prof. Benjamin Fuks and Prof. Carlos Yaguna for everything they taught me on the topics of this thesis.
- Sonja Esch and Dr. Karol Kovařík for so many useful discussions and for all their help.
- My colleagues during this time, especially Dr. Marcel Rothering, for all the things we have gone through together; Dr. Christoph Borschensky, Dr. Florian König, Dr. Vincent Theeuwes, Dr. Stefano Piemonte, Dr. Pietro Giudice and the rest of the institute for the great atmosphere they created.
- My family, my father Luis Regalado, my stepmother Margarita Delgado, my brother Luis Regalado, my sister Margarita Regalado, my grandmother Rocío Morales, and my girlfriend Dr. Isabell Twick, for so many things.

*To the memories of
my mother, Rocío Lamprea,
and my grandfather, Antonio “Maera” Lamprea.*

Lebenslauf

- Name: David Regalado Lamprea
- Geburtsdatum: 27/05/1989
- Geburtsort: Sevilla, Spanien
- Staatsangehörigkeit: Spanien
- Eltern: Rocío Lamprea Morales (†) / Luis Regalado Calderón

Schulbildung

- 2011–2017: Instituto Fernando de Herrera, Sevilla, Spanien (Gymnasium)
- 2005–2011: Colegio España, Sevilla, Spanien (Grundschule)

Studium

- **2011–2012: MSc Physik**
Westfälische-Wilhelms Universität Münster
Masterarbeit: Resummationsvorhersagen für die Produktion neuer elektroschwacher Eichbosonen am LHC
Schwerpunkt: Theoretische Teilchenphysik
Betrüer: Prof. Dr. Michael Klasen
- **2007–2012: Licenciado Física (Physik), Universidad de Sevilla, Spanien**

Promotionsstudium

- **2012–: PhD Physik**
Westfälische-Wilhelms Universität Münster
Unter der Betreuung von Prof. Dr. Michael Klasen
Masterarbeit: Precision computations for gaugino and scalar dark matter
Schwerpunkt: Theoretische Teilchenphysik

Vorträge

- 03/2015: Rencontres de Moriond, Young Scientists Forum, La Thuile, Italien
- 12/2014: GDR Terascale, Heidelberg, Deutschland

- 11/2013: Theoretical Physics Seminar, University of Liverpool, Vereinigtes Königreich
- 11/2013: Particle Physics Group Seminar, University of Manchester, Vereinigtes Königreich
- 03/2013: Deutsche Physikalische Gesellschaft (DPG), Dresden, Deutschland
- 01/2013: ATLAS SUSY seminar und CMS SUSY seminar, CERN, Genf, Schweiz
- 03/2011: SLTB Symposium, The Linnean Society, London, Vereinigtes Königreich

Veröffentlichungen

- S. Esch, M. Klasen, DRL, C. E. Yaguna,
Lepton flavor violation and scalar dark matter in a radiative model of neutrino masses,
Eur. Phys. J. C78 (2018).
- A. Corral, M. Balcerzyk, A. Parrado-Gallego, I. Fernández-Gómez, DRL, A. Olmo, R. Risco,
Assessment of the cryoprotectant concentration inside a bulky organ for cryopreservation using X-ray computed tomography,
Cryobiology 71, 419 (2015).
- T. Ježo, M. Klasen, DRL, F. Lyonnet, I. Schienbein,
NLO+NLL limits on W' and Z' gauge boson masses in general extensions of the Standard Model,
JHEP 1412, 092 (2014).
- B. Fuks, M. Klasen, DRL, M. Rothering,
Revisiting slepton pair production at the Large Hadron Collider,
JHEP 1401, 168 (2014).
- B. Fuks, M. Klasen, DRL, M. Rothering,
Precision predictions for electroweak superpartner production at hadron colliders with Resummino,
Eur. Phys. J. C73, 2480 (2013).
- B. Fuks, M. Klasen, DRL, M. Rothering,
Gaugino production in proton-proton collisions at a center-of-mass energy of 8 TeV,
JHEP 1210, 081 (2012).

Berufstätigkeit

- 12/2017–: Data Scientist, mobile.de, eBay, Berlin, Deutschland
- 08/2016–11/2017: Data Scientist, Future Finance, Dublin, Irland
- 11/2012–12/2015: Wissenschaftlicher Mitarbeiter, Institut für Theoretische Physik, Westfälische-Wilhelms Universität Münster, Deutschland
- 2011–2012: Studentische Hilfskraft, Institut für Theoretische Physik, Westfälische-Wilhelms Universität Münster, Deutschland

Münster, den 7. Mai 2018.